11-18-2016

Photocatalytic Reduction of CO2 with Tunable Bandgap and Bandedge Materials

Thuhuong T. Ngo
University of South Florida, kassie.ngo@gmail.com

Photocatalytic Reduction of CO_2 with Tunable Bandgap and Bandedge Materials

by

ThuHuong T. Ngo

A dissertation submitted in partial fulfillment
of the requirements for the degree of
Doctor of Philosophy in Chemical Engineering
Department of Chemical and Biomedical Engineering
College of Engineering
University of South Florida

Co-Major Professor: Babu Joseph, Ph.D.
Co-Major Professor: Venkat Bhethanabolta, Ph.D.
John Kuhn, Ph.D.
Shengqian Ma, Ph.D.
Arash Takshi, Ph.D.

Date of Approval:
November 7, 2016

Keywords: CO_2 conversion, photocatalyst, metal-organic-framework (MOF), perovskite, photosynthesis

DEDICATION

I would like to dedicate this manuscript to my husband, Marc C Moore, for always inspiring and supporting me throughout my Ph.D study.

ACKNOWLEDGMENTS

I wish to thank the members of my committees, Dr. Joseph, Dr. Bhethanabotla, Dr. Ma, Dr. Kuhn, Dr. Takshi for their support and direction. I would like to express my appreciation to my advisors, Dr. Babu Joseph and Dr. Venkat Bhethanabotla for their support and guidance throughout the course of my dissertation. Dr. Joseph has been supportive, and has acted as a great mentor to me throughout my PhD studies. Dr. Bhethanabotla has been motivating and has given me assistance through the course of my degree. Together they have been a great team.

Additionally, I would like to thank Dr. Ma and Wenyang Gao for their collaboration on the MOF section of this dissertation. Dr. Ma has allowed me to use his laboratory resources, and provided me with intellectual support. I am also grateful to Dr. Kuhn and his group who have provided me with materials, equipment, and guidance which have made this dissertation possible.

I am extremely thankful to my labmates, graduate students, and postdocs for all their assistance and support - especially Chita Yang and Xianhui Zhao. Throughout my graduate career, they have provided me with guidance and motivated me. I will miss their company in my office and laboratory.

Furthermore, I would like to thank all undergraduate students who I have worked with including Trang Tran and Matthew Khaselic for their persistence, hard work, and cheerful spirit. It has been a pleasure to provide them with laboratory skills and mentor them. I appreciate their commitment to the projects described in this dissertation.

Finally, I am thankful to my family – including my mom, dad, brother. They have provided me with love, support, and have constantly encouraged me throughout my PhD. Especially, I am grateful to my husband who has always been the greatest believer, and provided me with unwavering support.

TABLE OF CONTENTS

LIST OF TABLES

LIST OF FIGURES

ABSTRACT

Solar energy is a sustainable resource which has substantial potential to meet the increasing demand for renewable energy. Though there has been some success in harvesting solar energy for electricity production, converting solar energy to chemical energy as fuels is still a challenge due to low efficiency.

Since the discovery of TiO_2 photocatalysts for splitting water (4) and reducing CO_2 (5) to form useful chemical feedstock such as H_2, CO and CH_4, much research has been done to increase the efficiency of photocatalysts. However, the current conversion efficiency of photocatalysts remains low (~5%) (6, 7). Issues being addressed include the wide bandgap and mismatched band edge for reactions (thermodynamic energy for reaction), poor quantum efficiency of the photon collector systems, high recombination of e^-/h^+ pairs and limitation in the rate of charge transfer from photocatalyst to reactants.

This work focuses on improving efficiency of photocatalysts for fuel production through several approaches: (1) engineering a metal-organic-framework (MOF) to have proper band gaps and band edges for targeted reactions and for enhancing photoadsorption in the visible light range, (2) tuning an ABO_3-type perovskite for desired bandgaps and thermodynamically favored bandedges for CO_2 reduction with water in visible light range.

A porphyrin-based Ti-MOF is studied for CO_2 photoreduction to gaseous chemical fuels such as CH_4 and CO. The porphyrin linkers allow porphyrin-based MOF-525 to achieve narrow bandgap (Eg = ~1.7eV) to absorb visible light, indicating its

ability to harvest more solar energy than conventional TiO_2. Ti/Zr-MOF-525 also exhibited the appropriate energy level alignment for CO_2 and H_2O redox reaction for CO and CH_4 production. Its CO_2 photoreactivity under visible light was demonstrated in a photoreaction, illuminated by 150W Xenon solar simulator. Interestingly, Ti/Zr-MOF-525 demonstrates a selectivity toward CH_4, a more valuable fuels than CO. The gas phase reaction condition is an advance over liquid photoreaction. The catalyst stability was also studied and presented. After 3 cycles of reactions, Ti/Zr-MOF-525 is relatively stable for CO_2 photoreduction and able to maintain its photoreactivity at about 60-65% of fresh catalyst. The reduction of reactivity is due to a less stable fresh catalyst.

When investigating $LaCr_{1-x}Fe_xO_3$ perovskite oxides for photocatalyst, it was found that when replacing Cr ions at the B sites of $LaCrO_3$ by Fe ions, the bandgap does not follow a linear trend in regards to metal ratio composition but rather reflects the smaller bandgap of $LaFeO_3$. Bandedges were successfully measured for the new synthesized materials. At $x = 0.25$, the conduction band potential remains similar with $x = 0$. However, at $x = 0.75$, the conduction band potential was more negative than either perovskites at $x = 0$ or $x = 1$. Future simulation of density of state could address this interesting observation. CO_2 reduction relativities of each perovskites were predicted well by their measured bandgaps and bandedges. Among five studied perovskites, synthesized $LaCr_{0.25}Fe_{0.75}O_3$ ($x = 0.75$) is the most active for CO_2 photoreduction under visible illumination at room temperature thanks to its small bandgap (2.0 eV) and its suitable bandedges for CO_2 photoreduction.

CHAPTER 1: INTRODUCTION

1.1 Harvest Solar Energy and Photocatalysis

The DOE-BES Workshop on Solar Energy Utilization recently reported that the amount of solar energy that strikes the surface of the earth in one hour is more than enough for human energy assumption for an entire year (8). However, only a small fraction of the current energy consumed by our society is generated through solar technology (8, 9). Furthermore, the current harvesting of solar energy is predominantly limited to produce electricity and for heating, which is not suitable for use in transportation (9). Thus, the challenge to harvest solar energy for direct conversion to fuels has gained much attention in the research community (9). However, low conversion efficiency remains a challenge due to the nature of the photocatalysis process.

Photocatalyst is a material that has two main characters: 1) the semiconductor properties where it can be excited by photons when illuminated and generate electrons/hole (e^-/h^+) pairs, and 2) the catalytic properties where it assists the reaction to occur at a lower activated energy from the generated e^-/h^+ pairs (Figure 3). When the photocatalyst is illuminated under light, the photons excites the ground state electrons at the valence band (VB) to the conduction band (CB) (Figure 3) and creates e^-/h^+ pairs. The energy difference between VB and CB is called the bandgap. To generate e^-/h^+ pairs, the energies of absorbed photons have to at least equal to the bandgap energy.

Since the solar spectrum spreads from photons in the UV range where the wavelengths start at ~250nm (equals to photon energy of 4.96 eV) to photons in the IR range where the wavelengths can be 2500nm (equals to photon energy of 0.496 eV) (Figure 2), the smaller the band gap the more light get absorbed and the more e^-/h^+ pairs are generated for the photocatalytic reactions. Photon wavelengths, their frequencies and their energies relationship follows Max Planck's equation (10):

$$E_p = h\nu = \frac{hc}{\lambda} \quad \text{(Equation 1)}$$

where Ep is energy of photon, h is Planck's constant and equals to 6.63×10^{-34} J·s, v is photon frequency, λ is photon wavelength and c is speed of light and approximately equals to 3.00×10^8 m/s

To enhance the efficiency of the photocatalytic process, we need to (1) improve the photoabsorption and charge separation within photocatalysts, and, (2) increase the catalytic activity of photocatalysts. To improve photoabsoprtion and charge generation, there have been several techniques proposed for known inorganic semiconductor materials (i.e metal oxides and metal sulfides) such as reducing band gap by doping (1, 11-13) or by applying z-scheme of photocatalysts (14-17). To enhance charge separation one can try to make materials with more perfect crystallinity to reduce defects which promotes recombination. To enhance the charge transfer to reaction sites, one can create electron traps (18, 19) or co-catalyst (19, 20).

However, most of these modifications come at the expense of other properties. For instance, doping to reduce band gap will create more defects which increase recombination. Z-scheme of photocatalyst can absorb broader solar spectrum, however it creates a transition interface between materials, which increases e^-/h^+ recombination.

Overall, techniques to maximize the advantages and minimize the disadvantages to increase photocatalyst activity are still a challenge.

In this work, the photoabsorption ability of photocatalysts was improved by engineering materials for a narrower bandgap. The catalytic reactivity of photocatalysts was increased by employing the materials that have appropriate conduction band and valence band energy alignment for the CO_2 reduction with water (discussed in the following section), and in MOF case is also by increasing the surface area, providing more active site for CO_2 to react.

Figure 1: Pictorial abstract of the dissertation

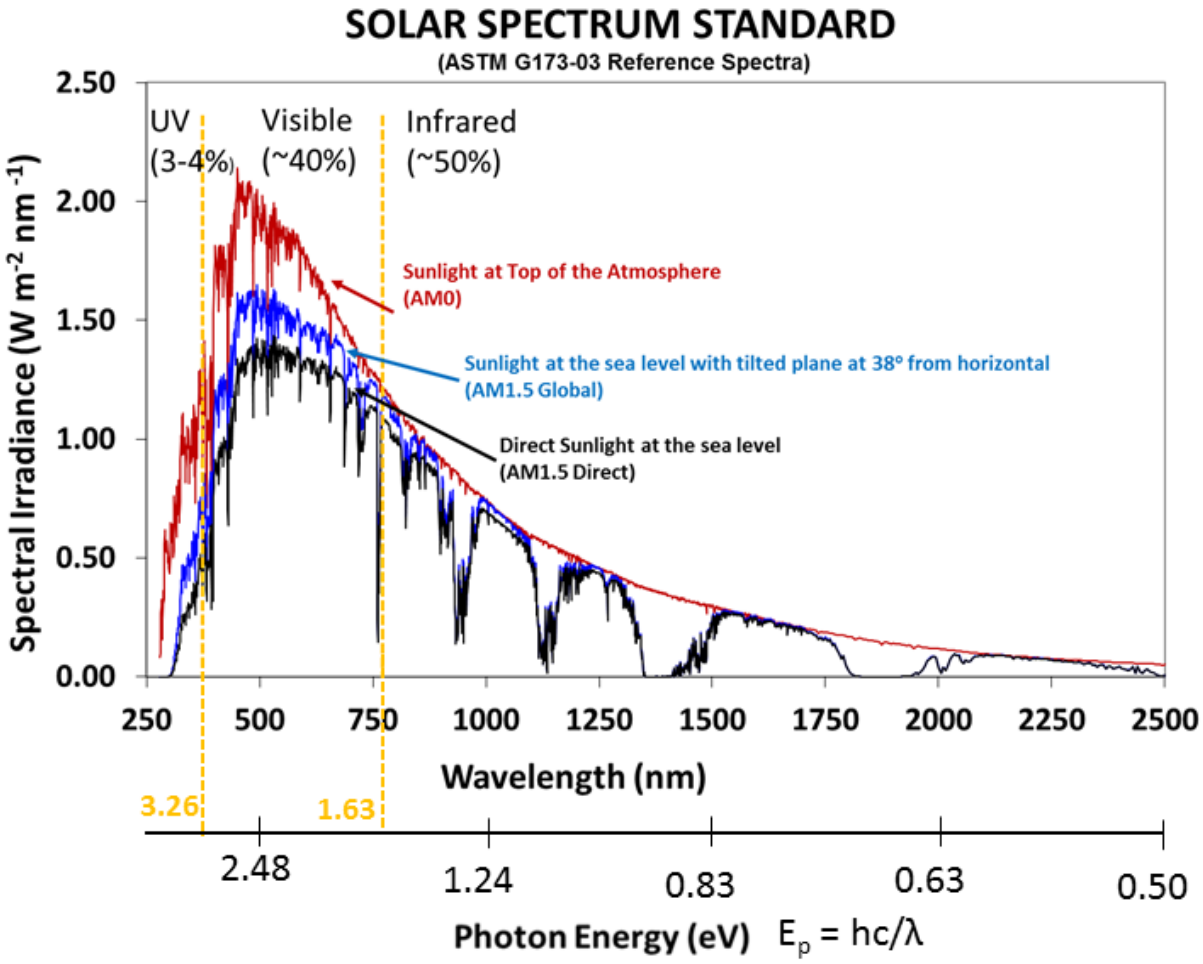

Figure 2: Solar spectrum with the x-axis in wavelength (nm) unit and in energy (eV) unit. Data was obtained from National Renewable Energy Laboratory (NREL) at link http://rredc.nrel.gov/solar/spectra/am1.5/astmg173/astmg173.html

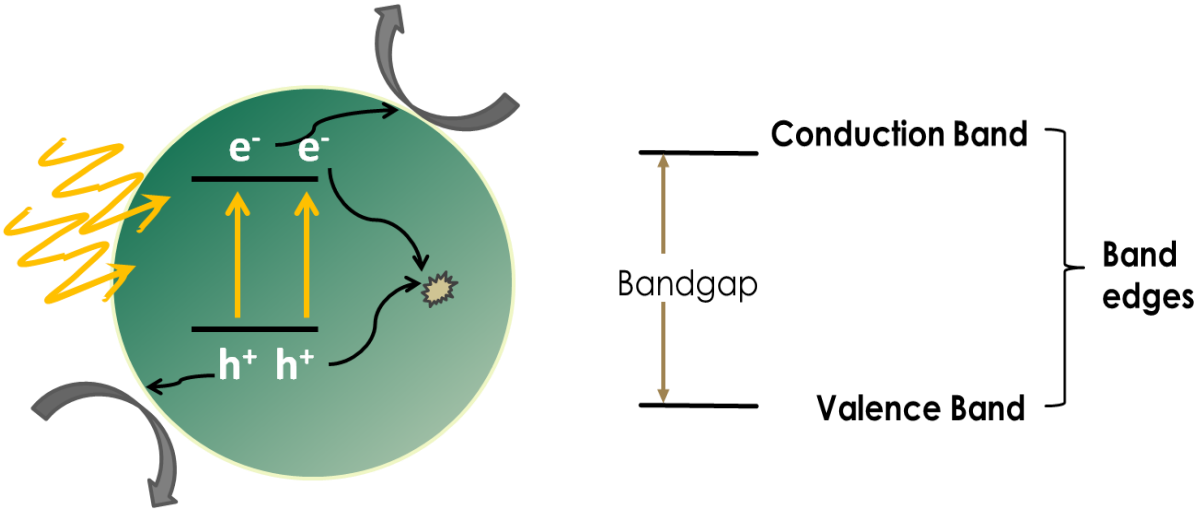

Figure 3: Photocatalyst properties and photocatalytic process. a) Photocatalytic process of CO_2 reduction with H_2O by a photocatalyst. b) Bandgap and bandedges determination

1.2 CO_2 Photoreduction with H_2O

CO_2 reduction with H_2O follows two main half reactions: the oxidation of water and the reduction of CO_2 (5, 21, 22) as presented below.

$$\text{Photocatalysts} \rightarrow e^- + h^+ \quad \text{(Equation 2)}$$

$$2H_2O + 4h^+ \rightarrow O_2 + 4H^+ \quad E = \text{(Equation 3)}$$

$$CO_2 + 2H^+ + 2e^- \rightarrow CO + H_2O. \quad E = -0.53 \text{ V vs NHE (Equation 4)}$$

$$CO_2 + 8H^+ + 8e^- \rightarrow CH_4 + 2H_2O. \quad E = -0.24 \text{ vs NHE (Equation 5)}$$

In the photocatalytic process, after e^-/h^+ pairs are generated from incident photons, they either recombine within the photocatalysts, where no reaction will occur, or they migrate to reaction sites and contribute to the reaction. In the CO_2 reduction with H_2O, the excited electrons help breaking the CO_2 bonds and reduce CO_2 to CO or CH_4, while the holes interact with H_2O and oxidize it to O_2 (Figure 3a). Since both halves of

the redox reaction occurs simultaneously, the photocatalysts remain charge neutral, making it able to continue to generate e^-/h^+ to catalyze the reaction.

For the reaction to occur, the e^-/h^+ pairs have to satisfy the thermodynamic potentials for CO_2 reduction and H_2O oxidationPhotocatalysts → e- + h+ (Equation 2-5). In other words, the excited electrons (e^-) at the conduction band have to have higher energy than the required thermodynamic potentials of CO_2 reductions, which are -0.53 V versus normal hydrogen electrode (NHE) for CO production and -0.24 V versus NHE for CH_4 production. The holes (h^+) at the valence band have to have energy lower than the required thermodynamic potentials of H_2O oxidation, which is 0.82 V versus NHE. In general, the bandedges which are defined to be the lowest point of the conduction band and the highest point of the valence band are required to align appropriately for the CO_2 photoreduction with H_2O (Figure 4a).

Figure 4b lists several known heterogeneous photocatalysts with their bandedge positions in regards to CO_2 reduction potentials and H_2O oxidation potential. According to Figure 4b, only TiO_2 and SiC are potential candidates for CO_2 conversion.

In this work, studied photocatalysts are characterized for their bandedges as a criteria to achieve CO_2 photoreduction with H_2O.

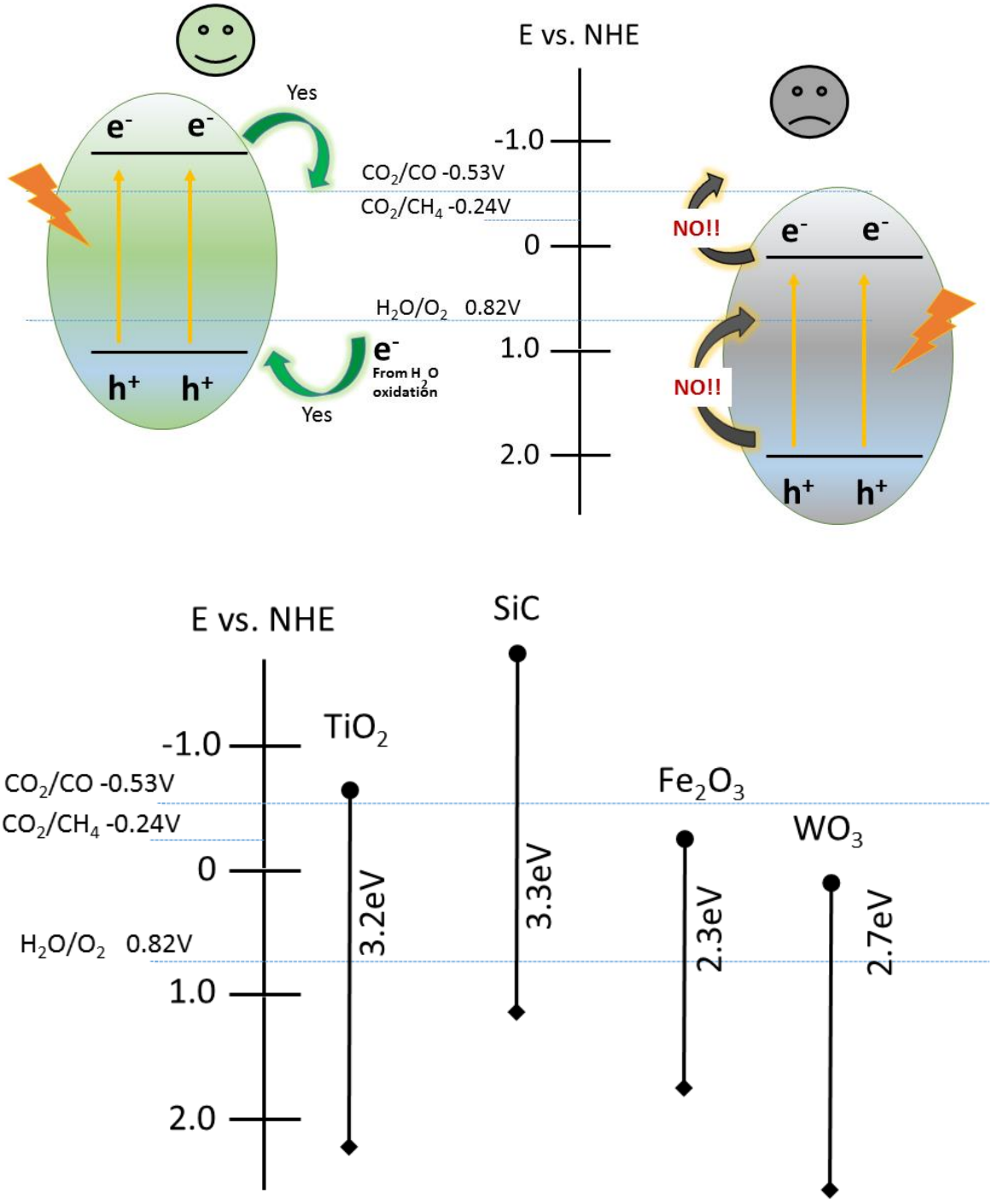

Figure 4: CO_2 photoreduction bandedge requirement and several photocatalyts band energy alignment. a) Scheme to explain the bandedge requirement for CO_2 reduction with H_2O. b) Bandedge potential positions of several photocatalysts in respects to CO_2 reduction and H_2O oxidation potentials. Information was extracted from Reference (22)

1.3 Metal-Organic-Framework (MOF)

MOF are hybrid-inorganic-organic materials where metal ions or clusters coordinate to organic ligands (Figure 5). Their structures and properties can be tuned and engineered with unlimited possibilities. MOF has been shown to have diverse structures and various associated properties (23-25). Some MOFs have been demonstrated to be stable at high temperatures and in aqueous environments (26, 27). Because of the hybridization between metal-containing cluster and organic ligands, some MOFs acquire semiconductor properties like their metal oxide counterparts (28-30). Their band gaps can be tuned by the choice of their linkers (31) or of their metal clusters (secondary-building-units, SBU) (32, 33). The metal SBUs in MOFs were demonstrated to be more catalytically effective than bulk materials due to the small and limited space within their frameworks (32, 34). The charges transfer process between linkers and metal clusters in MOF has been observed and demonstrated to be beneficial for charge separation (28, 35), which is hypothesized to occur easier because the charge giver (linkers) and receiver (metal clusters) belong to a same framework.

Recently, MOF has been demonstrated to have photocatalytic activity such as for phenol degradation (28) and for CO_2 reduction in solution using sacrificial reducing agent (35, 36). However, these findings have limited useful applications and still require sacrificial reducing agents, which are not applicable in commercial processes.

In this work, we eliminate the sacrificial reducing agents and run the reaction under gas phase.

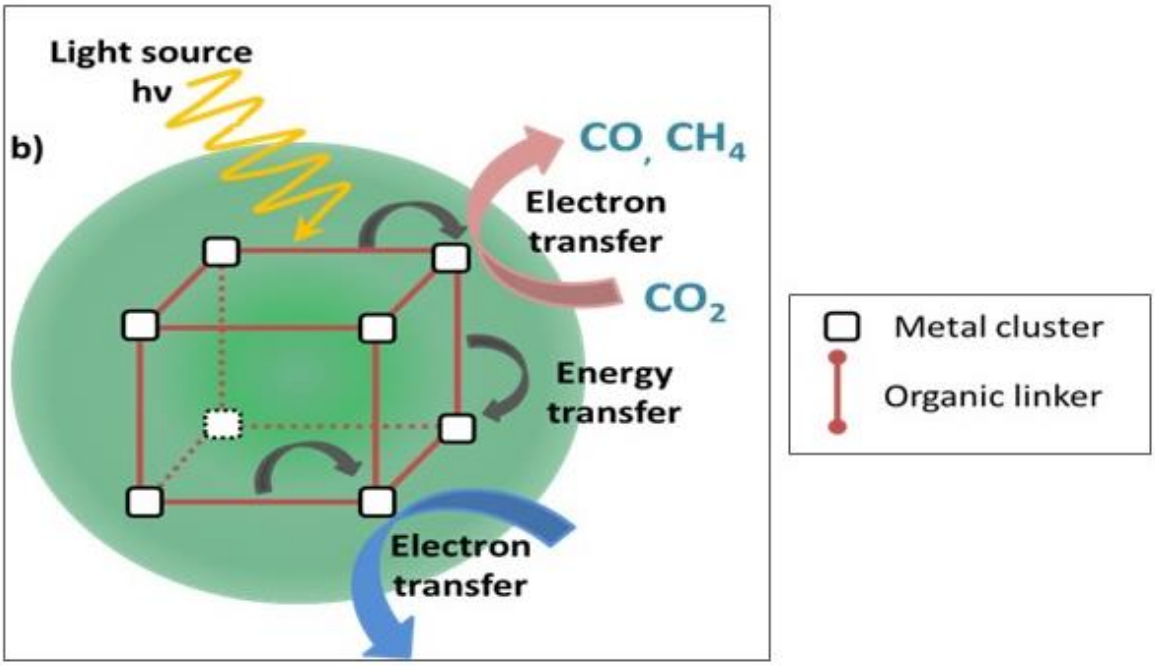

Figure 5: Scheme of metal-organic-framework photocatalyst

1.4 ABO_3-Type Perovskite Oxides

Perovskite oxides are hybrids of two or more metal oxides (Figure 6). Their general formula is ABO_3 where A sites are larger metals (i.e. La) and B sites are smaller transition metal (i.e. Fe, Cr etc.) (37-39). Each site A and B can be partially substituted by different metals(39). Because of this flexibility, perovskite is a class of materials which have a wide number of compounds and it can be tailored for desired characters for various applications such as in fuel cells(40), in catalytic converters(41), in photovoltaics(42). The physical and electrochemical properties of such perovskite materials can be modified through doping alkaline-earth elements into the A site and transition-metal elements into the B.

Recently, Luo et al.(42) has reported water splitting by perovskite photovoltaics at 12.3% efficiency, a number makes the solar water splitting efficiency comparable to electricity harvest by solar panels. Since photocatalysts are also semiconductors, materials which are great for photovoltaics are usually attractive candidates for photocatalyst. La-based photocatalyst have been reported for evolution of H_2 and O_2 from water under Uv irradiaion (43, 44). NiO/NaTaO3:La photocatalyst have high efficiency 50% (12). La-based pervoskites are also known to have strong basic sites for CO_2 adsorption (45), which potentially enhances CO_2 reduction reactivity. $LaFeO_3$ has many applications such as catalytic oxidation. It was also reported to have photocatalytic activity for water splitting(46) or pollutant degradation (47-49) under visible light illumination. Cr-doped metal oxides and perovskites(50) (2, 51) have been reported to be visible-light-driven photocatalysts. $LaCrO_3$ have also been used for fuel cell anodes (52-54).

In this dissertation, $LaCr_{1-x}Fe_xO_3$ was investigated for its changes in bandgap and bandedges when gradually substituted Fe ions for Cr ions. Consequently, its CO_2 photoreactivities were studied in responses to the Fe ion replacement.

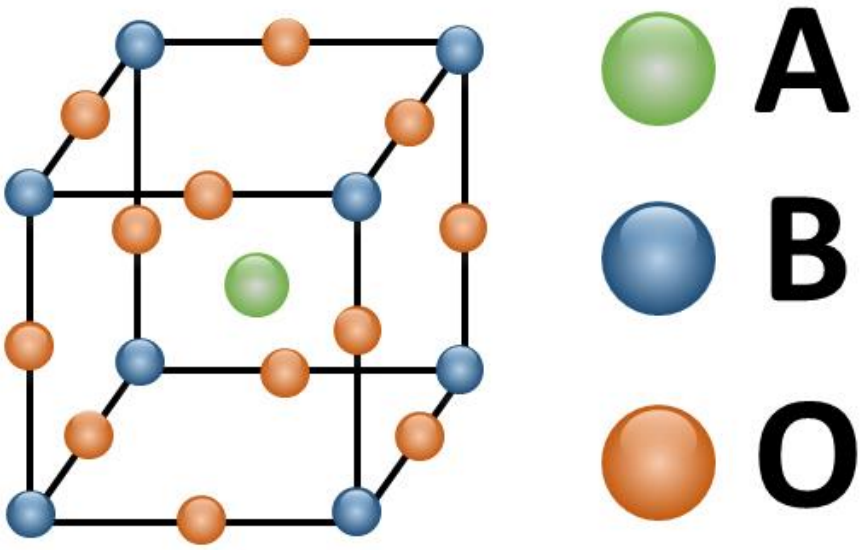

Figure 6: Scheme of ABO_3-type perovskite photocatalyst

CHAPTER 2: METHODOLOGY

2.1 Preparation of Materials

2.1.1 Synthesis of Metal-Organic-Framework

This work is in collaboration with Dr. Ma's lab. Wenyang Gao synthesized and provided the original materials, both Zr-MOF-525 and Ti/Zr-MOF-525.

MOF-525 materials were chosen partially because of their water stability(27, 55), an important requirement for the CO_2 reduction with H_2O, and also because of its porphyrin-based linker which enables the MOF to harvest visible light (56). Titanium-based MOF were selected for investigation due to the known photocatalyst reactivity for CO_2 reduction from their metal oxide TiO_2 and from other titanium-based MOF studied previously (35, 57, 58). Reports in literature of active Ti-based MOF for photoreactivity have been documented, though they have either been used for hydrogen production (57),(28, 59) or when for photocatalytic CO_2 reduction, they have either used a UV range illumination or with sacrificial agents (28, 35, 60-62). MOF-525 have free-base meso-tetra (4-carboxyl-phenyl) porphyrin (H_2TCPP) as linkers and Zr or Ti/Zr- mixed metallic clusters (SBUs) and is the first reported to exhibit reactivity for CO_2 photoreduction with H_2O to produce CH_4 and CO in gas phase and without sacrificial agent.

Briefly, Zr-MOF-525 was prepared using a slightly modified procedure as described in the literature (27). Zirconyl chloride octahydrate ($ZrOCl_2{\cdot}8H_2O$, Sigma-

Aldrich, 98% reagent grade) was added to N,N-dimethylformamide (DMF, Sigma-Aldrich, ≥99%) and sonicated for 15 minutes. Then, tetrakis (4-carboxylphenyl) porphyrin (TCPP, Sigma-Aldrich, ≥90%) and acetic acid (Sigma-Aldrich, ≥99%) were added to the solution and further sonicated. The scintillation vial was placed in an oven of 65^{o}C for 3 days. The dark colored powder was collected via centrifugation, then washed 5 times with DMF and with acetone over three days. Zr-MOF-525 was activated by heating at 120^{o}C under vacuum for 24 hours.

The Ti-exchange process of Zr-MOF-525 was carried out in glove box according to the work of Cohen and co-workers (62) using $TiCl_4$ $(THF)_2$. The mixture was incubated for 5 days. The solids were separated from the solvent via centrifugation, and washed with fresh DMF and methanol several times. The solids were activated at 120^{o}C under vacuum overnight.

2.1.2 Synthesis of Perovskite Oxides

2.1.2.1 The Pechini Synthesis Method

The Pechini Method uses a carboxylic acid, most commonly citric acid, as a chelating agent to dissolve the salt precursors of metals in perovskites (63). This creates a homogeneous dispersion of cation in the solution, resulting in a well-dispersed single-phase perovskites after the calcination (64). The Pechini Method has high reproducibility and a good precise stoichiometry control of the synthesized perovskites, which is important for this work as the ratio of metal in site B is varied from 0 to 1. The single-phase perovskites are desired for a better charge transfer and preventing charge recombination, which will reduce photo quantum yield.

2.1.2.2 Synthesis of $LaCr_{1-x}Fe_xO_3$

$LaCr_{1-x}Fe_xO_3$ (x = 0, 0.25, 0.5, 0.75, 1) perovskite powders were synthesized using the Pechini Method, similarly described by Popa and Kakihana(65) and followed similar procedures of previously synthesized $LaCr_{1-x}Fe_xO_3$ by Divya Suresh (66). Briefly, citric acid (Sigma Aldrich, ≥99.5%) was dissolved in 60^{o}C water. Then, appropriate amount of precursors La $(NO_3)_3$ (Sigma Aldrich, ≥99.9%), Cr $(NO_3)_3$ (Alfa Aesar, 99.9%) and Fe $(NO_3)_3$ (Sigma Aldrich, ≥98%) were added to the solution. The mixtures was continuously stirred at 60^{o}C for 2 hrs. After ethylene glycol (Sigma Aldrich, ≥99%) was added, the solution was raised to 90^{o}C and remained at this temperature for 7 hrs while under constant stirring. The gel-like resin was transferred to the oven where it was heated at 450^{o}C for 2 hrs to decompose all the metal precursors, and then at 950^{o}C for 6hrs to form the final perovskite catalysts.

The molar ratios of materials used was La: citric acid: ethylene glycol = 1:10:40 as described in Yolanda et al. (67). The amounts of Cr $(NO_3)_3$ and $Fe(NO_3)_3$ precursors used were determined to target the metal molar ratios in $LaCr_{1-x}Fe_xO_3$ where x = 0, 0.25, 0.5, 0.75, 1.

2.2 Characterization Techniques for Photocatalysts

2.2.1 N_2 Isotherm and Surface Area Determination by Gas Adsoprtion

The method used to determine the surface area and other porosity properties of materials is by gas adsorption, particularly using N_2 adsorption and desorption isotherm. In the process of adsorption, adsorbate (N_2) adsorbs on adsorbent (the interested photocatalyst materials). After saturation pressure P_s, the adsorption does not occur

anymore and no more adsorbates are added on the adsorbents. At this point, all the sites on the absorbent are occupied and the adsorption graph becomes independent of pressure. Different theories were developed to explain the phenomena such as Freundlich, Langmuir and BET adsorption isotherms. In 1938, Brunauer, Emmett and Teller successfully explained the physical adsorption isotherm that at high pressure and low temperature, thermal energy of gaseous molecules decreases and the multilayer formation of gas adsorbed occurs(68, 69). The BET equation is

$$\frac{P}{V_{total}(P-P_o)} = \frac{1}{V_{mono}C} + \frac{C-1}{V_{mono}C}\left(\frac{P}{P_o}\right) \quad \text{(Equation 6)}$$

where V_{mono} is the adsorbed volume of gas at high pressure conditions so as to cover the surface with a monolayer of gaseous molecules

Thus, the mono layer adsorbed volume of N_2 gas can be extracted from the slope and the intercept of the graph $P/(V_{total} * (P_o-P))$ versus P/P_o. Knowing the molecular dimension of N_2, one can easily calculate the surface area of absorbent from the monolayer of adsorbed N_2. Note that BET method is accurate in the P/P_0 range of 0.05-0.3, it is important to obtain the surface area at this range only (68).

2.2.2 X-ray Powder Diffraction (XRD) for Crystal Structure Characterization

X-ray powder diffraction (XRD) is an analytical technique, which is widely used for analyzing crystal structure of crystalline materials. The method can provide information on the unit cell dimensions as well as the lattice parameters. In this study, XRD method was used to characterize the material crystal structures, to determine sample purity and the existence of different metal oxide phases in perovskite.

Max von Laue, 1912, (70) was first to discover that under expose to X-ray, crystalline structures respond similar to the spacing of planes in a crystal lattice. The interaction of the incident X-rays with the studied samples follows Bragg's law ($n\lambda=2d \sin \theta$) for constructive interference (71, 72). This relates the wavelength of electromagnetic radiation to the lattice spacing in a crystalline sample and to its diffraction angle. Because each crystalline material has a set of unique crystal lattice spacing (d-spacings), conversion of the diffraction peaks over a scanning angle range of 2θ to d-spacing allows the materials identified. Since materials used in this work already have known crystal structures, their X-ray diffraction patterns are usually analyzed against a standard. For MOF, it is from previous literature *.cis file. For perovskites, they are compared to XRD Inorganic Crystal Structure Database (ICSD).

2.2.3 Morphology Characterization

Scanning electron microscopy (SEM) is a microscopy technique which uses high-energy electron beam to generate information of the solid material surfaces. SEM generated signals are seen as an image of the specimen surfaces which made of electron responses rather than of photo as in normal photographs (73).

The principle of the technique depends on the electron-sample interactions. During the process, a high-energy accelerated electron beam scans the sample, and transfers its energy to secondary electrons, backscattering electrons or X-ray photons (73). This electrons and photons coming from the sample surface carry information of the samples. In this work, SEM is mainly used for morphology and topography which are generated from the secondary electrons. Different energy and amount of secondary

electrons from the specimen surface yields different contrast and brightness in the image, which presents a feeling on surface morphology in black and white pictures.

The X-ray photons coming from the surface carry characteristic energy of the outer shell of elements at the surface of the samples. This information provide insight of chemical composition of the specimens. This method is called Energy-Dispersive X-ray Spectroscopy (EDS). The limitation of EDS for composition analysis is that it only accounts for 1-2μm depth (74).

Transmission electron microscopy (TEM) operates on a similar basic principles of the scanning electron microscopy (75-77) as it also uses electron beam to bombard the samples. However, while the SEM uses a focused electron beam to scan the sample line by line and detects the scattering or secondary electrons, TEM uses a broad static beam and detects the transmitted electrons. This differences makes the images in TEM opposites color to in SEM, which means generally what appears to be lighter color in SEM will appear to be darker in TEM images. In addition, SEM shows the surface morphology of the samples while TEM shows internal structure of particles. In this study, TEM was used as an extra technique to confirm the particle sizes and shapes of perovskites.

2.2.4 Bandgap Determination by DRS-UV-Vis Spectroscopy

As discussed above, the more e^-/h^+ pairs generated by photocatalysts when excited by incident light, the better the photocatalysts. To absorb more portion of the light and generate more e^-/h^+ pairs, the energy difference between conduction band and valence band (bandgap, Eg) is desired to be small. The bandgap energy can be converted to wavelength using the equation 1 ($E_\lambda=hc/\lambda$), to determine the lowest energy

photo, it can excite photocatalyst and generate charges for reaction. To adsorb all the UV range light, materials should have a bandgap of 3.1eV (~400nm). To adsorb UV light and some visible light upto 500nm, the bandgap should be 2.48 eV. The smaller the bandgap, the more energy the materials can harvest from the sun and more charges are produced.

Diffused reflectance spectroscopy (DRS) is a common and simple technique for obtaining the band gap energy (29) by extracting its diffuse reflectance spectrum through Tauc plots (30, 31). Under the incident light of the DRS, the electronic transitions between the highest occupied valence band and the lowest unoccupied conduction band will yield a high absorption band or a low reflectance spectrum. When the incident photo has small energy (or large wavelength), no excitation occurs and yield low absorption or high reflectance. Band gap energy and the absorption relationship is established through Tauc relation (32, 33)

$$\alpha h\nu = A(h\nu - Eg)^{n} \quad \text{(Equation 7)}$$

where α, v, A, and Eg are the absorption coefficient, incident light frequency, proportionality constant and band gap, respectively. n = 1/2 for direct transition and n = 2 for indirect band transition. Perovskites and MOF both display direct band transition, therefore n = 1/2.

The reflectance spectrum collected from DRS can be described in terms of absorption coefficient from Kubelka-Munk theory (40, 41).

$$F(R) \equiv \frac{(1-R)^2}{2R} = \frac{k}{s}. \quad \text{(Equation 8)}$$

where the ratio of effective absorption coefficient k versus the scattering coefficient s is the true absorption coefficient α of the powder. Thus, Kubelka-Munk function F(R)

equals to the absorption coefficient α in the Tauc equation$\alpha h\nu$ = A$(h\nu - Eg)^{n}$ (Equation 7. For direct bandgap materials, which is the case of MOFs and perovskites, n = 1/2, and the bandgap E_g is the interception of the slope with x-axis when plotting $[F(R)\cdot hv]^2$ as a function of E = hv.

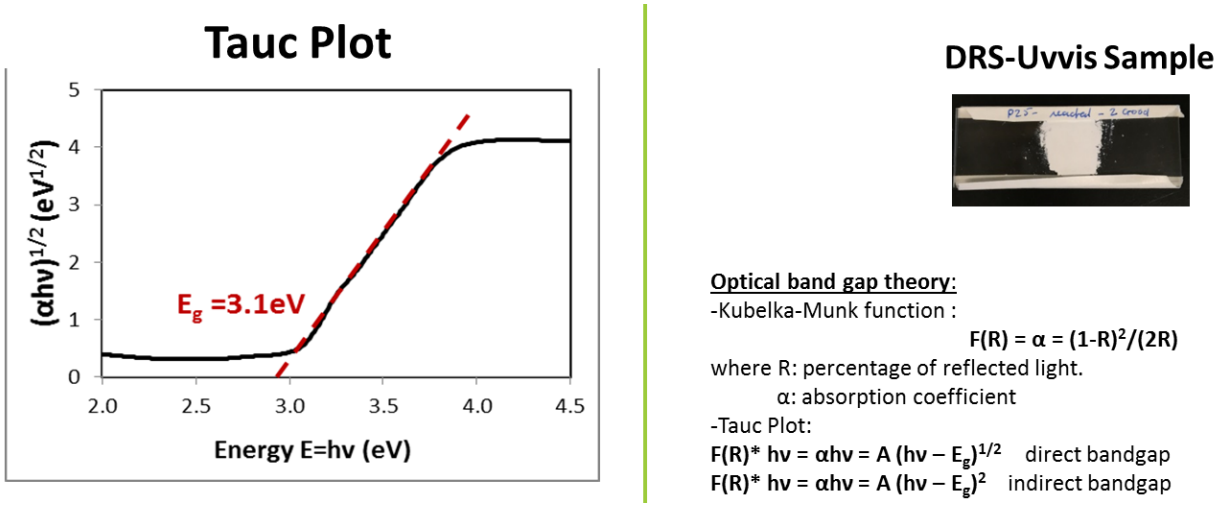

Figure 7 : Optical bandgap measurement and Tauc plot example of TiO_2-P25 to obtain optical bandgap. TiO_2-P25 has indirect bandgap (1-3), therefore n = 2 in equation 7.

2.2.5 Conduction Band and Valence Band Determination by Electrochemical Method

For CO_2 photoreduction to occur, the photocatalyst is required to have a suitable conduction band and valence band, which are thermodynamically favorable for CO_2 conversion. Their conduction band potentials were measured and compared with that of TiO_2-P25. The band energy levels of photocatalyst were investigated using the flat band potential (Vfb) measurement by Mott-Schottky (M.S) plot.

Mott-Schottky plot is a simple and common electrochemical method used to determine the conduction band potentials of semiconductors. When semiconductor electrodes are in contact with electrolytes, at the interface between solid and solvent, the valence and conduction band edges of the semiconductor curved to make its Fermi level in equilibrium with the electrolyte Fermi level (78) as electrons transfer between electrolyte and the semiconductor. This phenomena is called charge depletion at the semiconductor-electrolyte interface.

Figure 8 shows a p-type semiconductor's energy levels and an electrolyte redox potential. In this case, the Fermi level (Ef) is below the redox potential of the electrolyte. At the electrochemical equilibrium when two medium are in contact, electrons from the electrolyte solution transfer to the semiconductor creating a space charge region. This negative space charge region causes a downward bending of the band edges.

For an n- type semiconductor, things happen in an opposite direction. The Fermi level of the semiconductor is more negative than the electrolyte redox potential. Electrons transfer from the semiconductor to electrolyte causes a positive space charge region to form an upward bending of the band edges.

Applying the bias voltage on the semiconductor artificially by a potentiostat separates the Fermi levels of semiconductor and the electrolyte and lessen the level of band bending. When the applied bias voltage magnitude is large enough that there is no band bending or charge depletion, the semiconductor achieves its flat-band potential, Vfb. The Vfb and applied bias voltage (V) relation is described by the Mott-Schottky equation (78, 79)

$$\frac{1}{C^2} = \frac{2}{\varepsilon \varepsilon_0 A^2 e N_D}\left(V - V_{fb} - \frac{k_B T}{e}\right) \quad \text{(Equation 9)}$$

where C is the interfacial capacitance, V the applied bias voltage. From equation 9, a plot of $1/C^2$ against V should yield a straight line and Vfb is the intercept of the line with the V axis. The determined Vfb approximately equals to the conduction band edge (ECB) of an n-type semiconductor or the valence band edge (EVB) for a p-type semiconductor [44]. From the determined band edge from the Mott-Schottky plot and the bandgap from the Uv-vis DRS measurement, the other band edge can be determined by equation 10.

$$E_{CB} - E_{VB} = E_g \quad \text{(Equation 10)}$$

The Mott Schottky (M.S) plot electrochemical method used for band edges determination is valid when it satisfies the assumptions that the bulk semiconductor's resistivity and the capacitances of the space charge layers are negligible (45). This means that the dielectric coefficient ε is independent of the test frequency. Consequently, the band edges measurement using Mott-Schottky plot is measured at a range of frequency and the obtained Vfb from different frequency should be close to each other enough to make the measurement valid.

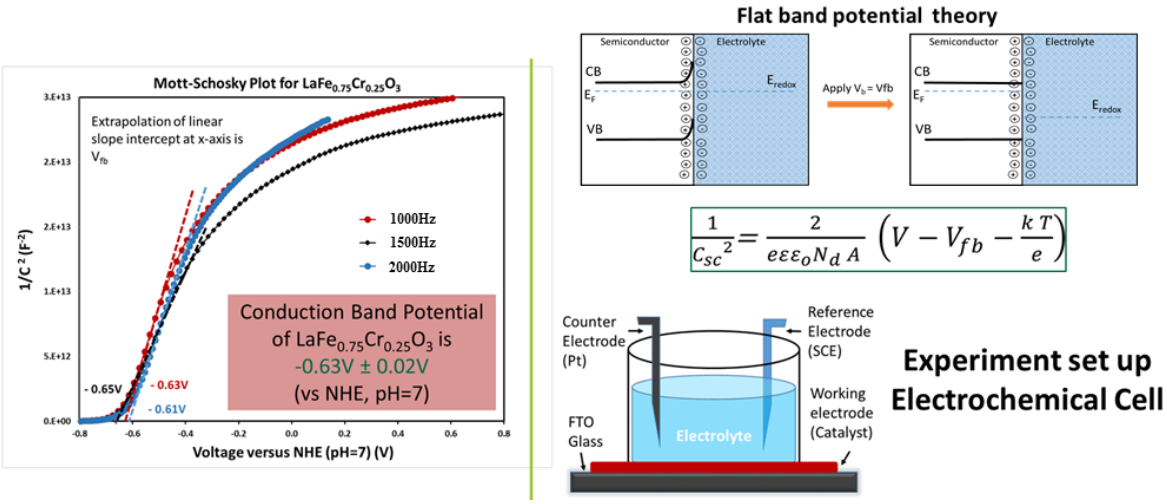

Figure 8: Mott-Schottky plot and experiment set up to obtain flat band potentials. a) Example of Mott-Schottky plot to obtain conduction band potential. b) Electrochemical cell setup. c) Flatband diagram and Mott-Schottky equation

2.3 CO_2 Photoreduction Reactor

CO_2 photoreduction experiments were performed using a setup described previously(80). The reaction was carried out in a stainless steel batch reactor with a quartz window on top.

The CO_2 photoreactor was designed in 2012 and was made at the USF College of Engineering machine shop ENG 118 in spring 2013 (Figure 9). It was made of stainless steel with three parts. Part 1 is the base of the reactor where the photocatalyst sits. Part 2 is the body of the reactor which contains a quartz window with the diameter of 1 inch. Part 3 is the top piece which secures the quartz top window seal especially when operating at higher pressure. Figure 9a shows details and dimension of these three parts. Though all the work done in this dissertation were done at 20 psi, the reactor was tested to operate at 60 psi. Higher pressure is possible, however, it was not tested. There is an o-ring between part 1 and part 2 of the reactor which keeps the reactor airtight during operation. Part 2 also includes a water flowing channel around the reactor area to uniformly cool or heat the reactor. Hot place could be placed under reactor to heat the reactor. Since the o-ring is temperature rated at 200^oC, it is recommended to operate within this temperature limit unless different o-ring is in use. Later, part 1 also modified to have inlet and outlet connections for reactants. Therefore, the reactor has capability to operate at a range of temperature and pressure and either in batch or flow reaction condition. To load photocatalysts, four screws at four corners was loosen to separate part 1 and 2 of the reactor.

Typically, 50mg of catalysts was uniformly spread on a 1 in^2 base area of the reactor. Gaseous 99.99% CO_2 (Airgas) was bubbled through DI water at room

temperature before introduction to the reactor (Figure 10 and 11). The amount of water vapor in the gaseous mixture was calculated to be 3% based on Raoult's law. Before the experiment, the reactor was evacuated. Then, water saturated CO_2 was flowed through at 2ml/min for 30 mins to achieve stability. The reaction was carried out at 20 psi, under irradiation of 150W Xenon light equipped with 1.5AM filter and a visible long pass filter (λ >400nm) for 6 hrs. Light intensities and spectrum at the catalyst surface were recorded using by Li-200R Pyranometer (active from 400-1100nm, Li-COR) and a UV-Vis-NIR spectroscopy respectively (Figure 12). The reactor was cooled by flowing water to maintain isothermal reaction temperature at 40^{o}C. Control runs were performed under the following conditions and no CO or CH_4 formation was observed: 1) under dark condition, and 2) with only N_2 and H_2O vapor when under irradiation. 80µl gas samples were periodically removed by gastight syringe (Hamilton, 100ul) for analysis by gas chromatography (Agilent 6970C) with a thermal conductivity detector (TCD), equipped with a HP-Plot column. The limitation of detection is ~40ppm for both CO and CH_4. CO and CH_4 quantitative analysis by GC-TCD and GCMS was calibrated detailed in the Appendices

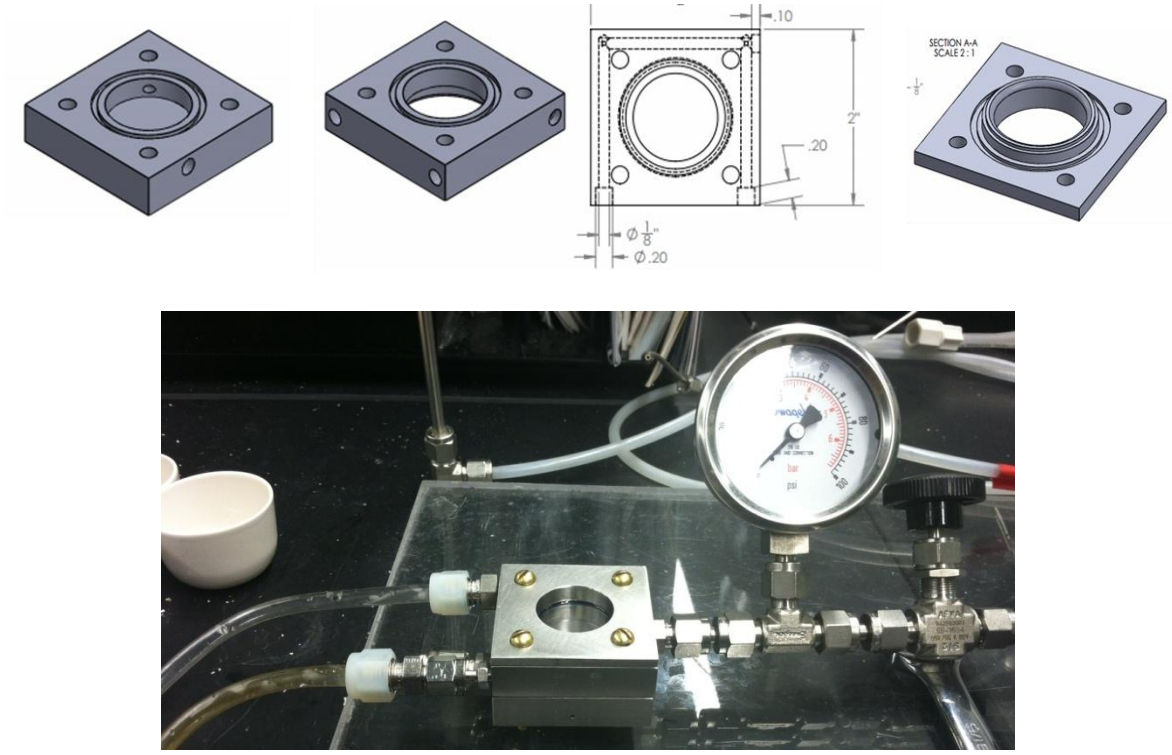

Figure 9: CO_2 reactor design. a) Diagrams of the three parts of the CO2 photoreactor. b) Picture of the assembled photoreactor.

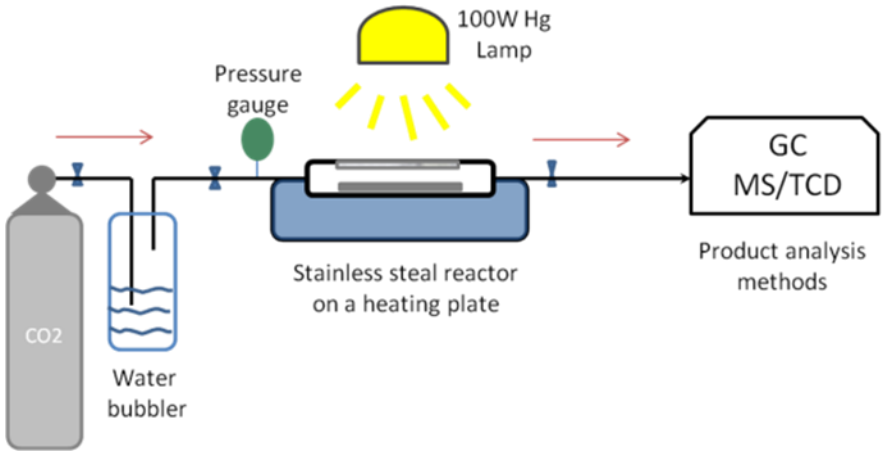

Figure 10: System diagram of CO_2 photocatalytic reaction

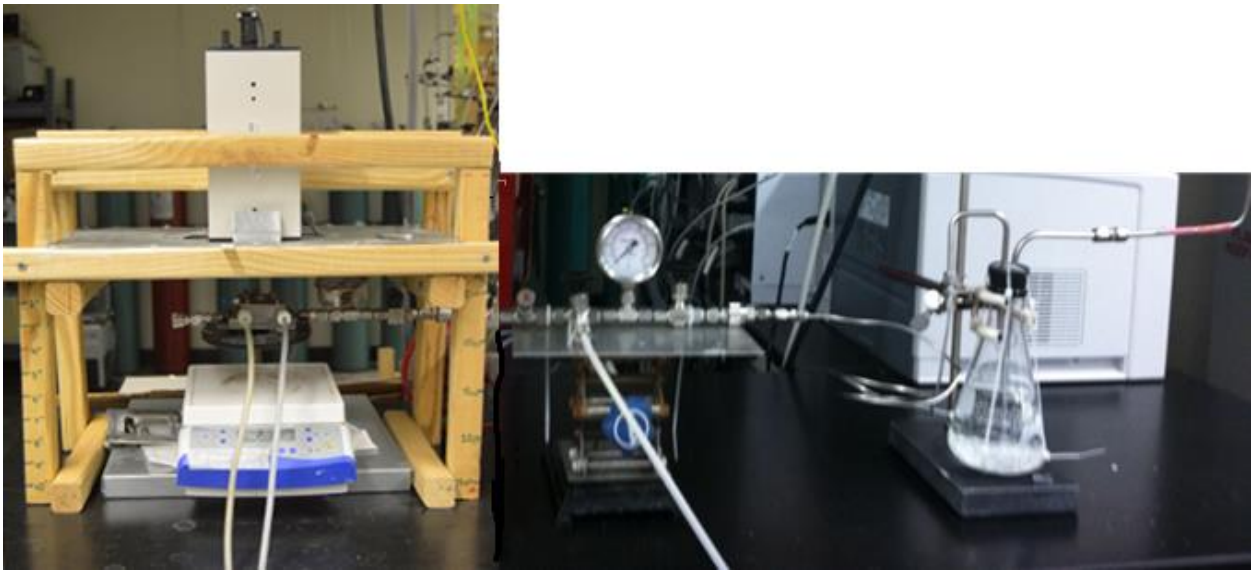

Figure 11: Picture of the CO_2 photorection system. In the picture, the water bubbler sits on the right and the reactor with the light above sits on the left.

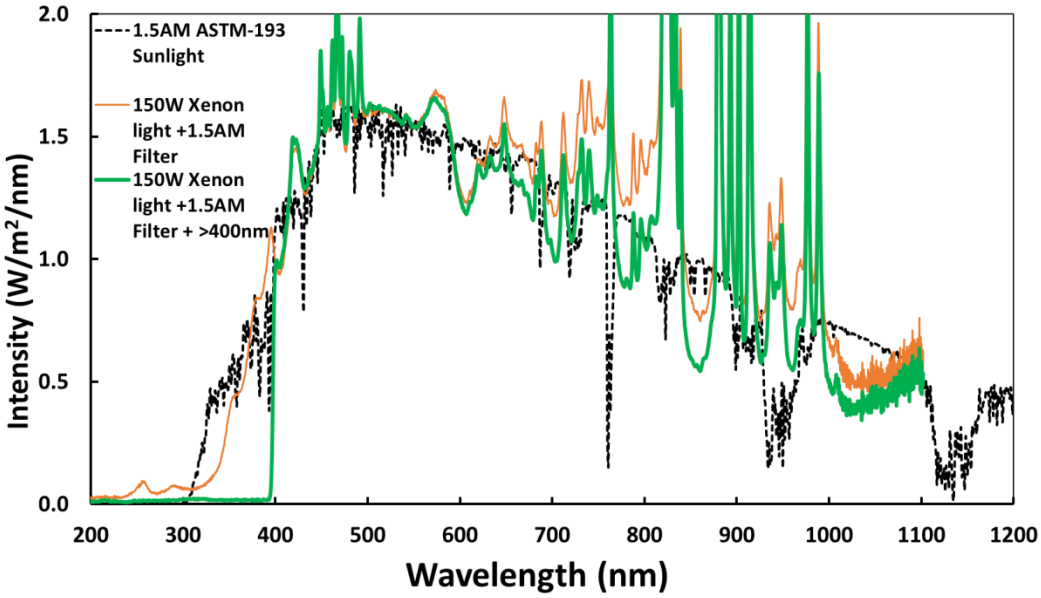

Figure 12: Light spectrum measured at the catalyst surface without filter and with filter

CHAPTER 3: Ti-MOF-525 FOR VISIBLE-LIGHT INDUCED REDUCTION OF CO_2 TO CH_4

3.1 Introduction

Harvesting solar energy for CO_2 conversion to the products of energy-rich chemicals such as H_2, CH_4 and HCOOH has drawn significant attention recently (22, 28, 81, 82) as this approach addresses problems of increased amount of CO2 in the atmosphere due to industrialization and the need for renewable energy sources. Conventional photoactive materials typically lack either a suitable band gap to absorb a broad section of solar spectrum (i.e TiO_2) or the appropriate band edges for CO_2 reduction, thus they are limited in yield efficiency. Recent work has shown that a relatively new class of materials, metal-organic-frameworks (MOFs), can be tailored to exhibit semi-conductivity and photoactivity properties (28, 30, 31, 82) by employing appropriate organic ligands and metal-containing nodes (or secondary building units, SBUs). MOF photocatalysts have seen more interest in CO_2 photoconversion and have become more robust than the 1st generation of MOF photocatalyst where they were tested for dye degradation. However, most of these studies occur in aqueous solution (83) or employ sacrificial agent such as TEOA (62, 82) in organic solvent such as DMF (55). Since the reaction occurs in solution, the main products evolved are HCOOH (82) and CO (55), which have low value as fuels and have to be further converted to useful fuels such as H_2 with the assistance of a suitable catalyst. The use of MOF as

photocatalyst for CO_2 reduction to create ready chemical fuels such as CH_4 has received relatively little attention in literature.

The objective of this work was to investigate the potential of metal-organic-frameworks (MOFs) for CO_2 photoreduction in gaseous phase using visible light, without any sacrificial agent present, to produce chemical fuels, especially CH_4. Previously, we showed that MOFs can be tuned for their band gap by proper selection of linkers or ligands (31). In this work, we demonstrate that when a MOF material is constructed by proper linkers (porphyrin-based) to absorb a broader portion of solar spectrum (visible range), and by metal-containing clusters (or secondary building unit, SBU) which are optimal for CO_2 reduction to CH_4, it benefits positively toward CO_2 photoreduction capability, and thus advances the plausibility of designing MOF photocatalysts for larger scale applications.

MOF materials investigated in this study, Zr-MOF-525 and its Ti-ion exchanged MOF-525 (Ti/Zr-MOF-525) were synthesized by W. Gao in Dr. Ma's lab based on a modified procedure from previous reports (27). These MOFs have free-base meso-tetra (4-carboxyl-phenyl) porphyrin (H_2TCPP) as linkers and Zr or Ti/Zr mixed metallic clusters (SBUs) (Figure 13). MOF-525 materials were chosen in part because of their water stability (27, 55), an important requirement for the CO_2 reduction with H_2O, and also because of its porphyrin-based linker which enables the MOF to harvest visible light (56). Titanium-based MOF were selected for investigation due to their known photocatalyst reactivity for CO_2 reduction from their metal oxide TiO_2 and from other titanium-based MOF studied previously (35, 57, 58). Reports in literature of active Ti-based MOF for photoreactivity have been documented, although they have either been

used for hydrogen production (57),(28, 59) or when used for photocatalytic CO_2 reduction, they have either been used in a wide-spectrum UV illumination range (outside of the visible solar spectrum) or with the aid of sacrificial agents (28, 35, 60-62). Ti-MOF-525 is the first reported to reduce CO_2 in water vapor directly to gaseous fuels CH_4 and CO without the use of sacrificial agents. Ti-based MOF was synthesized by ion exchanging precursor Zr-MOF-525 with $TiCl_4(THF)_2$.

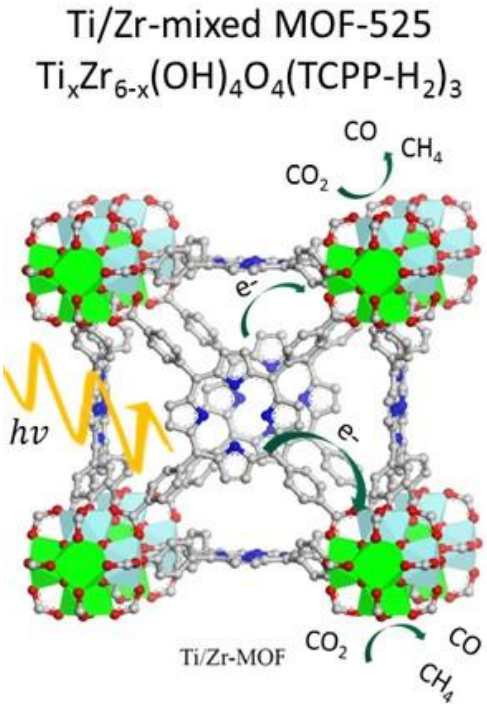

Figure 13: Metal-organic-framework. The image was done with the help of Wenyang who provided the draw of MOF crystal structure

3.2 Methods Used

3.2.1 Material Characterization

The phase purity of catalysts was determined by Powder X-ray diffraction (PXRD) measurement on powder samples at room temperature using a Bruker D8 Advance X-ray diffractometer. The X-ray source was Cu Kα radiation (λ = 1.5406 Å). Diffraction patterns was recorded at a scan speed of 0.5 s/step (6°/min) and a step size of 0.05° in the 2θ range of 5° to 30°. The accelerating voltage and applied current were 20 kV and 5 mA, respectively. The simulated XPD patterns were produced using Mercury 3.6 software.

N_2 gas adsorption isotherms were collected at 77K using the Micromeritics Surface Area and Porosity Analyzer ASAP-2020. Before the measurements, the samples were washed with methanol several times for 3 days. All the samples are degassed at 120^{o}C for 10 hours. The specific surface area was obtained by a multipoint BET method using the adsorption data in the relative pressure (P/P0) range of 0.05–0.3. Pore size distribution were determined by the density functional theory method (DFT).

Morphological observations were carried out on a Hitachi S-800 field emission scanning electron microscope (SEM, Hitachi, Japan). To investigate the distribution of Ti and Zr inside the MOF crystals, average atomic composition analysis is done on three different locations of samples by the Energy dispersive X-ray spectroscopy (EDS), which is equipped with the Hitachi S-800 SEM. The accelerating voltage was 20 kV. To prevent electron charging, samples were gold-palladium coated by a Hummer X sputter coater for 45 seconds before SEM-EDS measurement.

It is well known that TiO_2-P25 has an indirect bandgap (86, 87). Therefore, from Eq. 1, n = ½ and plotting $[F(R)\cdot hv]^{1/2}$ as a function of E = hv will deliver a slope intercepting x-axis at the bandgap E_g of TiO_2-P25. Similarly, for direct bandgap materials, n = 2, and bandgap E_g is the interception of the slope with x-axis when plotting $[F(R)\cdot hv]^2$ as a function of E = hv. For MOFs, since it is a hybrid material which contains both inorganic (metal-containing SBU) and organic parts (linkers), it is generally considered to have a direct bandgap (31, 88).

Conduction band potentials of MOF photocatalysts were measured using photoelectrochemical method to obtain the flat-band potential (V_{fb}) (89, 90). The photovoltaic cells were constructed similar to a Gratzel cell but without dye to avoid interaction of MOF with the dye as has been previously described in literature (28, 32, 91, 92). The working electrode was fabricated by depositing a paste of photocatalysts (TiO_2-P25, Zr-MOF or Ti/Zr-MOF) in 200-proof ethanol (Sigma Aldrich) on a cleaned transparent fluorine doped tin oxide (FTO) glass by via doctor blading technique. Sticky tape was used to control the layer area and the thickness of the working electrode (1x1cm^2 area and 25µm thickness). The electrode was then dried in vacuum oven at 100^oC for 30 minutes. The platinum counter electrode was made by dropcasting 2mg/ml H_2PtCl_6 (99.9% Sigma Aldrich) in ethanol on a FTO glass and then was annealed in oven at 425^oC for 1hr. Two electrodes were sealed together by a sealant (Solaronix) with a thickness of 50µm. I^3/I^{-3} electrolyte was injected between two electrodes. The current-voltage (I-V) curve was recorded by 600 Reference Gamry potentiostat. A 150W Xenon lamp was used to illuminate the cells. To make sure the measured open-circuit voltages corresponding with the flat-band voltages, which happens when the light

intensity is high enough (89, 90, 93), The light intensity was varied from 50%-100% by metal wire gauzes. At higher 80% light intensity, the open-voltage did not change for all tested photocatalysts, which indicates the measured open-voltage to be close to the flat-band potential. Thus, all I-V curves were reported at 100% light intensity. The potential data are plotted relative to the normal hydrogen electrode (NHE).

Calculation of FF (fill factor): $FF = \frac{P_{MAX}}{I_{SC} \times V_{OC}}$

where P_{MAX} is maximum power, which is the largest value of measured current times applied voltage, I_{SC} is short-circuit current, V_{oc} is open-circuit voltage.

3.2.2 Photocatalytic Reactivity for CO_2 Reduction with H_2O

The reaction was carried out in a stainless steel batch reactor with a quartz window on top. Typically, 50mg of catalysts was uniformly spread on a 1 in^2 base area of the reactor. Gaseous 99.99% CO_2 (Airgas) was bubbled through DI water at room temperature before introduction to the reactor. The amount of water vapor in the gaseous mixture was calculated to be 3% based on Raoult's law. Before the experiment, the reactor was evacuated. Then, water saturated CO_2 was flowed through at 2ml/min for 30 mins to achieve stability. The reaction was carried out at 20 psi, under irradiation of 150W Xenon light equipped with 1.5AM filter and a visible long pass filter (λ >400nm) for 6 hrs. Light intensities and spectrum at the catalyst surface were recorded using a blab la and blab Sensor and blab al respectively. The reactor was cooled by flowing water to maintain isothermal reaction temperature at 40^oC. Control runs were performed under the following conditions and no CO or CH_4 formation was observed: 1) under dark condition, and 2) with only N_2 and H_2O vapor when under

irradiation. 80µl gas samples were periodically removed by gastight syringe (Hamilton, 100ul) for analysis by gas chromatography (Agilent 6970C) with a thermal conductivity detector (TCD), equipped with a HP-Plot column. The limitation of detection is ~40ppm for both CO and CH_4.

The photochemical quantum yields (η %) of CO_2 reduction to CO and CH_4 under solar irradiation were calculated using the following equation(94):

$$\eta_{CO \text{ or } CH_4}(\%) = \frac{n * \text{moles of reduction products (CO or } CH_4)}{\text{moles of photon incident on catalyst}} * 100\%$$

where n is the number of electrons required to convert CO_2 to CO or CH_4, which are two and eight, respectively.

The number of photons for each wavelength from λ = 400nm-1100nm irradiated on the catalyst surface per second per unit area was calculated from the light intensity (~56 $mW.cm^{-2}$) measured by Li-200R Pyranometer (active from 400-1100nm, Li-COR) and the 150W Xenon light spectrum measured with filter at the catalyst surface (Figure 12). Because the IR section of the 150W Xenon light spectrum (λ> 750nm) generates heat and its effect was eliminated by controlling the reaction at a constant temperature (40^oC), and the long filter glass used in the experiment setup evokes any light wavelength at λ < 400nm (E_{hv} > 3.1eV), only photons with the wavelength in the visible range λ = 400nm-750nm are accounted for generating unbound electron−hole pairs in the Ti/Zr-MOF-525 photocatalyst and were used to calculate the quantum yield. This value was then compared to TiO_2-P25 efficiency found in literature.

3.3 Results and Discussion

3.3.1 Structural and Optical Characterization

The molar ratio of Ti:Zr in Ti/Zr-MOF-525 is 90:10, measuring by energy-dispersive X-ray Spectroscopy (EDS) (Figure 16). Power XRD (Figure 14) confirm the synthesized material structures as predicted in simulations (Mercury 3.3). Both precursor Zr-MOF-525 and its Ti-ion exchanged MOF-525, Ti/Zr-MOF-525 are highly porous. Their BET surface areas (Table 1) are 2492m^2/g and 2780m^2/g respectively, and their Langmuir surface areas 3134m^2/g and 4202m^2/g, respectively, which are comparable to that reported in the literature (27). The similarity of XRD results and surface areas between Zr-MOF-525 and Ti/Zr-MOF-525 confirm that the Ti atoms replaced Zr atoms in the SBU after the ion exchange process rather than blocking the pores of MOFs. Solid state Uv-vis absorbance shows MOFs optical properties are highly regulated by their porphyrin linkers (Figure 17). The absorption bands ranging from 400nm-750nm imply the MOFs ability to absorb light deep in the visible range. Signature spectra of four Q bands as expected from the π- π* transitions in metal-free porphyrin (56, 95) are also observable in Zr-MOF-525 and Ti/Zr-MOF-525 at a range from 490nm-670nm. These Q bands of porphyrin in MOFs are more defined and intense than from pure porphyrin (95), indicating a high number of π- π* transitions in MOF frameworks. This enhances the adsorption of visible light range in MOF. Significantly high intensity of porphyrin Q-bands in MOF structures in comparison with molecular porphyrin was also observed elsewhere in literature (56), though it is less eminent than in our Zr-MOF-525 and Ti/Zr-MOF-525. Two broad bands at 370nm and

450nm are assigned for the Soret band (S_0-S_2 absorption process), a characteristic band of free-base porphyrin (95).

To estimate the ability of MOF-525 to absorb visible light, optical band gaps were calculated from the UV-Vis solid-state absorption spectra of these MOFs by plotting the Kubelka-Munk function versus the energy of incident light in eV (Inserted in Figure 17). The bandgaps of Zr-MOF-525 and Ti/Zr-MOF-525 are extrapolated to be 1.7 eV (729 nm). The narrow bandgaps in MOFs are influenced strongly by the ligand.(31, 88) In the case of MOF-525, the measured bandgaps (1.7 eV) closely resemble the optical absorbance spectrum of free base meso-tetra (4-carboxylphenyl) porphyrin (TCPP) which has a UV-vis absorption band (a Q band) at 645 nm or 1.9 eV (95),(96). The values are red-shifted in respect to the free-base porphyrin ligand (H_2TCPP), due to the influence from coordinating with metal ions forming SBUs. This small band gap value allows Zr-MOF-525 and Ti/Zr-MOF-525 to be excited in the visible spectrum.

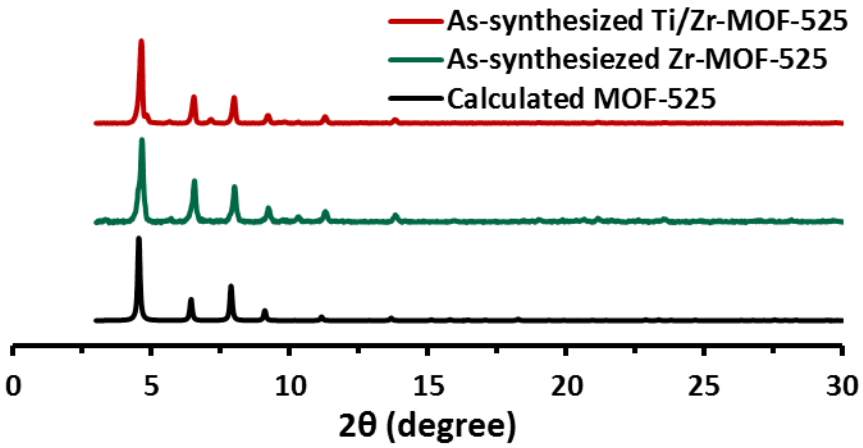

Figure 14: MOF PXRD results. a) of synthesized Zr-MOF-525 and Ti/Zr-MOF-525 versus that of simulated Zr-MOF-525

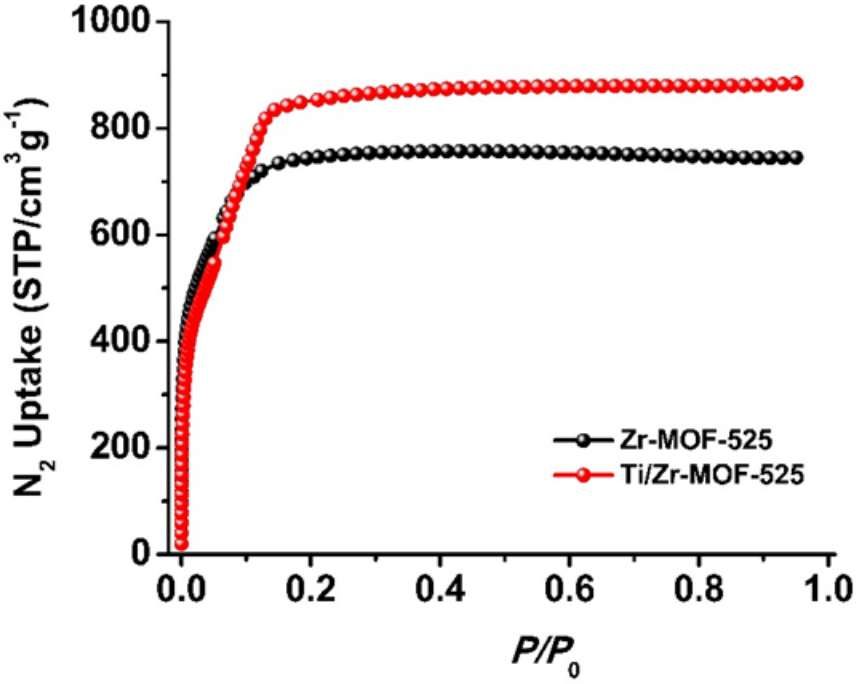

Figure 15: N_2 isotherm results of synthesized Zr-MOF-525 and Ti/Zr-MOF-525

Table 1: Physiochemical properties and measured band gaps and band edges of synthesized Zr-MOF-525 and Ti/Zr-MOF-525

Sample	Molar ratios[a] Zr:Ti	BET SA[b] (m^2/g)	Langmuir SA[b] (m^2/g)	Bandgap[c] (eV)	Conduction band Potential[d] Vs. NHE (eV)	Valence band Potential[f] Vs. NHE (eV)
Zr-MOF-525	100 : 0	2492 ± 53	3134 ± 50	1.7	-0.26	1.44
Ti/Zr-MOF-525	10 : 90	2780 ± 30	4202 ± 73	1.7	-0.52	1.18

[a]Determined by EDS results on three locations and then, averaged

[b]Determined by N_2 physisorption

[c]Determined by DRS_UVvis spectroscopy

[d]Determined by conduction band potential measurement experiment

[f]Calculated from bandgap and conduction band potentials

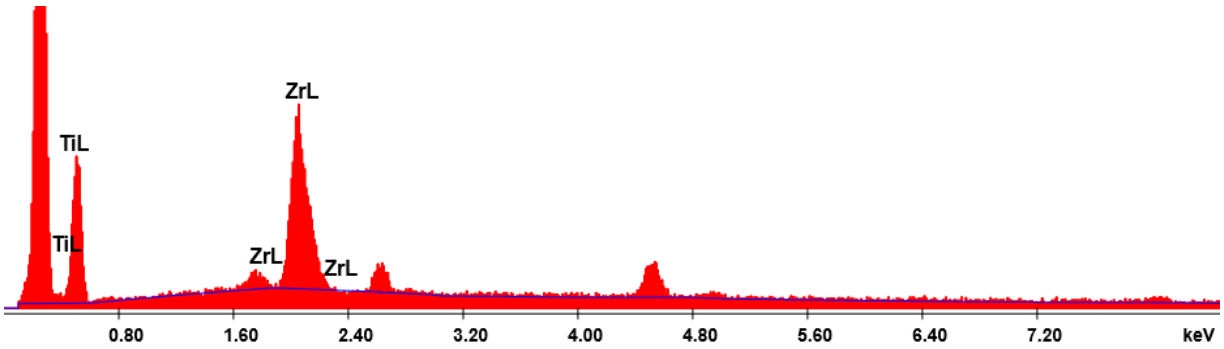

Element	Wt %	At %	K-Ratio	Z	A	F
TiL	81.42	89.30	0.4353	1.0116	0.5285	1.0001
ZrL	18.58	10.70	0.1576	0.9450	0.8871	1.0115
Total	100.00	100.00				

Element	Net Inte.	Bkgd Inte.	Inte. Error	P/B
TiL	18.52	2.15	3.05	8.60
ZrL	83.62	11.05	1.45	7.57

Figure 16: EDS results of Ti/Zr-MOF-525

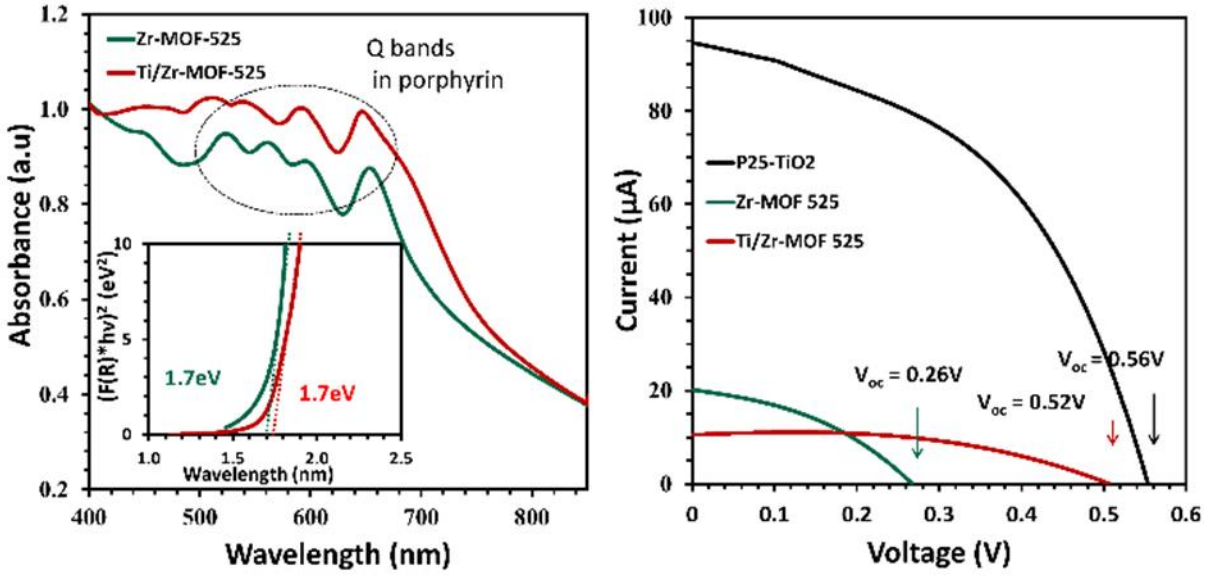

Figure 17: Optical bandgap measurement and conduction band potential experiment results. a) UV-vis solid-state absorption spectra of Zr-MOF and Ti/Zr-MOF. Insert shows the optical band gap energies of Zr-MOF-525 and Ti/Zr-MOF-525 which equal to 1.7 eV. b) I-V curves obtained for the photovoltaic solar cell prepared from TiO_2-P25, Zr-MOF-525, and Ti/Zr-MOF-525. Cells were irradiated with an AM 1.5-filtered Xenon lamp (150W) at radiation power of ~ 100W/m^2

For CO_2 photoreduction to occur, the catalyst is required to have a suitable conduction band and valence band, which are thermodynamically favorable for CO_2 conversion. Their open circuit potentials were measured and compared with that of TiO_2-P25. For n-type semiconductors, when illuminated under sufficiently high-intensity light, the quasi-Fermi level (measured as its open-circuit potential, V_{OC}) becomes close to the potential of the conduction band (93),(89, 90). This open-circuit potential is also called flat-band potential (E_{FB}) due to the elimination of conduction and valence band bending at the interface of electrolyte-semiconductor. The conduction bands of two MOFs were determined by comparing the open circuit voltages of photovoltaic cells made of Zr-MOF-525 or Ti/Zr-MOF-525 with the TiO_2-P25 cell (28, 32). In Figure 17b, the V_{OC} of Zr-MOF-525 and Ti/Zr-MOF-525 are 0.3 eV and 0.05 eV less than that of TiO_2-P25. After accounting for the conduction band of TiO_2-P25, which is -0.56eV versus NHE (pH = 7) (97), the conduction band edge of Zr-MOF-525 and Ti/Zr-MOF-525 were calculated to be -0.26 eV and -0.51 eV (versus NHE, pH = 7), respectively. While the bandgaps in our MOFs are clearly dictated by their ligands, they have relatively close band edge energies despite the differences in band edge positions of the metal oxides (ZrO_2 and TiO_2) (98). Simulation studies have shown that the band edges depend significantly on the configuration between the organic ligands and the SBUs (33, 99). Valence band potentials (V_{VB}) were then calculated from the conduction bands (V_{CB}) and bandgap (E_g) by applying the equation $V_{VB} = V_{CB} + E_g$ and are shown in Figure 19.

In Figure 17b, both MOFs generate much smaller photocurrent density than TiO_2-P25 in the I-V experiment. We interpret these data to suggest that these MOFs deliver

less charge carriers to the interface of the photocatalysts and electrolyte. This limitation lowers the efficiency of their photoreactions as observed in CO_2 photoreduction reactivity experiments.

CO_2 photoreduction were carried out in a batch reaction under irradiation using a 150 W Xenon lamp with a visible long pass filter (λ >400nm) . The CO_2 photoreduction results of Zr-MOF-525 and Ti/Zr-MOF-525 with the generation of CH_4 and CO are shown in Figure 18a. Background experiments included a blank run of catalysts with only N_2 and H_2O vapor under irradiation, a control run of catalysts with CO_2 and H_2O under dark conditions and a test run of free base porphyrin (H_2TCPP) under the CO_2 photoreduction conditions. No formation of CO or CH_4 was observed for these controls, which validated our observed CO and CH_4 formation using MOF-525 during CO_2 photoreduction experiments. The reactivity of TiO_2-P25 was also included for comparison due to its common use as photocatalyst for CO_2 reduction with H_2O. Negligible production of CH_4 occurred over TiO_2-P25, which is in agreement with a previous report.(80) This lack of activity was attributed to the large band gap (3.1 eV) of TiO_2-P25. In the 1st half hour, the production rate of Ti/Zr-MOF-525 is 1.52 $\mu mol.hr^{-1}.g^{-1}$ CH_4 (2865$ppm.hr^{-1}.g^{-1}$) and 0.33 $\mu mol.hr^{-1}.g^{-1}$ CO (630$ppm.hr^{-1}.g^{-1}$). The overall production of CH_4 and CO after six hours under visible-light irradiation by Zr-MOF-525 was measured at 437 ppm g^{-1} and 333 ppm g^{-1}. Likewise, Ti/Zr-MOF-525 showed 4119 ppm g^{-1} CH4 and 1423 ppm g^{-1} CO, respectively. The overall photocatalytic activity of Ti/Zr-MOF-525 for CH_4 is 9.5 times higher than the parent Zr-MOF-525. Ti/Zr-MOF-525 reactivity showed high selectivity toward CH_4 than CO. Since CH_4 is much more energy-valuable than CO, Ti/Zr-MOF-525 presents a beneficial impact forward in the search for

better photocatalysts. The photochemical quantum efficiency for CH_4 and CO of Ti/Zr-MOF-525 catalyst was calculated to be 0.0203% and 0.0011%, respectively. The total quantum efficiency (ηCO + ηCH4) under only visible light is 0.0214%. These results are comparable to TiO_2-P25 under full solar spectrum irradiation (80, 100).

The energy level alignment for TiO_2-P25, Zr-MOF-525 and Ti/Zr-MOF-525 ere illustrated in Figure 18b and this represents the observed photoreactivity results from CO_2 reduction. TiO_2-P25 was not photo active under visible light to generate the electron-hole (e^-/h^+) pair. Zr-MOF-525 has a suitable band gap (1.7 eV, 729nm) to absorb visible light and it possibly generated the e^-/h^+ pair under visible light; however, its band edge positions are not thermodynamically suitable for CO_2 reduction. Consequently, we observed some reactivity, but its photocatalytic activity toward CO and CH_4 production is substantially inferior to Ti/Zr-MOF-525. Finally, Ti-MOF-525 exhibited proper bandgap and band edge positions for CO_2 photoreduction synthesis of CO and CH_4.

The CO_2 photoreduction mechanism remains a complicated topic in the literature. A proposed mechanism for MOF catalyzed CO_2 and H_2O conversion into CO and CH_4 in Figure 19. After absorbing visible light, the porphyrin ligands generate the associated excited electrons (56), which migrate and transfer to the metal-containing SBUs nearby through a linker-to-cluster-charge-transfer process(28) to reduce Ti^{4+} in the Ti-O cluster to Ti^{3+} (35, 58, 101). This separation process of generated e^-/h^+ pair in a MOF has been proven to benefit the reactivity during photocatalysis (35, 82). Then, CO_2 molecules adsorbed in the MOF pores are readily reduced by Ti^{3+} to form adsorbed CO species, which desorb into free CO or further react with H^+ generated from the oxidation

of H_2O to form CH_4 (3, 35). The porphyrin ligands remain positively charged and oxidize water (102, 103). Because CO tends to adsorb strongly to the metal cluster (104), it is more likely to remain adsorbed and some would react further to form CH_4 and O_2, a reaction that requires lower energy to occur. This agrees well with what is observed in Figure 18a, where CH_4 formed 3 times as much as the CO product. Over time, strong CO adsorption would block active sites and could be the reason for the decline in CH_4 production after 2 hours of illumination. The low reactivity can also be explained by a slow process of transferring e^- and H^+ from the porphyrin ligands to the metal-containing nodes. Nonetheless, future detailed mechanistic studies to probe the intermediates during the CO_2 reduction is needed to verify these hypotheses

3.4 Conclusions

We have demonstrated, for the first time, the ability of porphyrin-based Ti/Zr-MOF-525 to reduce CO_2 in H_2O to gaseous chemical fuels (CH_4 and CO) without the presence of any sacrificial agents and using only visible light. The results show the tunability of MOF by using suitable linkers and metals in secondary-building-units in order to obtain desired bandgap and band edges for effective photocatalytic reactions. The reaction produces selectively more CH_4 versus CO and no sacrificial reagents are required.

While the yields are low, the approach shows great potential for designing linkers and nodes that can lead to much enhanced photoreduction capability.

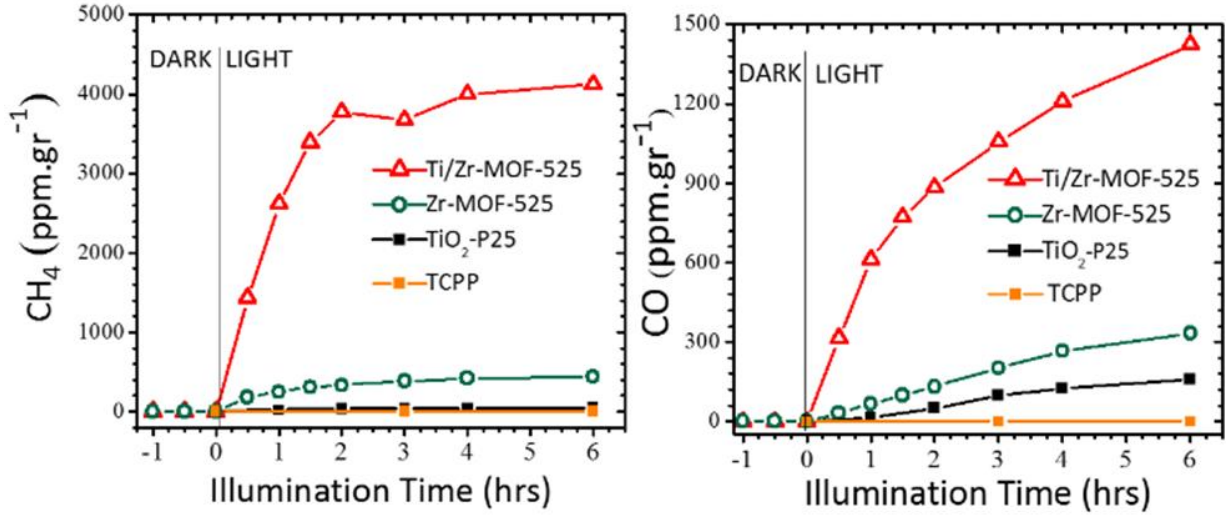

Figure 18: CO_2 photoreduction reactivities of MOF-525. (a) CH_4 and (b) CO production using Zr-MOF-525, Ti/Zr-MOF-525, TiO_2-P25 and H_2-TCPP under visible light illumination (λ>400nm) of a 150 W Xenon lamp at 40°C, 20psi. TiO_2-P25 reactivity was included for comparison.

.

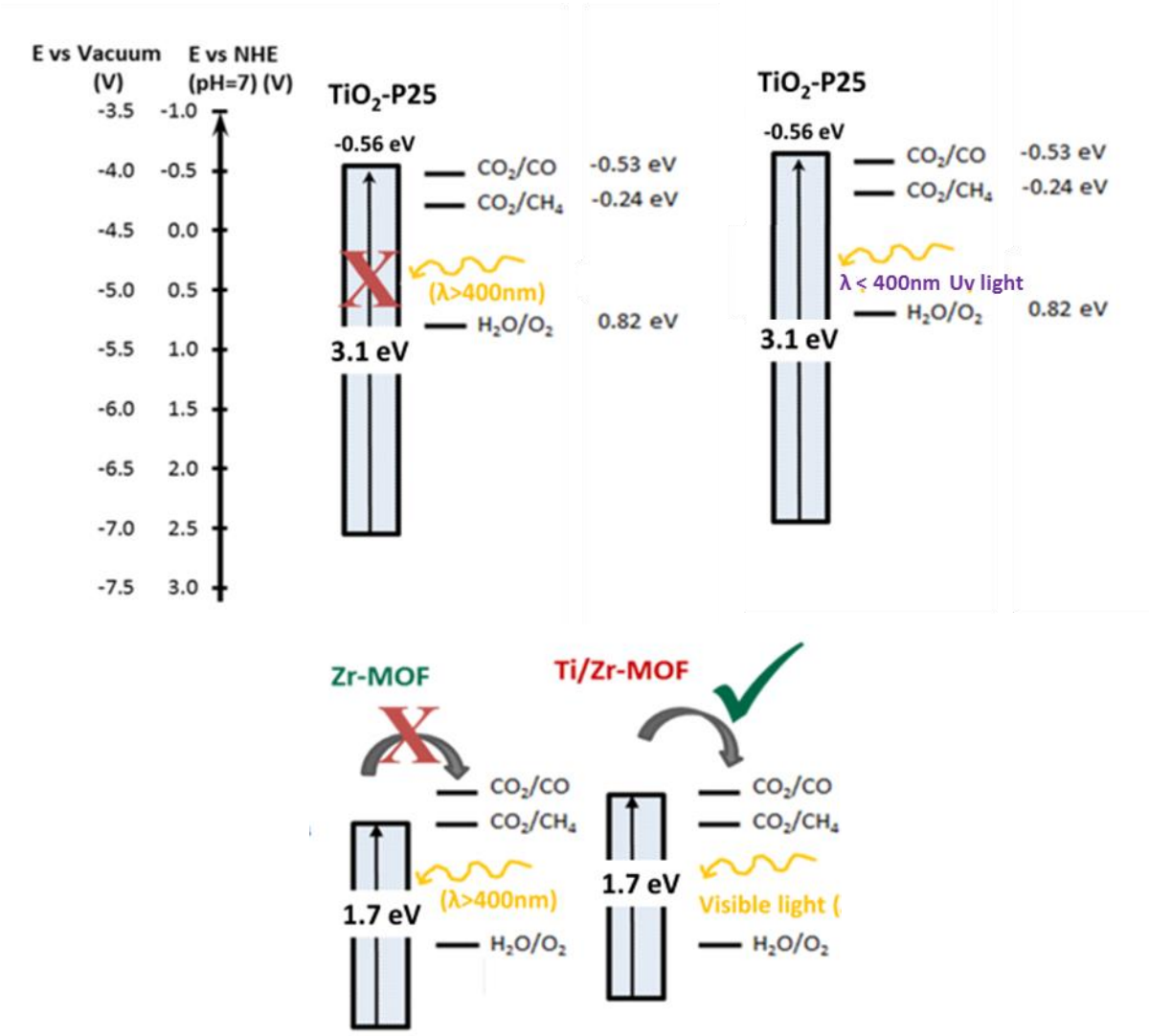

Figure 19: Diagram to explain the Ti/Zr-MOF-525 photoreactivity for CO_2 reduction with water. a) TiO_2-P25 has a large bandgap, therefore when illuminated under visible light (λ>400nm), it is not active. However, when illuminated under UV light (λ<400nm), TiO_2-P25's proper aligned energy levels (CB and VB) allows its reactivity for CO_2 photoreduction with water. b) Similarly, results from Figure 18 suggests that Ti/Zr-MOF-525 has suitable energy level alignment for CO_2 reduction with water under illumination.

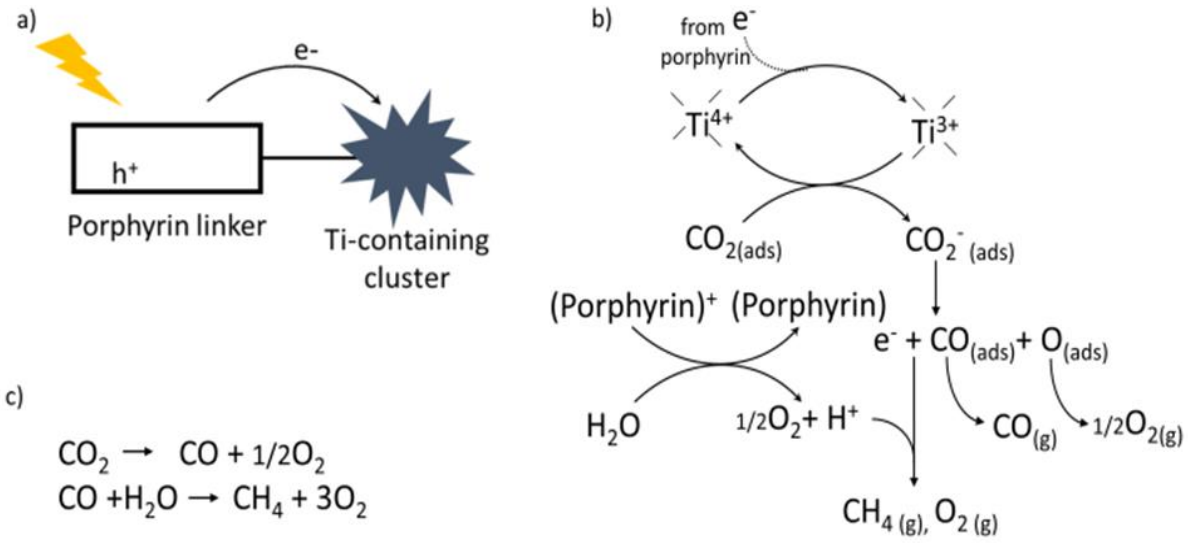

Figure 20: Overall CO_2 photoreduction mechanism by MOF photocatalyst. a) Scheme of charge transferred process within MOF when excited by illumination. b) Proposed CO_2 photoreduction mechanism catalyzed by Ti/Zr-MOF-525. c) Overall reaction of CO_2 reduction with H_2O to CH_4 and CO

CHAPTER 4: STABILITY STUDY OF TI/ZR-MOF-525 PHOTOCATALYST

4.1 Introduction

Metal-organic-frameworks have received intensive research interest thanks to their aesthetic framework structure and its flexibility to engineer for different applications such as gas storages and catalysis. Due to the nature of MOF, hybrid compounds between metal oxides and organic ligands, their biggest weakness is their stability under thermal effects or under guest solvent removal (105-107)

CO_2 photocatalytic reduction process exposes MOF photocatalysts to water, to light, and to radicals and charges either generated by the incident light or as byproducts during the reaction occurs. This potentially affects the structure and the reactivity of MOF photocatalysts. In an ideal world, the photocatalyst should continue to make products as long as it is illuminated. In addition, it should be able to be regenerated and recycled after used.

In the previous chapter, Ti/Zr-MOF-525 proves to be an advanced photocatalyst over its precursor Zr-MOF-525 and the gold standard photocatalyst TiO_2-P25. However, after 2 hours, the production of CH_4 reaches a plateau value, indicating a reduction of photocatalytic activity of the catalyst. In this chapter, MOF photocatalyst is further investigated for its ability for regeneration and its reactivity after recycling. Ti/Zr-MOF-525 fresh and used are characterized utilizing multiple techniques.

4.2 Experimental Section

4.2.1 Procedure to Regenerate MOFs

To study the stability of Ti/Zr-MOF-525 photocatalysts, the samples were reused 3 times for CO_2 reaction (Figure 20). After each reaction, the samples were washed with ethanol and acetone several times to remove possible contamination and reaction residual, and then dried in vacuum oven at 120°C overnight and were characterized before and after the reaction

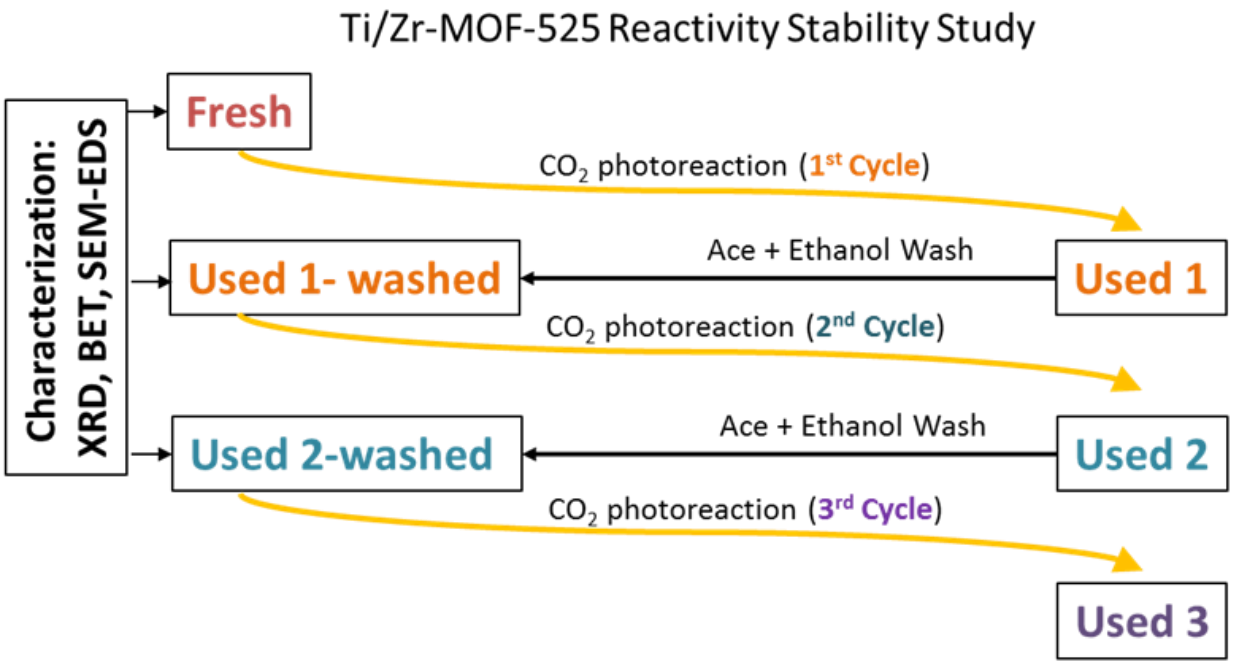

Figure 21: Ti/Zr-MOF-525 reactivity stability study procedure diagram

4.2.2 Characterization

The phase purity of catalysts was verified by Powder X-ray diffraction (PXRD) measurement on powder samples at room temperature using a Bruker D8 Advance X-ray diffractometer. The X-ray source was Cu Kα radiation (λ = 1.5406 Å). Diffraction patterns was recorded at a scan speed of 0.5 s/step (6°/min) and a step size of 0.05° in the 2θ range of 5° to 30°. The accelerating voltage and applied current were 20 kV and 5 mA, respectively. The simulated XPD patterns were produced using Mercury 3.6 software.

N_2 gas adsorption isotherms were collected at 77K using the Micromeritics Surface Area and Porosity Analyzer ASAP-2020. All the samples are degassed at 120^{o}C for 10 hours. The specific surface area was obtained by a multipoint BET method using the adsorption data in the relative pressure (P/P0) range of 0.05–0.3. Pore size distribution were determined by the density functional theory method (DFT).

Morphological observations were carried out on a Hitachi S-800 field emission scanning electron microscope (SEM, Hitachi, Japan). To investigate the distribution of Ti and Zr inside the MOF crystals, average atomic composition analysis is done on three different locations of samples by the Energy dispersive X-ray spectroscopy (EDS), which is equipped with the Hitachi S-800 SEM. The accelerating voltage was 20 kV. To prevent electron charging, samples were gold-palladium coated by a Hummer X sputter coater for 45 seconds before SEM-EDS measurement.

To study optical properties and measure the bandgap, the diffused reflectance spectrum (DRS) of catalysts were measured by a JASCO V-670 UV-vis-NIR spectrophotometer with the 60mm integrating sphere attachment at a wavelength range

from 200nm to 1100nm with a scan speed of 100nm.min^{-1}. Samples were spread in a thin layer and sandwiched between two microscopy glass slides.

The diffused reflectance UV-Vis spectra were used to calculate the Kubelka−Munk function, F(R) = (1 − R) 2/2R, where R is the percentage of reflected light(84). The incident photon energy (E = hv) and the optical bandgap energy (E_g) are related to the transformed Kubelka − Munk function in the following equation $[F(R)\cdot hv]^n = A (hv - E_g)$, where A is the constant depending on transition probability and n = ½ or 2 for indirect or direct bandgaps, respectively (84, 85).

4.2.3 Photocatalytic Reactivity for CO_2 Reduction with H_2O

The reaction was carried out in a stainless steel batch reactor with a quartz window on top. Typically, 50mg of catalysts was uniformly spread on a 1 in^2 base area of the reactor. Gaseous 99.99% CO_2 (Airgas) was bubbled through DI water at room temperature before introduction to the reactor. The amount of water vapor in the gaseous mixture was calculated to be 3% based on Raoult's law. Before the experiment, the reactor was evacuated. Then, water saturated CO_2 was flowed through at 2ml/min for 30 mins to achieve stability. The reaction was carried out at 20 psi, under irradiation of 150W Xenon light equipped with 1.5AM filter and a visible long pass filter (λ >400nm) for 6 hrs. Light intensities and spectrum at the catalyst surface were recorded using a blab la and blab Sensor and blab al respectively. The reactor was cooled by flowing water to maintain isothermal reaction temperature at 40^{o}C. Control runs were performed under the following conditions and no CO or CH_4 formation was observed: 1) under dark condition, and 2) with only N_2 and H_2O vapor when under irradiation. 80µl gas samples were periodically removed by gastight syringe (Hamilton,

100ul) for analysis by gas chromatography (Agilent 6970C) with a thermal conductivity detector (TCD), equipped with a HP-Plot column. The limitation of detection is ~40ppm for both CO and CH_4.

4.3 Results and Discussion

4.3.1 Structural and Morphological Changes

Characterization of the catalysts before and after each reaction recycle shows that no significant change in the solid-state UV-vis absorbance spectra and negligible change in XRD measurement were observed in the fresh and used photocatalysts (Figure 25 and Figure 22). This confirms that the Ti/Zr-MOF-525 structures and their electronic properties are preserved during the reaction. However, N_2 isotherm adsorption study (Figure 23) shows that phototcatalyst surface area has reduced by half after the 1st reaction cycle and then remains relatively unchanged in 2nd and 3rd cycles, agreeing with the observation of the reactivity behavior in Figure 27. The changes after the 1st cycles are also observed in the morphology as shown by SEM images, which indicate a reduction in particle size. Washing solvents of the used catalyst after the 1st cycle also contain a small amount of porphyrin, implying a leeching of the linker. All of these changes alleviate after the 1st cycle, marking the end of the framework breakdown. Used phototcatalysts become relatively stable during 2nd and 3rd cycles. After the 1st cycle, Ti/Zr-MOF-525 remained relatively stable, as observed by the lack of framework disruption and the maintenance of productivity at about 60-65% of its freshly prepared catalyst. Further catalytic investigation will bring insight to the mechanism and

pathway of CO_2 photoreduction in MOF, which will assist the design of future photocatalyst with improved stability and product selectivity.

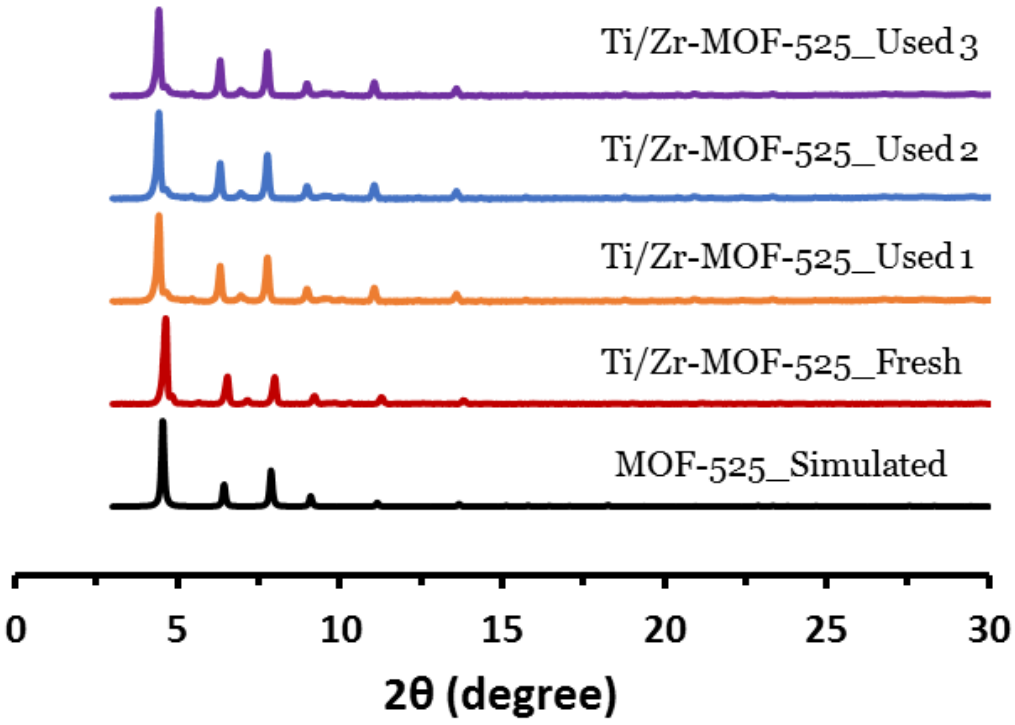

Figure 22: PXRD of fresh and used Ti/Zr-MOF-525 after each reaction cycle

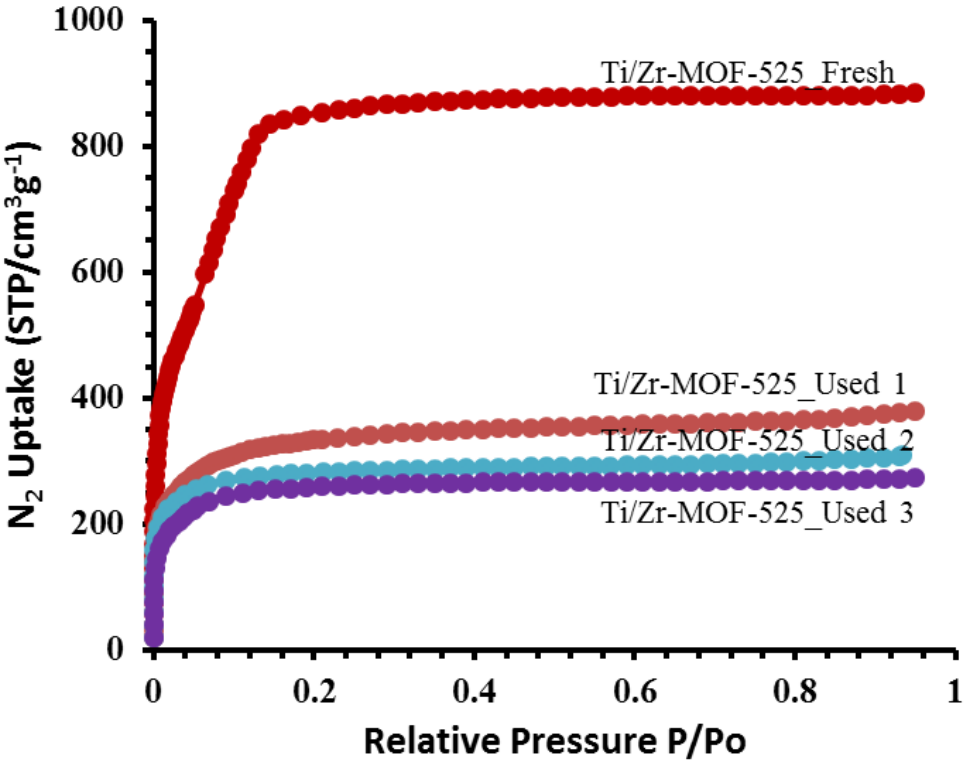

Figure 23: N_2 isotherm results of fresh and used Ti/Zr-MOF-525 after each reaction cycled

Table 2: Physiochemical properties and measured band gaps of fresh and used Ti/Zr-MOF-525

Sample	Molar ratios[a] Zr:Ti	BET SA[b] (m^2/g)	Langmuir SA[b] (m^2/g)	Bandgap[c] (eV)
Ti/Zr-MOF-525 Fresh	10 : 90	2780 ± 30	4202 ± 73	1.7
Ti/Zr-MOF-525 Used 1	11 : 89	1216 ± 18	1489 ± 19	1.8
Ti/Zr-MOF-525 Used 2	11 : 89	1070 ± 16	1256 ± 17	1.8
Ti/Zr-MOF-525 Used 3	11 : 89	970 ± 14	1171 ± 11	1.8

[a]Determined by EDS
[b]Determined by N_2 isotherm
[c]Determined by DRS-UVvis spectroscopy

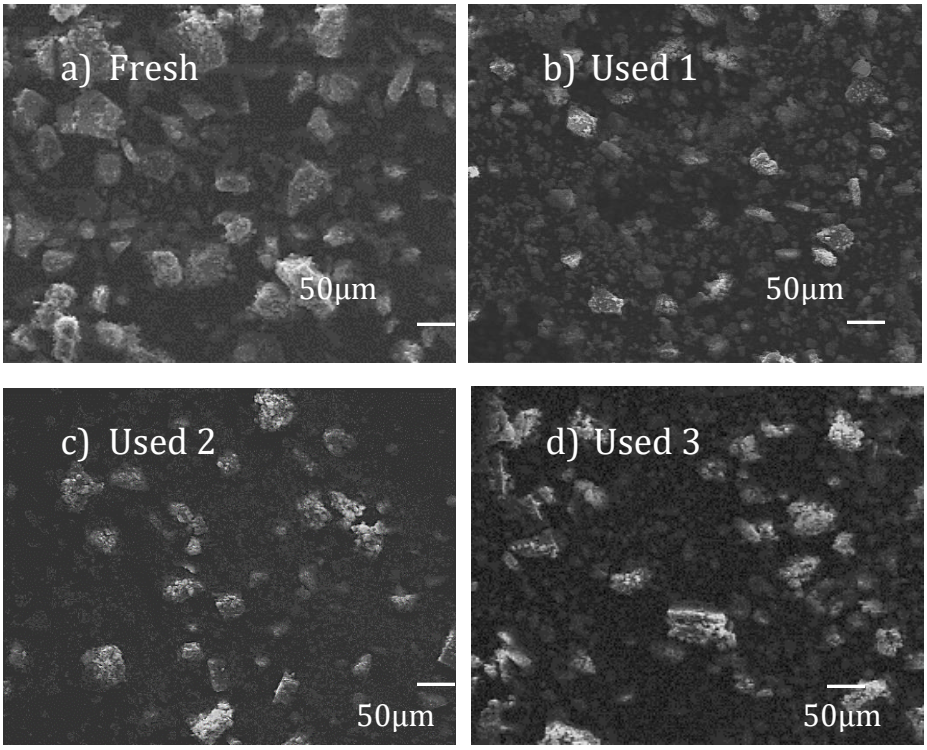

Figure 24: SEM images of fresh and used Ti/Zr-MOF-525 after each reaction cycle

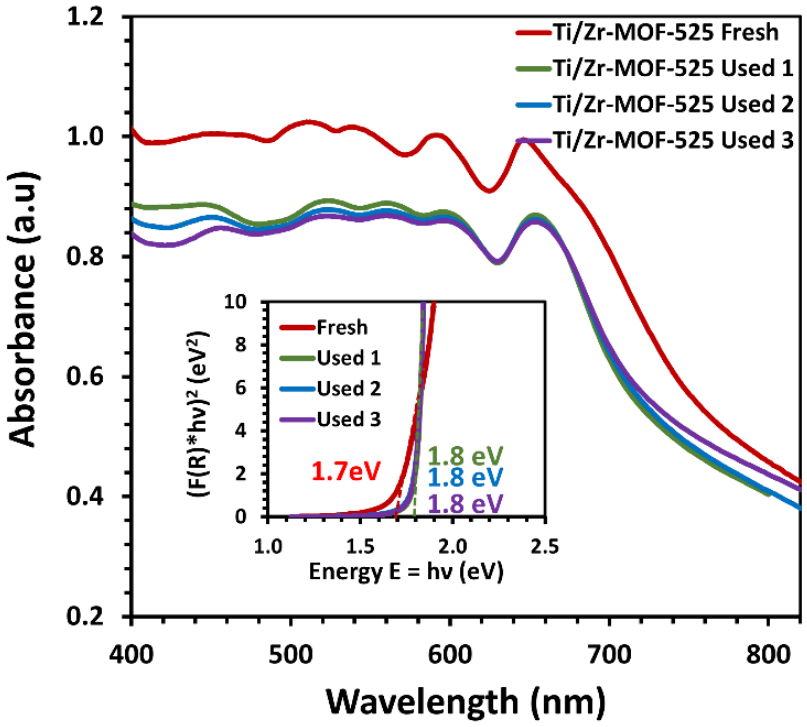

Figure 25: DRS_UVvis spectra of fresh and used Ti/Zr-MOF-525 before and after each reaction cycles. Inserted is the Tauc plot to measure the bandgaps.

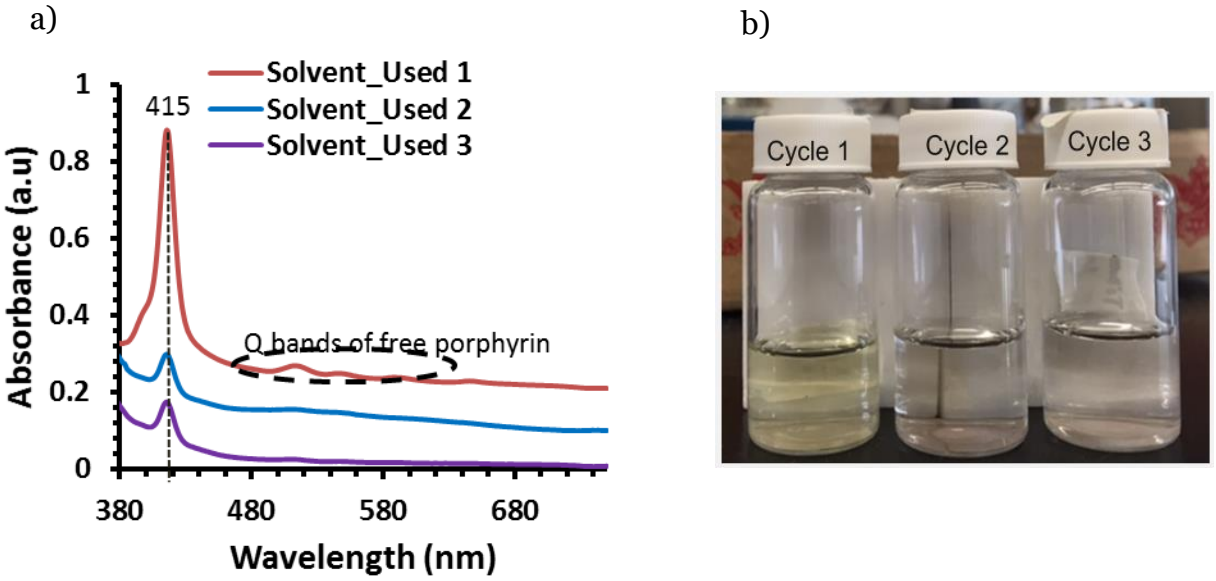

Figure 26: Washing solvent characterization. a) Liquid UV-vis spectroscopy results of washing solvents. b) Picture of washing solvents

4.3.2 Photocatalytic Reactivity Results

As seen in Figure 26 , the photoreactivity of used Ti/Zr-MOF-525 has reduced on average about 34% for CH_4 production and 40% for CO production in compared to fresh catalyst. However, after the 1st cycle, the photocatalyst maintains its reactivity in the 2nd and 3rd cycles, producing approximately 1.343 ± 0.035 μmol.gr^{-1} (~2534 ± 66 ppm.gr-1) CH_4 and 0.479± 0.063 μmol.gr^{-1} (~904 ± 118 ppm.gr^{-1}) CO after 6 hours of visible light illumination.

The second-cycled catalyst produces ~40% less CH_4 and CO than the fresh catalyst. The third cycled photocatalyst maintained similar reactivity with the second cycle, producing 1.255 ± 0.033 μmol.gr^{-1} (~2366 ± 61 ppm.gr^{-1}) CH_4 and 0.451± 0.038 μmol.gr^{-1} (~849 ± 72 ppm.gr^{-1}) CO after six hours of irradiation. Ti/Zr-MOF-525 maintained its structure as demonstrated in the solid-state UV-Vis absorbance spectra and PXRD patterns (Figures 21 and 22) between the fresh and recycled photocatalysts. This confirmed that the Ti/Zr-MOF-525 structures and its electronic properties are preserved during reaction. However, N_2 isotherm adsorption study showed that the phototcatalyst surface area reduced by half after the first reaction cycle and third cycles. This reduced surface area corresponded with the reduced reactivity behavior. Physical changes after the first cycle were observed in the morphology as shown in SEM images (Figure 23), which showed a reduction in particle size. The washing solvents contained porphyrin molecules from the MOF catalyst after the first cycle (Figure 25). We interpreted these observations to the breakdown of the material during photocatalysis, but the deterioration alleviates after the 1st cycle.

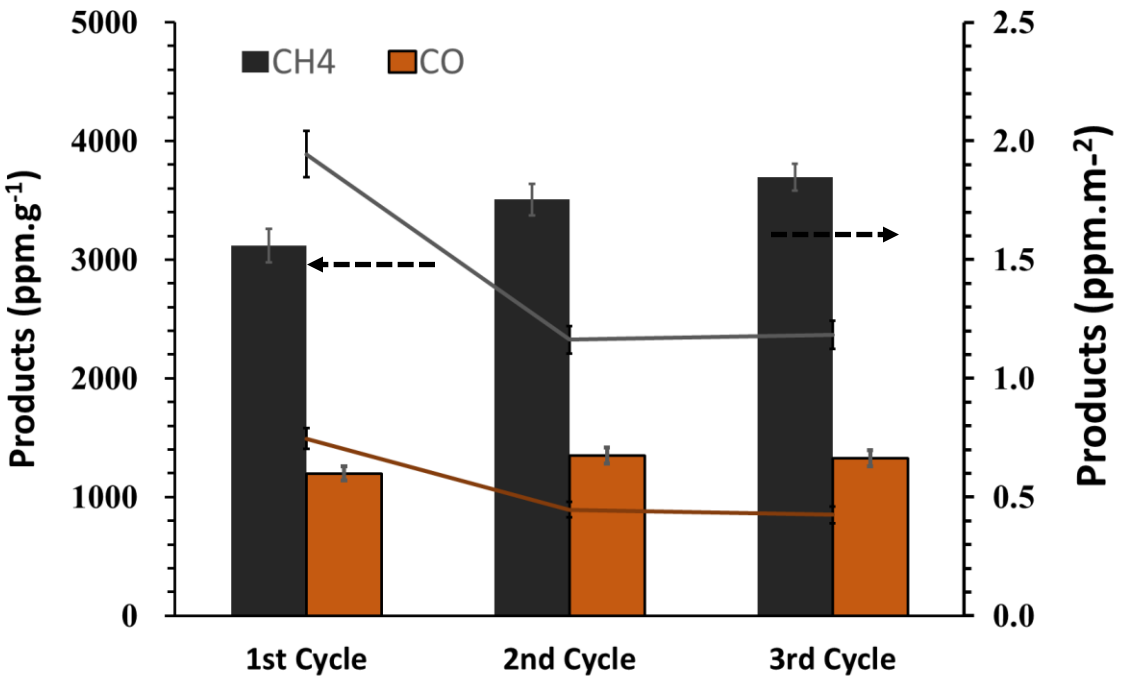

Figure 27: Total product yield of CO_2 photoreduction by Ti/Zr-MOF-525 on each reaction cycle. Legends: Lines-per mass of the catalyst. Columns-per surface area of the catalyst.

4.4 Conclusion

Ti/Zr-MOF-525 showed a ~34-40% deactivation after the first run, however it stabilized after that and subsequent regeneration steps were able to restore the activity. The surface area reduces significantly after the 1st cycle of reaction. However, the Ti-MOF photocatalyst maintains its surface area during 2nd and 3rd cycles of reaction. The production yields remain similarly in regards to its surface area, implying that intact MOF preserves its reactivity.

CHAPTER 5: CO_2 PHOTOREDUCTION STUDIES USING $LACR_{1-x}FE_xO_3$ PEROVSKITES: THE EFFECTS OF METAL RATIOS IN B SITE ON BANDGAPS AND BANDEDGES

5.1 Introduction

The ABO3-type perovskite can have the B site modified by partially substitute B with a similar B' cations. Modified perovskites can have altered electrical and chemical properties. This tunability of perovskites makes them a great material for engineering the bandgap,conduction, and valence band potentials for photocatalytic applications.

In addition, perovskites have thermal and chemical stabilities which are similar to regular metal oxides, making them comparable to TiO_2-P25 for reuse and photocatalyst applications under aquesous conditions.

$LaCrO_3$ has a conduction band potential negative enough for CO_2 conversion but it has a large bandgap (3.09eV) (108), making it less effective for absorbing solar energy. On the other hand, $LaFeO_3$ has a small bandgap due to its Fe-O bonds but an overly positive conduction band potential for CO_2 conversion. Thus, a combination of these two perovskites will provideinsight into the effects of site B substitution on chemical and electronic properties of the mixed perovskites.

In this study, $LaCr_{1-x}Fe_xO_3$ was investigated for its changes in bandgap and bandedge when gradually substituted Fe ions for Cr ions. Five perovskites with

different Cr/Fe ratios was synthesized where x = 0, 0.25, 0.5, 0.75, 1. Consequently, their CO_2 photoreactivities were studied in responses to Fe ion replacement.

Previously, Divya Suresh, a Master graduate student in our research laboratory has synthesized four $LaCr_{1-x}Fe_xO_3$ and tried to measured their bandgaps and bandedges (66). She observed a narrowing of band gap energy when increasing iron concentration. The band edges were also measured. However, the study is incomplete as only four samples with x = 0, 0.25, 0.5, 1 (missing x = 0.75) were synthesized and reported. Also, the Mott-Schottky plots were generated using only two frequencies (50Hz and 100Hz). As discussed on the methodology chapter (Chapter 2), it is important to obtain the Vfb over a range of frequencies. Therefore, the experimental limitations of the previous study were addressed and improved in this work. In particular, five perovskites with different Cr/Fe ratios were synthesized, where x = 0, 0.25, 0.5, 0.75, and 1. Mott-Schottky plots were obtained at least three frequencies.

5.2 Experimental Set Up and Characterization

5.2.1 Synthesis of the Perovskite Photocatalysts

$LaCr_{1-x}Fe_xO_3$ (x = 0, 0.25, 0.5, 0.75, 1) perovskite powders were synthesized using Pechini method, similarly described by Popa and Kakihana (65). Briefly, citric acid (Sigma Aldrich, ≥99.5%) was dissolved in 60^{o}C water. Then, appropriate amount of precursors La $(NO_3)_3$ (Sigma Aldrich, ≥99.9%), Cr $(NO_3)_3$ (Alfa Aesar, 99.9%) and Fe $(NO_3)_3$ (Sigma Aldrich, ≥98%) were added to the solution. The mixtures was continuously stirred at 60^{o}C for 2 hrs. After ethylene glycol (Sigma Aldrich, ≥99%) was added, the solution was raised to 90^{o}C and remained at this temperature for 7 hrs while

under constant stirring. The gel-like resin was transferred to the oven where it was heated at 450^{o}C for 2 hrs to decompose all the metal precursors, and then at 950^{o}C for 6hrs to form the final perovskite catalysts.

The molar ratios of materials used was La: citric acid: ethylene glycol = 1:10:40 as described in Yolanda et al. (67). The amounts of $Cr(NO_3)_3$ and $Fe(NO_3)_3$ precursors used were determined to target the metal molar ratios in $LaCr_{1-x}Fe_xO_3$ where x = 0, 0.25, 0.5, 0.75, 1.

5.2.2 Structural and Composition Characterizations

Synthesized perovskites were characterized for their surface area, porosity, crystal structures, morphology, and compositions. The phase purity of catalysts was verified by Powder X-ray diffraction (PXRD) measurement on powder samples at room temperature using a Bruker D8 Advance X-ray diffractometer. The X-ray source was Cu Kα radiation (λ = 1.5406 Å). Diffraction patterns was recorded in the 2θ range of 20° to 80° with a step size of 0.01° and an average time per step of 1s. The accelerating voltage and applied current were 20 kV and 5 mA, respectively.

N_2 gas adsorption isotherms were collected at T = 77K using a Quantachrome Autosorb IQ. Approximately 150mg of each perovskites were used for the measurement. The samples were outgassed at T = 250^{o}C for 10 hours to remove all water and other light volatile organic compounds during the washing process. The specific surface area was obtained by a multipoint BET method using the adsorption data in the relative pressure (P/P_o) range of 0.05–0.3. The BET (Brunauer-Emmett-Teller) method (69) considers both multilayer and monolayer adsorption.

Morphological observations were carried out on a Hitachi S-800 field emission scanning electron microscope (SEM, Hitachi, Japan). To investigate the distribution of metals, average atomic composition analysis is done on three different locations of samples by the Energy dispersive X-ray spectroscopy (EDS), which is equipped with the Hitachi S-800 SEM. The accelerating voltage was 20 kV. To prevent electron charging, samples were gold-palladium coated by a Hummer X sputter coater for 45 seconds before SEM-EDS measurement.

The FTIR spectra of the catalysts were obtained using a Nicolet IS50 Spectrometer in an attenuated total reflection (ATR) mode.

5.2.3 Optical Bandgap and Conduction Band Edge Measurements

To study optical properties and to measure the bandgap, the diffused reflectance spectrum (DRS) of catalysts were measured by a JASCO V-670 UV-vis-NIR spectrophotometer with the 60mm integrating sphere attachment at a wavelength range from 200nm to 1100nm with a scan speed of 100nm.min^{-1}. Samples were spread in a thin layer on the quartz window side of the powder sample holder cell (Jasco, PSH-002). A white Spectralon plate was used as reflectance standard background. The reflectance spectra were converted into Kubelka-Munk function (F(R)) which is proportional to the absorption co-efficient for low values of F(R).

Band edge potentials of photocatalysts were measured using Electrochemical Impedance Spectroscopy (EIS) to generate Mott-Schottsky plots for the flat-band potential (V_{fb}). To make the working electrodes, the powder catalysts were first grounded, mixed with ethanol and water, and sonicated for 30 minutes to yield a thick slurry. Then, the mixtures were spread via the doctor blade technique on a 2.5x1.5cm^2

pure titanium foil (Sigma Aldrich). The samples were then oven dried at 250°C for 5 hrs to yield a smooth thin film on the foil. A 2ml plastic tube was glued on the foil to hold electrolytes. The catalyst electrode area is 0.625cm^2. Titanium wire was used as reference and platinum wire as counter electrodes. The potential of the titanium wire reference electrode was later calibrated against Saturated Calomel Electrode (SCE) and it is +0.155V versus SCE. 0.1M Na_2SO_4 (pH ~7) was used as electrolyte. A potentiostat/galvanostat model Gamry 600 was utilized for the measurements using the EIS software from Gamry. Mott-Schottsky plots were obtained at several frequencies (1000Hz-2500Hz). Flatband potentials were determined by plotting inverse capacitance squared ($1/C_2$) as a function of voltage, which was found to be independent of frequencies for all samples. Conduction band edges (CB) were determined using standard equations from these flat band potentials. Valance bands (VB) are then calculated from measured bandgap (Eg) and conduction band (CB) using the equation: VB = CB – Eg.

5.2.4 CO_2 Photoreduction Reactivity

CO_2 photoreduction experiments were performed using a setup described previously(80). The reaction was carried out in a stainless steel batch reactor with a quartz window on top. Typically, 50mg of catalysts was uniformly spread on a 1 in^2 base area of the reactor. Gaseous 99.99% CO_2 (Airgas) was bubbled through DI water at room temperature before introduction to the reactor. The amount of water vapor in the gaseous mixture was calculated to be 3% based on Raoult's law. Before the experiment, the reactor was evacuated. Then, water saturated CO_2 was flowed through at 2ml/min for 30 mins to achieve stability before two valves at inlet and outlet of the

reactor were closed for a batch reaction. The reaction was carried out at 20 psi, under irradiation of 150W Xenon light equipped with 1.5AM filter and a visible long pass filter (λ >400nm) for 6 hrs. Light intensities and spectrum at the catalyst surface were Li-200R Pyranometer (active from 400-1100nm, Li-COR). The reactor was cooled by flowing water to maintain isothermal reaction temperature at 40^{o}C. Control runs were performed under the following conditions to ensure that the gas products CO and CH_4 are not from non-photo-catalyzed reactions: 1) under dark condition, and 2) with N_2 and H_2O vapor under irradiation. 80µl gas samples were periodically removed by gastight syringe (Hamilton, 100ul) for analysis by gas chromatography (Agilent 6970C) with a thermal conductivity detector (TCD), equipped with a HP-Plot column. The limitation of detection is ~40ppm for both CO and CH_4.

5.3 Results and Discussion

5.3.1 Crystal Structure and Physical Properties

The powder X-ray diffraction (PXRD) patterns of the synthesized perovskites are shown in Figure 27. $LaFeO_3$ and $LaCrO_3$ crystal structures match with the JCPDS X-ray pattern files (ICCD 01-088-0641 reference code for $LaFeO_3$ and ICCD reference code 00-026-0817 for LaCrO3). All synthesized perovskites have orthorhombic crystal structures and are single phase which agrees with previous finding (109) when Pechini synthesis method is used. Das et al.(109) reported that $LaMO_3$ (where M is metal) synthesized by Pechini routes always yield single phase and have orthorhombic crystal structure. Kato and Kudo(110) observed that orthorhombic phases in perovskite ABO_3 type accelerates the charge transfer of photogenerated e^-/h^+ pairs within crystals. This

is also the reason why Pechini method was chosen to synthesize the perovskite photocatalysts, to target single phase for suppression of e^-/h^+ pairs recombination and to promote orthorhombic structures for charge transfer. Orthorhombic structure is common for ABO_3 perovskite oxides due to the distortion caused by mismatch cation size in A and B sites from the ideal cubic structure (111). The clean XRD patterns indicate a high crystallinity of all five samples which promotes change mobility. Less defects from single phase and high crystallized materials also discourage charge recombination, which will lead to better photoreactivity (112, 113).

The calculated lattice constants from the XRD data are given in Table 3. The lattice parameters and unit cell volumes of perovskite increased with x (enriching Fe content) as the ionic radii of Fe is larger than Cr. This was also observed by others(67) when Fe replaces smaller metal atoms. XRD patterns at the major diffraction line (Miller indices [121]) in Figure 27b clearly display a peak shift toward smaller angle for Fe-enriching samples. No minor peaks observed at 2theta of 36.59 ^{o}, 38.42 ^{o} or 39.6^o, indicate no extra phases of La_2O_3, Fe_2O_3 and Fe_3O_4 (46) existed in these perovskites. The gradual change in lattice parameter and unit cell from $LaCrO_3$ to $LaFeO_3$, the consistency of single-phase orthorhombic structure, and the absence of metal oxide (La_2O_3, Fe_2O_3 and Fe_3O_4) peaks suggest that when x increases from 0 to 1, Fe replaces Cr sites on the B site rather than creating extra crystal structure or phases.

BET surface areas (Figure 28 and Table 3) are small across all five materials, which are observed in previous studies for perovskites when activated at high temperature(46, 67). They are strictly non-porous and homogeneous in size and shape.

The low surface area reduces the adsorption ability and therefore will affect the reactivity of perovskite as discussed below.

The metal compositions determined by EDS are within ±10% of the target ratios (Figures 29-33). EDS was taken at several spots and averaged to assure the representative of the data. The metal ratio variations between spots within a sample are small, around ~3% of the values, indicating the homogeneity of the sample composition.

The IR spectra of perovskite nanoparticles synthesized at different ratios of Fe/Cr in the crystal structures are shown in Figure 34. No observed peak at about 1500 cm^{-1} which was ascribed to –COOH wag vibrations of the oxygen group carbonate (24), demonstrates that the sample do not contain a significant amount of impurity. The IR peaks at about 400 and 560 cm^{-1} are close related to the bending vibration of O–Fe–O and the stretching vibration of Fe–O, respectively (47, 49). These bands are characteristic of the octahedral FeO_6 group in $LaFeO_3$. No broad band observed at about 3400 cm^{-1} which is normally attributed to the stretching vibration of O–H of adsorbed water molecules indicates that the samples are certainly dry.

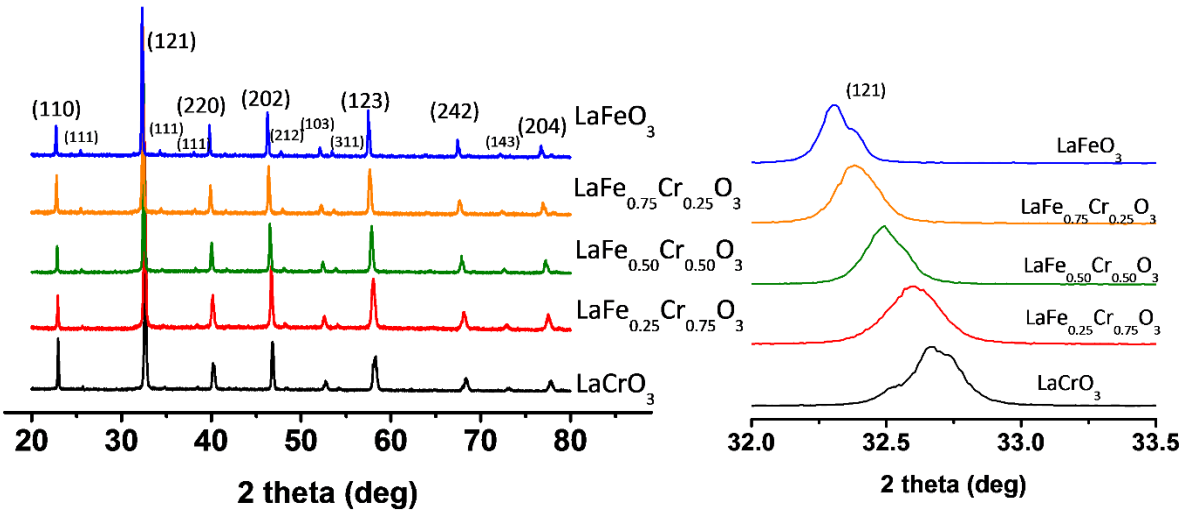

Figure 28: Perovskites' PXRD results. a) PXRD patterns of as-prepared five perovskites. b) Detailed PXRD patterns of the strongest diffraction peaks at around 2θ = 32 º - 33º

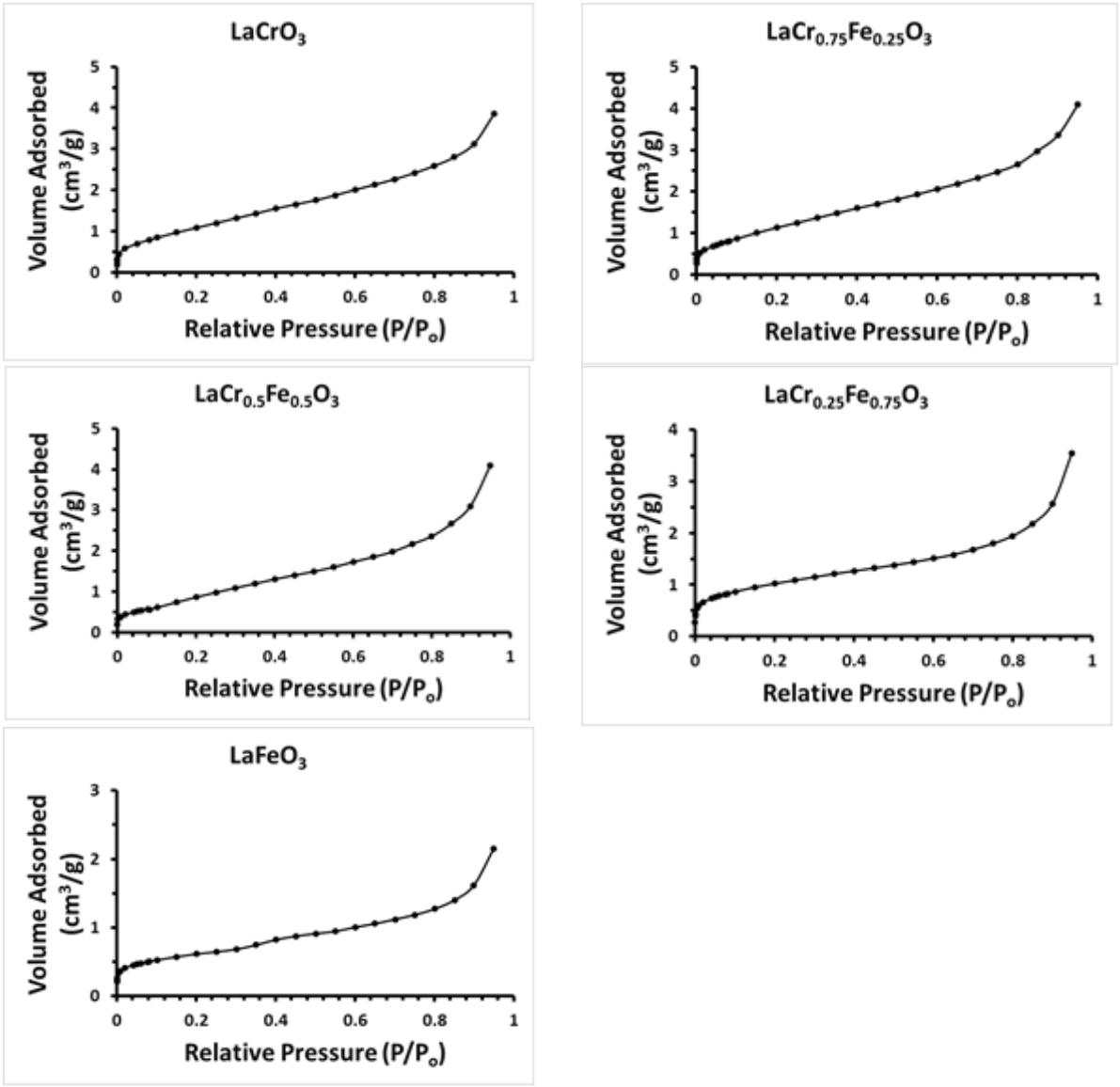

Figure 29: N_2 adsorption isotherms of $LaCr_{1-x}Fe_xO_3$

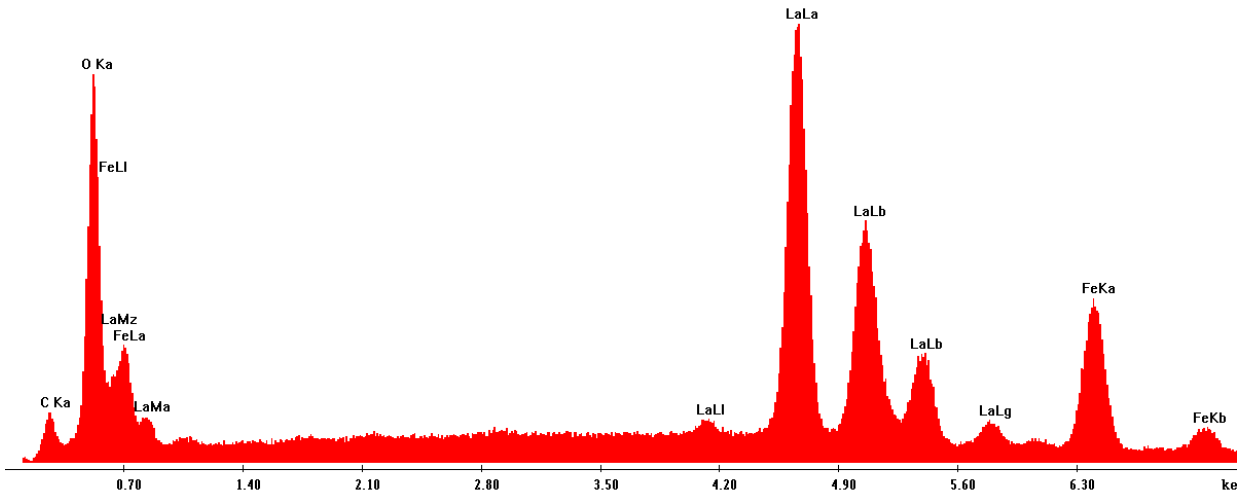

Element	Wt %	At %	K-Ratio	Z	A	F
C K	1.82	11.25	0.0077	1.3523	0.313	1.0001
O K	4.64	21.47	0.0327	1.3227	0.5317	1.0009
LaL	71.52	38.11	0.6629	0.9094	1.0098	1.0094
FeK	22.02	29.18	0.2381	1.147	0.9429	1
Total	100	100				

Element	Net Inte.	Bkgd Inte.	Inte. Error	P/B
C K	25.91	18.88	3.65	1.37
O K	261.74	85.31	0.94	3.07
LaL	686.48	0	0.45	686.48
FeK	271.04	0	0.72	271.04

Figure 30: EDS result at one spot of $LaFeO_3$ sample

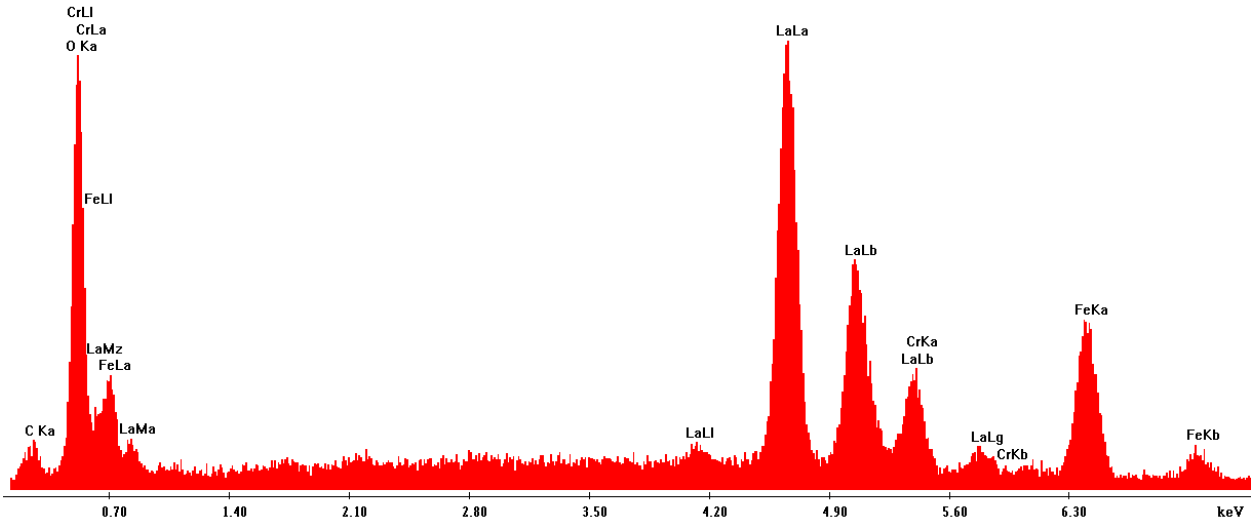

Element	Wt %	At %	K-Ratio	Z	A	F
C	0.90	5.49	0.005	1.3395	0.0954	1
O	3.60	21	0.0382	1.3102	0.364	1.001
LaL	70.60	37.41	0.3712	0.8994	1.0111	1.001
FeK	19.15	26.31	0.2409	1.1258	0.9865	1.059
CrK	5.96	9.79	0.0923	1.1335	0.9442	1
Total	100	100				

Figure 31: EDS result at one spot of $LaCr_{0.25}Fe_{0.75}O_3$ sample

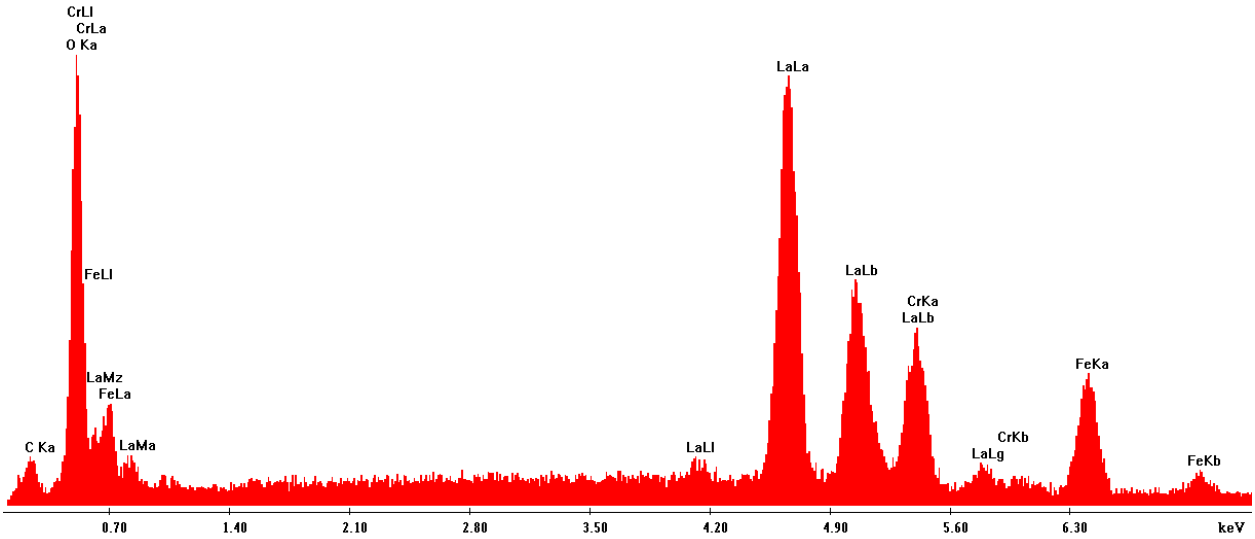

Element	Wt %	At %	K-Ratio	Z	A	F
C	1.30	7.9	0.0075	1.3395	0.2354	1
O	4.60	21	0.0382	1.3102	0.54	1.001
LaL	67.67	35.34	0.6212	0.8994	1.0111	1.003
CrK	14.09	18.39	0.1409	1.1258	0.9865	1.0159
FeK	12.35	17.37	0.123	1.1335	0.9442	1

Figure 32: EDS result at one spot of $LaCr_{0.5}Fe_{0.5}O_3$ sample

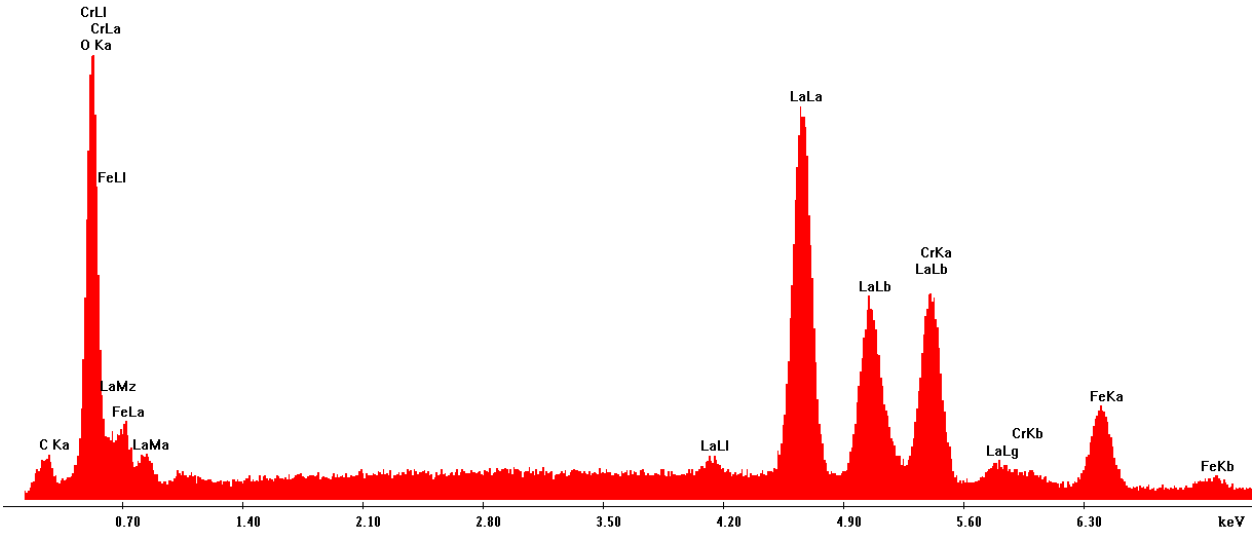

Element	Wt %	At %	K-Ratio	Z	A	F
C	1.29	7.89	0.0014	1.595	0.0954	1
O	4.38	20	0.0458	1.102	0.364	1.001
LaL	69.02	36.41	0.3602	0.947	1.011	1.001
FeK	6.52	8.51	0.0709	1.178	0.965	1.059
CrK	19.04	27.19	0.2345	1.0335	0.972	1
Total	100	100				

Figure 33: EDS result at one spot of $LaCr_{0.75}Fe_{0.25}O_3$ sample

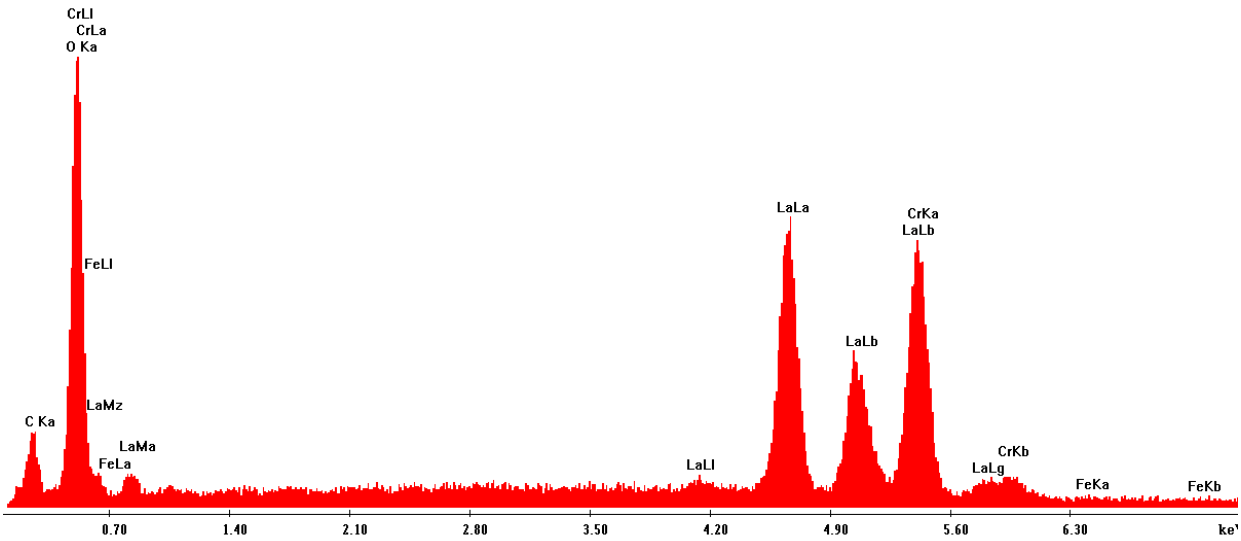

Element	Wt %	At %	K-Ratio	Z	A	F
C	2.86	11.35	0.001	1.950	0.054	1
O	7.91	27	0.0248	1.102	0.364	1.001
LaL	63.21	30.4	0.6302	0.947	1.011	1.001
CrK	26.23	31.25	0.2425	1.035	0.972	1
Total	100	100				

Figure 34: EDS result at one spot of LaFeO3 sample

Table 3: Crystallographic properties, metal compositions and Brunauer-Emmett-Teller surface areas of synthesized perovskite photocatalysts

Sample	Molar ratios[a] Cr : Fe	BET SA[b] (m^2/g)	Crystal Structure[c]	Lattice parameters (Å) [c]			Unit cell volume ($Å^3$)[c]
				a	*b*	*c*	
$LaCrO_3$	100 : 0	2.3	Orthorhombic	5.47	5.47	7.74	231.72
$LaFe_{0.25}Cr_{0.75}O_3$	76.7 : 23.6 (±1.1)	3.0	Orthorhombic	5.50	5.51	7.79	235.85
$LaFe_{0.5}Cr_{0.5}O_3$	52.2 : 47.8 (±1.8)	3.2	Orthorhombic	5.51	5.52	7.80	237.27
$LaFe_{0.75}Cr_{0.25}O_3$	26.8 : 73.2 (±0.5)	3.1	Orthorhombic	5.53	5.54	7.83	239.73
$LaFeO_3$	0 : 100	2.1	Orthorhombic	5.56	5.55	7.84	241.99

[a] Determined by EDS Scan, [b] Determined by N_2 physisorption, [c] Determined by XRD

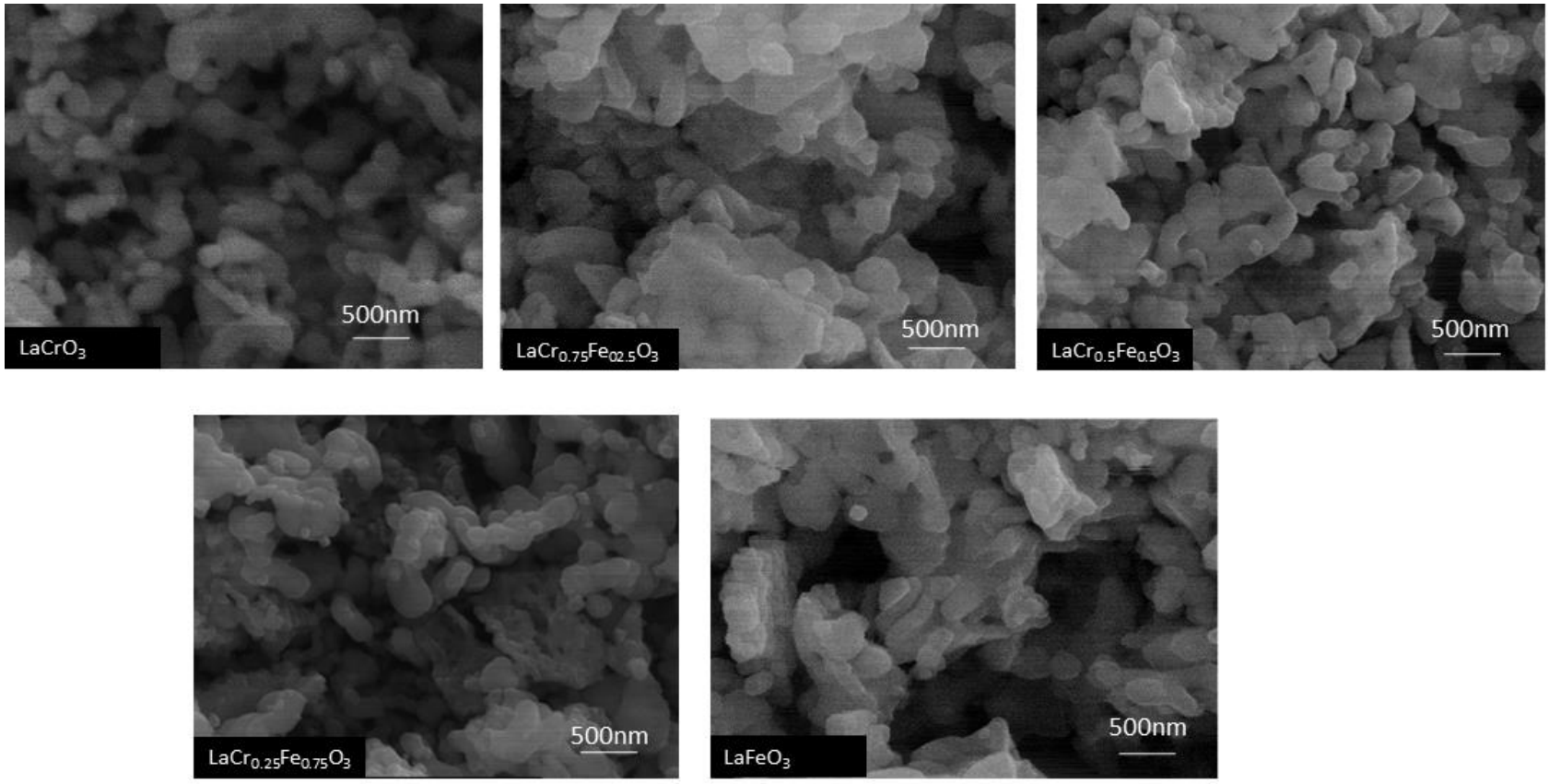

Figure 35: SEM images provides morphology of synthesized perovskites.

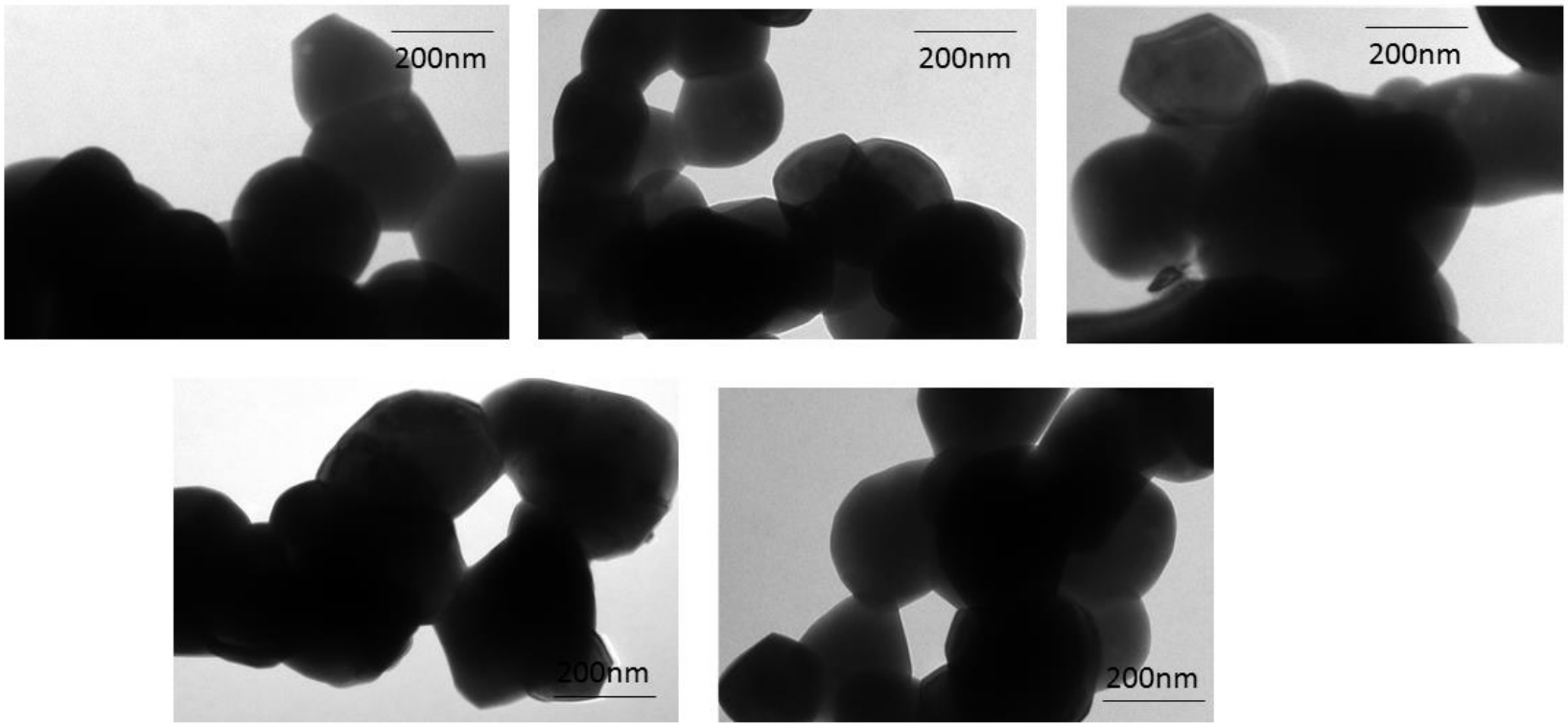

Figure 36: TEM images of five perovskites

5.3.2 Optical Bandgap and Positions of Conduction and Valence Band Potentials

Figure 37a shows the optical absorption spectra of five synthesized perovskites. The diffused reflectance Uv-vis spectra were used to calculate the Kubelka − Munk function(84), F(R) = (1 − R) 2/2R, where R is the percentage of reflected light (84). $LaFeO_3$ cuts off its light absorption at around ~550nm. It has a small adsorption band at 720nm, indicates a mid-band stage within the bandgap. This band was also observed for nanocrystal $LaFeO_3$ calcined at 500-950^oC (46, 47, 114). It is known that $LaFeO_3$ UV-Vis spectra reflects the Fe-O bond excitation (47, 115) and is similar to Fe_2O_3 (47). This attributes to the electronic transition of O_2p from the valence band to Fe-3d conduction band (116). Most literature reports DRS-UV-Vis spectra of $LaFeO_3$ ending at 700 nm, thus, they did not observe the extra band at 720nm as reported here. $LaCrO_3$ adsorbs till 380nm. It exhibits small absorption bands at 460nm and at 600nm. A theory study of $LaCrO_3$ electronic band structures (117) points out that $LaCrO_3$ conduction band consisted of Cr3d unoccupied orbitals and its valence band consisted of Cr3d partial occupied orbitals and O2p orbitals. Therefore, 2 small bands at around 650nm and 400nm represent Cr d-d transition and partial occupied Cr3d -O2p transition. The true bandgap is recognized as the cation-anion charge transfer (CT). In this case, it is the unoccupied Cr3d-O2p transition at 380nm. These small absorption bands at 460 and 650nm are similarly observed in Cr_2O_3 oxide (118) revealing the influent of Cr-O bonds in the $LaCrO_3$ perovskite electronic structure. Interestingly, the UVvis spectra of mixed perovskites (x = 0.25, 0.5, 0.75) display characters closer to $LaFeO_3$ than to $LaCrO_3$.

Figure 37b shows the optical bandgaps (Eg) of five synthesized peroviskites generated from the UV-vis spectra. The incident photon energy (E = hv) and the optical bandgap energy (E_g) are related to the transformed Kubelka − Munk function (F(R)) in the following equation $[F(R)\cdot hv]^n = A (hv - E_g)$, where A is the constant depending on transition probability and n = ½ or 2 for indirect or direct bandgaps, respectively(84, 85). For direct bandgap materials, which is the case of $LaCrO_3$ and $LaFeO_3$(117, 119), n = 2, and bandgap E_g is the interception of the slope with x-axis when plotting $[F(R)\cdot hv]^2$ as a function of E = hv.

$LaCrO_3$ and $LaFeO_3$ bandgaps are measured at 3.1 eV and 2.0 eV respectively, agreed with reported value (66, 113, 117). Generally, in oxide photocatalysts, the valance band (VB) is determined by O2p orbital and the conduction band (CB) is determined by metal ion electrical state. For example, in $LaFeO_3$, VB is O2p orbital, CB is Fe3d orbital, the bandgap is the electronic transition takes place from O2p to Fe3d. The band gap of LaFeO3 is 2.2eV, in agreement with literature(46). Three new perovskites interestingly all have bandgap similar to LaFeO3 (~2.0-2.1eV) regardless of the difference in percentage of Fe/Cr ratio (x) in the materials. Umezawa(120) recently published a work where lanthanum pervoskites bandgap changed significantly by the oxynitride percentage (x) upto 0.25%. At 25% (or x = 0.25), the bandgap alteration progress halted and its value is close to the bandgap at x = 1. The shift of the bandgaps versus Fe/Cr ratio is consistent with the transition of the material colors from green to red and deep red, revealing their light adsorption capability moving from UV to visible-light range.

Figure 38 is the Mott-Schottky plots for obtaining the conduction band potentials for five perovskites. The conduction bands measured at different frequencies are all reasonably agreed with each other, with a deviation of less than ±0.04 eV (<10%). This validated a valid measurement under Mott-Schottky assumption.

The bandgap and flat-band potential measurement are summarized in Figure 38. Interestingly, the results differs from our expectations. The hypothesis was that the bandgap will reduce gradually from 3.2 eV to 2 eV as Fe ions replace Cr ions. Instead, the bandgap of $LaCr_{1-x}Fe_xO_3$ changes suddenly to ~2.eV even at only 25% Fe replacement. This bandgap value remains the same as the Fe ratio increases. Further theoretical studies of the $LaCr_{1-x}Fe_xO_3$ bandgap are going on within our group to further understand this observation at the molecular electronic level. The conduction band obtained from Mott-Schottky plots also show some unexpected nonlinear behavior.. Umezawa(120) et al. ‘s work on simulation of bandedge and bandgap for pervoskites showed that when introducing new metals in the structure, it cohesively changes the band alignments of conduction and valence bands. These changes is not reflected in the Density of States (DOS) of stand-alone individual substituted atoms but by how it interacts within the structures. Similarly, at x = 0.75, $LaCr_{0.25}Fe_{0.75}O_3$ could potentially ee a shift in conduction band potential position, different from the rest of the perovskites. Future simulation studies will address this experimental finding. Lowering symmetry of the crystal structure by introducing foreign elements are also known to shift conduction band minimum upward in pervoskite(120) which is beneficial for CO_2 reduction.

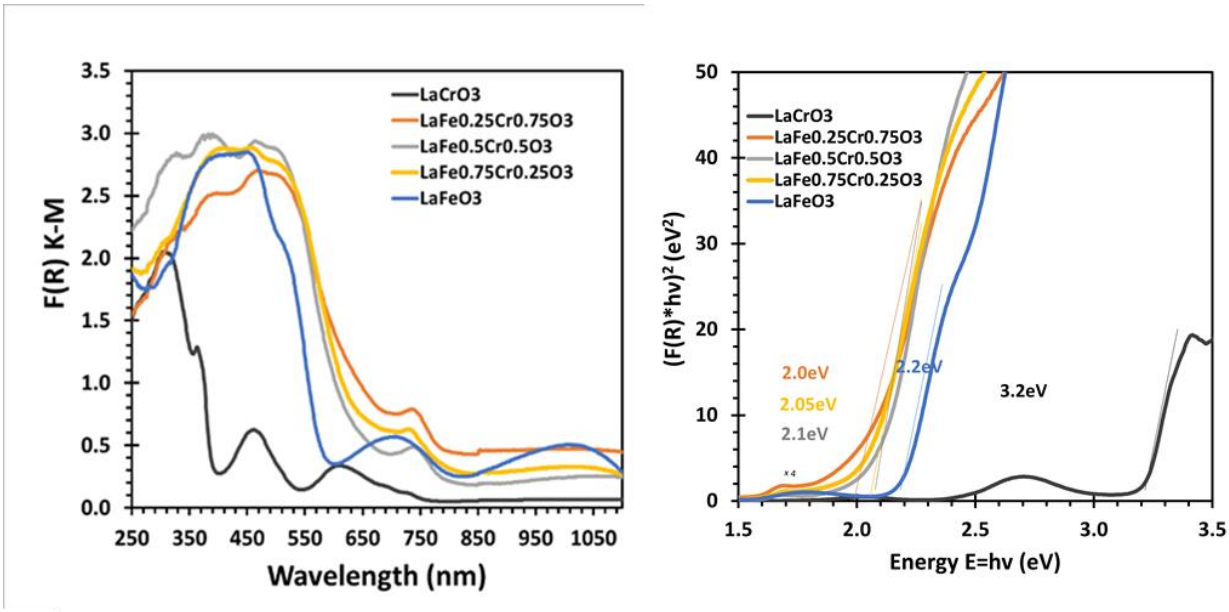

Figure 37: DRS-UVvis measurement of $LaCr_{1-x}Fe_xO_3$. a) UV-vis solidstate absorption spectra of five pervoskites. b) Tauc plot to determine their optical bandgaps

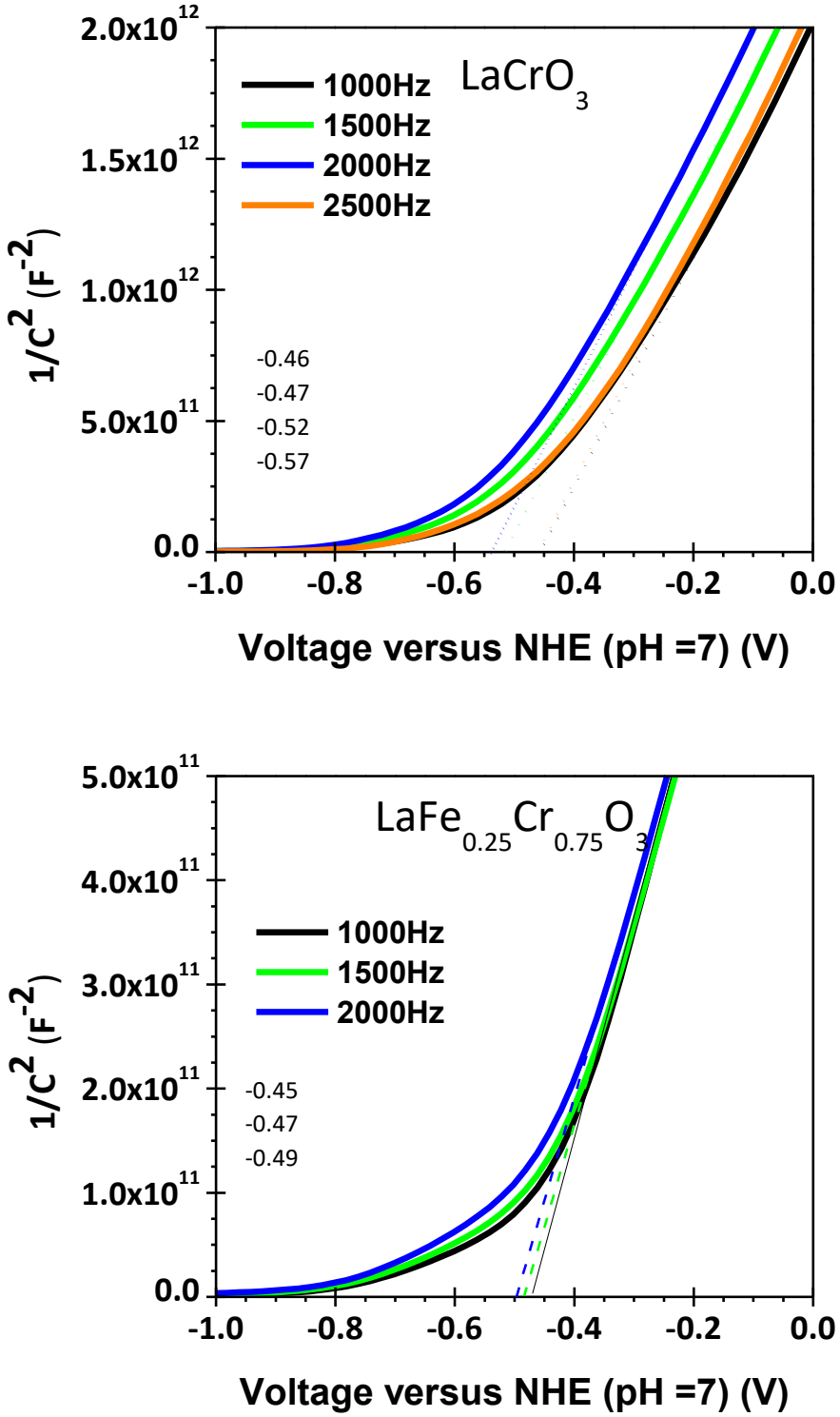

Figure 38: The Mott-Schottky plots for obtaining the conduction band potentials for five perovskites

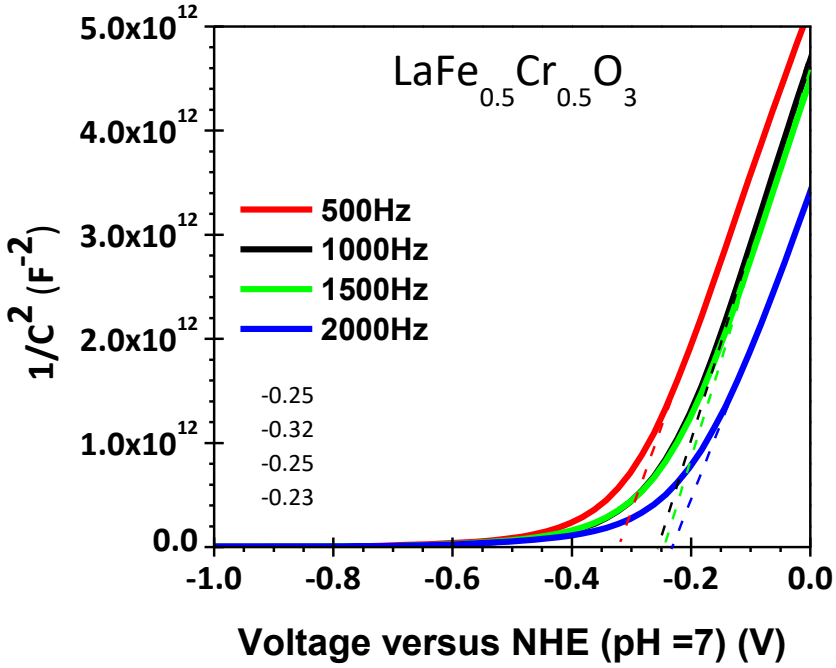

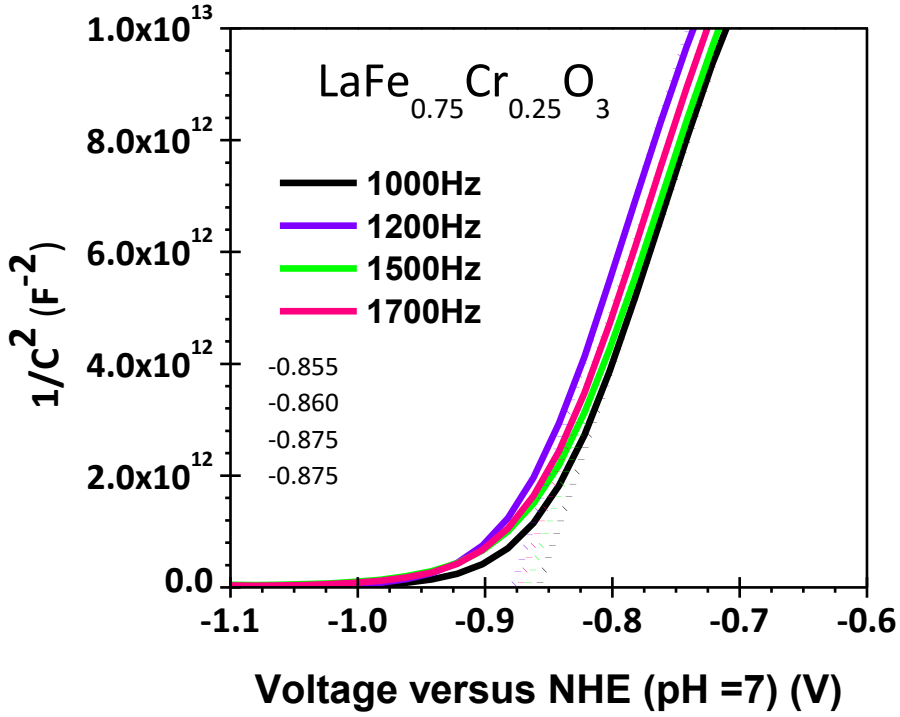

Figure 38 (continued)

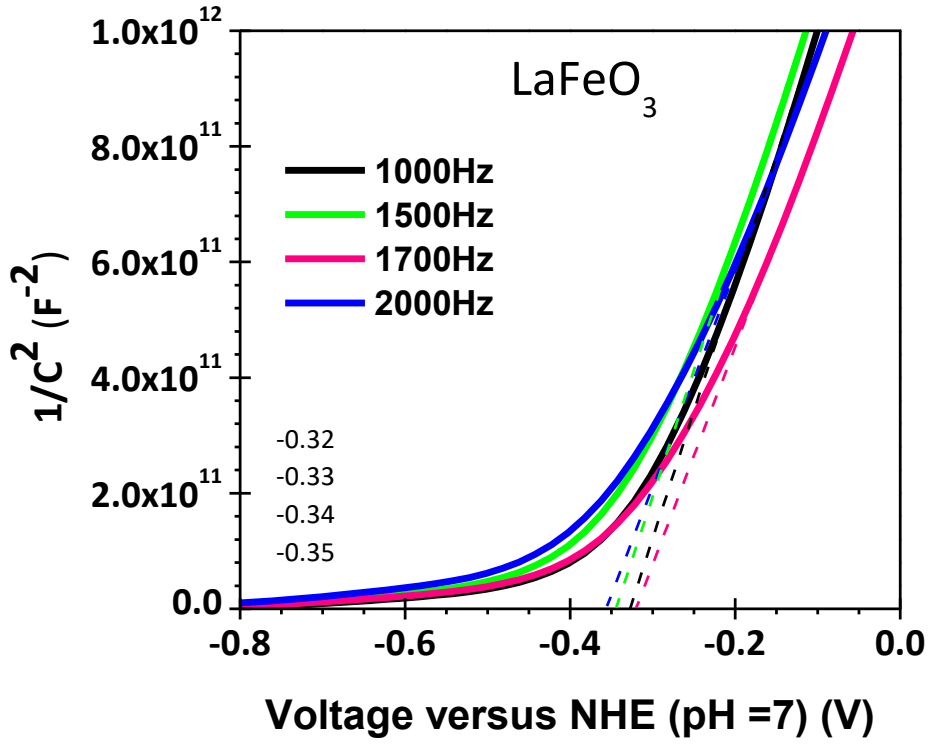

Figure 38 (continued)

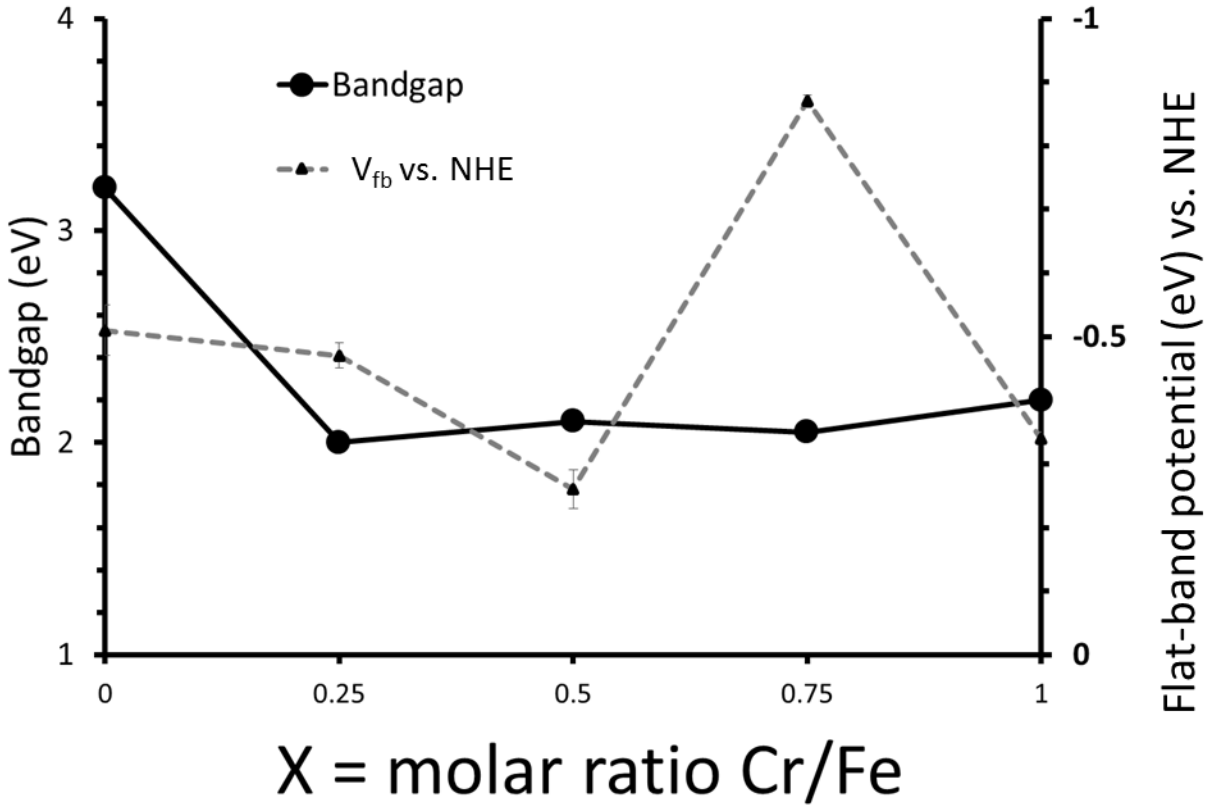

Figure 39: Summary of perovskites bandgaps and flat-band potential results

5.3.3 CO_2 Photoreactivity

The photoactvity of pervoskites are then tested for CO_2 reduction in presence of H_2O to make CH_4 and CO under visible light (λ >400nm). The CO_2 reduction with H_2O follows two half reactions: the oxidation of water and the reduction of CO_2(5, 21): $LaCr_xFe_{1-x}O_3 \rightarrow e^- + h^+$, $2H_2O + 4h+ \rightarrow O_2 + 4H^+$, $CO_2 + 2H^+ + 2e^- \rightarrow CO + H_2O$, $CO_2 + 8H^+ + 8e^- \rightarrow CH_4 + 2H_2O$. Controlled reaction experiment were carried out to validate the source of C to form CH_4 and CO from CO_2 rather than from the catalysts or other contamination sources. Figure 39 shows the products (CH_4, CO and O_2) observed after 4 hours of visible light illumination normalized for the weight of perovskites used. H_2 was undetectable or in a negligible amount in compared to three main products above. Longer hydrocarbon compounds such as C_2H_4, C_2H_6 while were reported in other photocatalytic studies(121) were not observed in this work. This is because these photocatalytic studies loaded an amount of ~5% Pt on the studied catalysts which usually significantly increase the production yield and the variation of eluted products. Among five studied perovskites, $LaCr_{0.25}Fe_{0.75}O_3$ (x = 0.75) is the most active photocatalyst and $LaCr_{0.75}Fe_{0.25}O_3$ (x = 0.25) is 2nd best whereas the rest of the La perovskites show a minimal photocatalytic reactivity. The quantum efficiency was calculated using the following equation.

$$\eta_{CO \text{ or } CH_4}(\%) = \frac{n * \text{moles of reduction products (CO or } CH_4)}{\text{moles of photon incident on catalyst}} * 100\%$$

This is consistent with previous reports that a long induction period is required as Cr6+ species will consume photo-generated electrons and hydrogen evolution is a competitive process with reduction of Cr6+ species (51)

The reactivity of synthesized pervoskites are perfectly explained by Figure 39 where the bandgap and bandedges are graphed against NHE or vacuum potentials and in perspective of CO_2-H_2O redox reaction potentials. $LaCrO_3$ has largest bandgap (Eg = 3.20 eV), therefore it does not absorb visible light and do not generate excited enough e^-/h^+ pairs to catalyze the reaction. The conduction band potentials were calculated using the following equation: $E_{CB} = E_{redox} + V_{fb}$ where the E_{redox} is the redox potential of electrolyte in the Mott-Schottky measurement. The electrolyte is 0.1M Na_2SO_4 solution. Because the E_{redox} of Na_2SO4 is larger than water splitting(122), at the working electrode (or the cathode where the photocatalyst is), water is reduced instead of Na^+. Therefore, E_{redox} used in the above equation is $E_{redox} = E_{H+/H2} = 0$ eV vs. NHE.

The conduction band potentials of $LaCr_{0.5}Fe_{0.5}O_3$ and $LaFeO_3$ (x = 0.5 and 1) are not negative enough for CO_2 conversion, thus they are inactive for CO_2 photoreduction. $LaCr_{0.25}Fe_{0.75}O_3$ (x = 0.75) has a small bandgap (Eg = 2.0 eV) to absorb photon at wavelength 400nm-620nm and its bandedges are thermodynamically favorable for the redox reaction. Therefore, it has the best photoreactivity out of five samples. This agrees with other studies which also confirm that the photocatlyst reactivity under visible light were dictated by their small bandgaps and suitable band edges.

5.4 Conclusion

When replacing Cr ions at the B sites of $LaCrO_3$ perovskites by Fe ions, the bandgap does not follow a linear trend in regards to the metal ratio composition. Bandedges were successfully measured for the new synthesized materials. At x = 0.25, the conduction band potential remains similar with x = 0. However, at x = 0.75, the conduction band potential was more negative than either perovskites at x = 0 or x = 1.

Future simulation of the density of states could address this interesting observation. CO_2 reduction relativities of each perovskites were predicted accurately by their measured bandgaps and bandedges. Among the five studied perovskites, synthesized $LaCr_{0.25}Fe_{0.75}O_3$ (x = 0.75) was the most active for CO_2 photoreduction under visible illumination at room temperature thanks to its small bandgap (2.0 eV) and its suitable bandedges for CO_2 photoreduction.

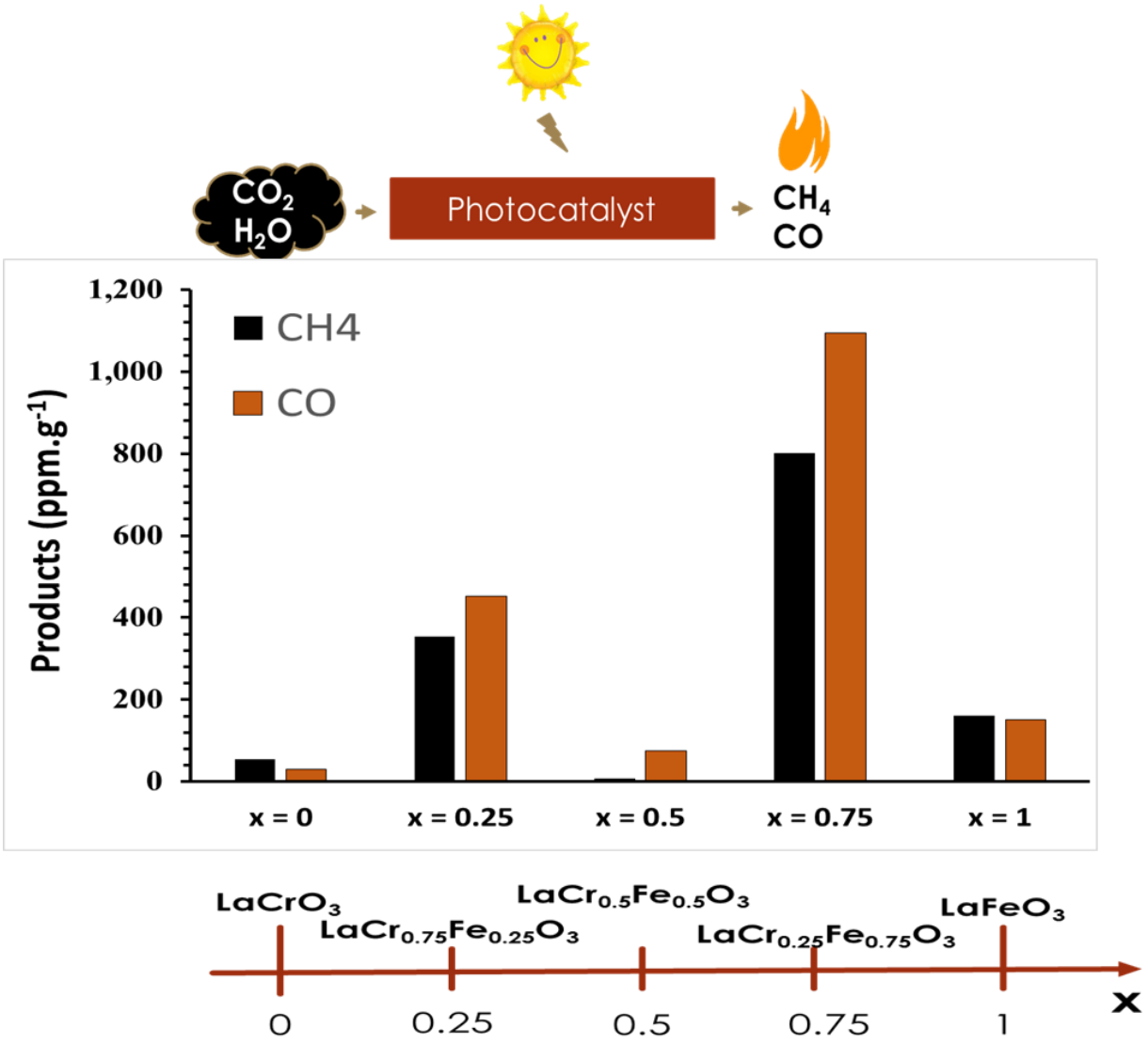

Figure 40: CO_2 photoreduction products of $LaCr_{1-x}Fe_xO_3$ after 4 hours illuminated by visible-light-cut-off solar simulator (λ>400nm)

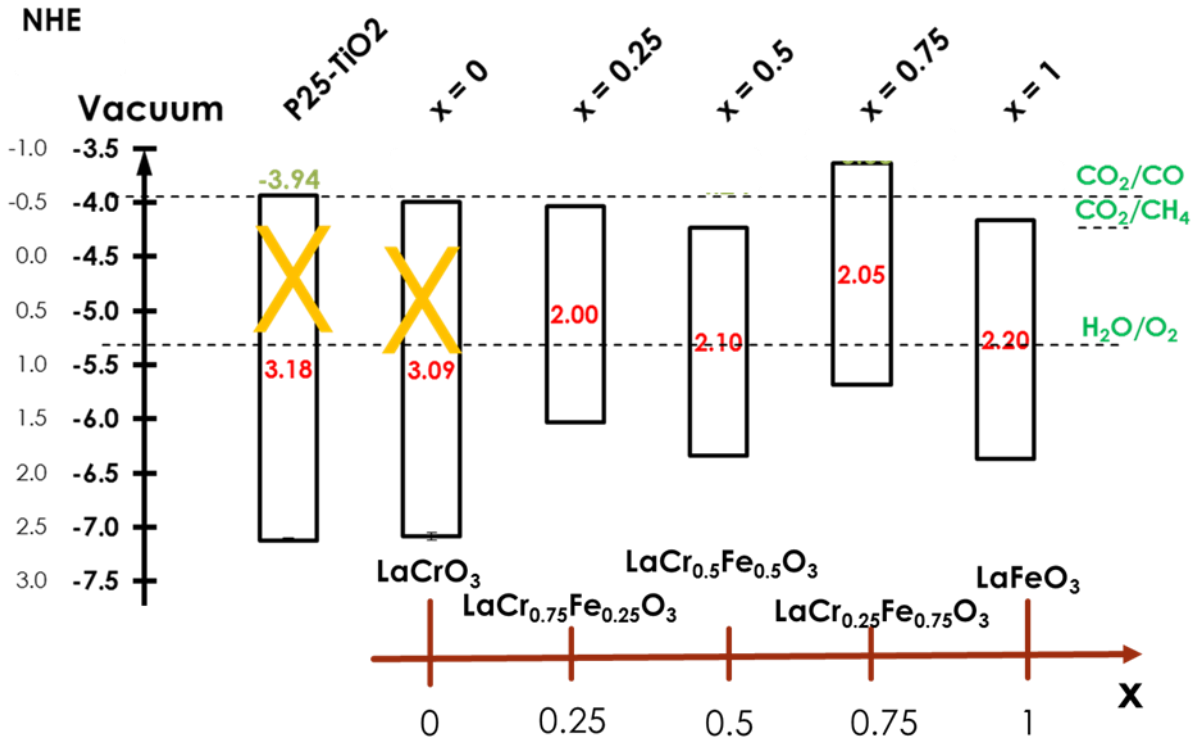

Figure 41: Overall summary of perovskites photocatalytic properties in regards to CO_2 H_2O redox reaction. The conduction bands were calculated using the equation $E_{CB} = E_{redox} + V_{fb}$

CHAPTER 6: CONCLUSION AND FUTURE WORK

6.1 Conclusion

Two tunable materials, MOFs and perovskites were investigated for their photocatalytic CO_2 reduction. Both candidates were able to achieve the narrow bandgaps needed for visible light harvesting. Two compounds, Ti/Zr-MOF-525 and $LaCr_{0.25}Fe_{0.75}O_3$ were found to have suitable conduction band potential to drive the CO_2 reduction to CH_4.

Ti/Zr-MOF-525 was demonstrated to reduce CO_2 in H_2O to gaseous chemical fuels (CH_4 and CO) without the presence of any sacrificial agents and using only visible light. Results show the tunability of MOF by using suitable linkers and metals in secondary-building-units in order to obtain desired bandgap and band edges for effective photocatalytic reactions. Though the yield is limited, the reaction produces selectively toward CH_4 versus CO and no sacrificial reagents are required.

The bandgap of $LaCr_{1-x}Fe_xO_3$was tuned from 3.2eV to 2.0eV when substituting Cr by Fe metal. The bandgap was narrowed down even at the smallest substitution (25%) level. Among the five studied perovskites, synthesized $LaCr_{0.25}Fe_{0.75}O_3$ (x = 0.75) was the most active for CO_2 photoreduction under visible illumination at room temperature because of its small bandgap (2.0 eV) and its suitable bandedges for CO_2 photoreduction.

This work validates that a small bandgap and suitable bandedges are the main criteria for photocatalytic reaction to occur under visible-light illumination.

However, even after satisfying these criteria, the production yield and the quantum efficiencies remain modest (in range of 0.01% quantum efficiency). Therefore, other obstacles such as limiting the recombination process, increasing the photocatalytic stability, and improving the surface area remain for additional investigation.

6.2 Future Work

Several directions for future work are listed below. Besides a proposed detailed study of the catalytic reactivity of these photocatalysts to understand the mechanism of the photocatalytic reaction, this future work section also suggests a theoretical approach to study photocatalytic activity.

6.2.1 A Theoretical Study of Perovskites Bandgap and Bandedges

The findings of the five synthesized perovskites are interesting. A theoretical study using DFT or DFT-U would offer an explanation into the molecular level of the bandgap and bandedge behavior when substituting metals in site B. This could provide a tool for designing better photocatalysts for with targeted bandgap and band edges.

6.2.2 Increase Surface Area for Perovskites

Studied perovskites were synthesized at 950^{o}C to generate high crystallinity but they had low surface area (<5m^{2}/g). High crystallinity decreases charge recombination within the photocatalysts; however, low surface area reduces the reactant adsorption,

thus lowering the catalytic reactivity. Therefore, perovskites with higher surface area would likely increase the reactivity. To increase the surface area, several methods can be utilized. One is to synthesize at a lower temperature (`600-750^{o}C). At lower synthesized temperature, perovskites can potentially increase surface area from ~5m^2/g to 50m^2/g. Another method that has been reported is to high-energy ball milling the perovskite.

REFERENCES

1. Yu JC, Yu J, Ho W, Jiang Z, Zhang L. Effects of F-doping on the photocatalytic activity and microstructures of nanocrystalline TiO2 powders. Chemistry of materials. 2002;14(9):3808-16.

2. Kato H, Kudo A. Visible-light-response and photocatalytic activities of TiO2 and SrTiO3 photocatalysts codoped with antimony and chromium. The Journal of Physical Chemistry B. 2002;106(19):5029-34.

3. Liu L, Zhao H, Andino JM, Li Y. Photocatalytic CO2 reduction with H2O on TiO2 nanocrystals: Comparison of anatase, rutile, and brookite polymorphs and exploration of surface chemistry. Acs Catalysis. 2012;2(8):1817-28.

4. Fujishima A, Honda K. Electrochemical Photolysis of Water at a Semiconductor Electrode. Nature. 1972;238(5358):37-+.

5. Inoue T, Fujishima A, Konishi S, Honda K. Photoelectrocatalytic reduction of carbon dioxide in aqueous suspensions of semiconductor powders. Nature. 1979;277:637-8.

6. Reece SY, Hamel JA, Sung K, Jarvi TD, Esswein AJ, Pijpers JJ, et al. Wireless solar water splitting using silicon-based semiconductors and earth-abundant catalysts. Science. 2011;334(6056):645-8.

7. Maeda K, Teramura K, Domen K. Effect of post-calcination on photocatalytic activity of (Ga1-xZnx)(N1-xOx) solid solution for overall water splitting under visible light. Journal of catalysis. 2008;254(2):198-204.

8. Lewis NS, Crabtree G. Basic research needs for solar energy utilization: report of the basic energy sciences workshop on solar energy utilization, April 18-21, 2005. 2005.

9. Crabtree GW, Lewis NS. Solar energy conversion. Physics today. 2008:309-21.

10. Planck M. On the law of distribution of energy in the normal spectrum. Annalen der Physik. 1901;4(553):1.

11. Asahi R, Morikawa T, Ohwaki T, Aoki K, Taga Y. Visible-light photocatalysis in nitrogen-doped titanium oxides. science. 2001;293(5528):269-71.

12. Kato H, Asakura K, Kudo A. Highly efficient water splitting into H2 and O2 over lanthanum-doped NaTaO3 photocatalysts with high crystallinity and surface nanostructure. Journal of the American Chemical Society. 2003;125(10):3082-9.

13. Ohno T, Akiyoshi M, Umebayashi T, Asai K, Mitsui T, Matsumura M. Preparation of S-doped TiO< sub> 2</sub> photocatalysts and their photocatalytic activities under visible light. Applied Catalysis A: General. 2004;265(1):115-21.

14. Kato H, Hori M, Konta R, Shimodaira Y, Kudo A. Construction of Z-scheme type heterogeneous photocatalysis systems for water splitting into H2 and O2 under visible light irradiation. Chemistry Letters. 2004;33(10):1348-9.

15. Zhu H, Yang B, Xu J, Fu Z, Wen M, Guo T, et al. Construction of Z-scheme type CdS–Au–TiO< sub> 2</sub> hollow nanorod arrays with enhanced photocatalytic activity. Applied Catalysis B: Environmental. 2009;90(3):463-9.

16. Wang X, Li S, Ma Y, Yu H, Yu J. H2WO4· H2O/Ag/AgCl composite nanoplates: a plasmonic Z-scheme visible-light photocatalyst. The Journal of Physical Chemistry C. 2011;115(30):14648-55.

17. Sasaki Y, Iwase A, Kato H, Kudo A. The effect of co-catalyst for Z-scheme photocatalysis systems with an Fe< sup> 3+</sup>/Fe< sup> 2+</sup> electron mediator on overall water splitting under visible light irradiation. Journal of Catalysis. 2008;259(1):133-7.

18. Szczepankiewicz SH, Moss JA, Hoffmann MR. Electron traps and the stark effect on hydroxylated titania photocatalysts. The Journal of Physical Chemistry B. 2002;106(31):7654-8.

19. Fox MA, Dulay MT. Heterogeneous photocatalysis. Chemical reviews. 1993;93(1):341-57.

20. Arai T, Yanagida M, Konishi Y, Iwasaki Y, Sugihara H, Sayama K. Promotion effect of CuO co-catalyst on WO< sub> 3</sub>-catalyzed photodegradation of organic substances. Catalysis Communications. 2008;9(6):1254-8.

21. Indrakanti VP, Kubicki JD, Schobert HH. Photoinduced activation of CO 2 on Ti-based heterogeneous catalysts: Current state, chemical physics-based insights and outlook. Energy & Environmental Science. 2009;2(7):745-58.

22. Kumar B, Llorente M, Froehlich J, Dang T, Sathrum A, Kubiak CP. Photochemical and photoelectrochemical reduction of CO2. Annual Review of Physical Chemistry. 2012;63:541-69.

23. Mueller U, Schubert M, Teich F, Puetter H, Schierle-Arndt K, Pastre J. Metal–organic frameworks—prospective industrial applications. Journal of Materials Chemistry. 2006;16(7):626-36.

24. Lee J, Farha OK, Roberts J, Scheidt KA, Nguyen ST, Hupp JT. Metal–organic framework materials as catalysts. Chemical Society Reviews. 2009;38(5):1450-9.

25. Horcajada P, Chalati T, Serre C, Gillet B, Sebrie C, Baati T, et al. Porous metal-organic-framework nanoscale carriers as a potential platform for drug delivery and imaging. Nature materials. 2010;9(2):172-8.

26. Laurier KG, Vermoortele F, Ameloot R, De Vos DE, Hofkens J, Roeffaers MB. Iron (III)-Based Metal–Organic Frameworks As Visible Light Photocatalysts. J Am Chem Soc. 2013;135(39):14488-91.

27. Morris W, Volosskiy B, Demir S, Gándara F, McGrier PL, Furukawa H, et al. Synthesis, Structure, and Metalation of Two New Highly Porous Zirconium Metal–Organic Frameworks. Inorganic chemistry. 2012;51(12):6443-5.

28. Alvaro M, Carbonell E, Ferrer B, Llabrés i Xamena FX, Garcia H. Semiconductor Behavior of a Metal-Organic Framework (MOF). Chemistry-A European Journal. 2007;13(18):5106-12.

29. Tachikawa T, Choi JR, Fujitsuka M, Majima T. Photoinduced Charge-Transfer Processes on MOF-5 Nanoparticles: Elucidating Differences between Metal-Organic Frameworks and Semiconductor Metal Oxides. The Journal of Physical Chemistry C. 2008;112(36):14090-101.

30. Silva CG, Corma A, García H. Metal–organic frameworks as semiconductors. Journal of Materials Chemistry. 2010;20(16):3141-56.

31. Lin C-K, Zhao D, Gao W-Y, Yang Z, Ye J, Xu T, et al. Tunability of Band Gaps in Metal–Organic Frameworks. Inorganic chemistry. 2012;51(16):9039-44.

32. Llabrés i Xamena FX, Corma A, Garcia H. Applications for metal-organic frameworks (MOFs) as quantum dot semiconductors. The Journal of Physical Chemistry C. 2007;111(1):80-5.

33. HoonáChoi J, JeongáChoi Y, WooáLee J, HoáShin W, KuáKang J. Tunability of electronic band gaps from semiconducting to metallic states via tailoring Zn ions in MOFs with Co ions. Physical Chemistry Chemical Physics. 2009;11(4):628-31.

34. Bordiga S, Lamberti C, Ricchiardi G, Regli L, Bonino F, Damin A, et al. Electronic and vibrational properties of a MOF-5 metal–organic framework: ZnO quantum dot behaviour. Chem Commun. 2004(20):2300-1.

35. Fu Y, Sun D, Chen Y, Huang R, Ding Z, Fu X, et al. An Amine-Functionalized Titanium Metal–Organic Framework Photocatalyst with Visible-Light-Induced Activity for CO2 Reduction. Angewandte Chemie. 2012;124(14):3420-3.

36. Wang J-L, Wang C, Lin W. Metal–organic frameworks for light harvesting and photocatalysis. Acs Catalysis. 2012;2(12):2630-40.

37. De Lima R, Batista M, Wallau M, Sanches E, Mascarenhas YP, Urquieta-Gonzalez E. High specific surface area LaFeCo perovskites—Synthesis by nanocasting and catalytic behavior in the reduction of NO with CO. Applied Catalysis B: Environmental. 2009;90(3):441-50.

38. Ishihara T. Perovskite oxide for solid oxide fuel cells: Springer Science & Business Media; 2009.

39. Pena M, Fierro J. Chemical structures and performance of perovskite oxides. Chemical reviews. 2001;101(7):1981-2018.

40. Huang K, Lee HY, Goodenough JB. Sr-and Ni-Doped LaCoO3 and LaFeO3 Perovskites New Cathode Materials for Solid-Oxide Fuel Cells. Journal of the Electrochemical Society. 1998;145(9):3220-7.

41. Ferri D, Forni L, Dekkers MA, Nieuwenhuys BE. NO reduction by H 2 over perovskite-like mixed oxides. Applied Catalysis B: Environmental. 1998;16(4):339-45.

42. Luo J, Im J-H, Mayer MT, Schreier M, Nazeeruddin MK, Park N-G, et al. Water photolysis at 12.3% efficiency via perovskite photovoltaics and Earth-abundant catalysts. Science. 2014;345(6204):1593-6.

43. Kim HG, Hwang DW, Bae SW, Jung JH, Lee JS. Photocatalytic water splitting over La2Ti2O7 synthesized by the polymerizable complex method. Catalysis letters. 2003;91(3-4):193-8.

44. Wang Z, Teramura K, Hosokawa S, Tanaka T. Photocatalytic conversion of CO 2 in water over Ag-modified La 2 Ti 2 O 7. Applied Catalysis B: Environmental. 2015;163:241-7.

45. Tejuca LG, Fierro JLG. XPS and TPD probe techniques for the study of LaNiO3 perovskite oxide. Thermochimica Acta. 1989;147(2):361-75.

46. Parida K, Reddy K, Martha S, Das D, Biswal N. Fabrication of nanocrystalline LaFeO 3: an efficient sol–gel auto-combustion assisted visible light responsive photocatalyst for water decomposition. International journal of hydrogen energy. 2010;35(22):12161-8.

47. Li S, Jing L, Fu W, Yang L, Xin B, Fu H. Photoinduced charge property of nanosized perovskite-type LaFeO 3 and its relationships with photocatalytic activity under visible irradiation. Materials Research Bulletin. 2007;42(2):203-12.

48. Yang J, Hu R, Meng W, Du Y. A novel p-LaFeO 3/n-Ag 3 PO 4 heterojunction photocatalyst for phenol degradation under visible light irradiation. Chemical Communications. 2016;52(12):2620-3.

49. Ren X, Yang H, Gen S, Zhou J, Yang T, Zhang X, et al. Controlled growth of LaFeO 3 nanoparticles on reduced graphene oxide for highly efficient photocatalysis. Nanoscale. 2016;8(2):752-6.

50. Ishii T, Kato H, Kudo A. H 2 evolution from an aqueous methanol solution on SrTiO 3 photocatalysts codoped with chromium and tantalum ions under visible light irradiation. Journal of Photochemistry and Photobiology A: Chemistry. 2004;163(1):181-6.

51. Xu X, Lv M, Sun X, Liu G. Role of surface composition upon the photocatalytic hydrogen production of Cr-doped and La/Cr-codoped SrTiO3. Journal of Materials Science. 2016;51(13):6464-73.

52. Zhu J, Zhang Y, Basu A, Lu Z, Paranthaman M, Lee D, et al. LaCrO 3-based coatings on ferritic stainless steel for solid oxide fuel cell interconnect applications. Surface and Coatings Technology. 2004;177:65-72.

53. Tao S, Irvine JT. A redox-stable efficient anode for solid-oxide fuel cells. Nature materials. 2003;2(5):320-3.

54. Jiang SP, Liu L, Ong KP, Wu P, Li J, Pu J. Electrical conductivity and performance of doped LaCrO 3 perovskite oxides for solid oxide fuel cells. Journal of Power Sources. 2008;176(1):82-9.

55. Hod I, Sampson MD, Deria P, Kubiak CP, Farha OK, Hupp JT. Fe-porphyrin-based metal–organic framework films as high-surface concentration, heterogeneous catalysts for electrochemical reduction of CO2. ACS Catalysis. 2015;5(11):6302-9.

56. Fateeva A, Chater PA, Ireland CP, Tahir AA, Khimyak YZ, Wiper PV, et al. A Water-Stable Porphyrin-Based Metal–Organic Framework Active for Visible-Light Photocatalysis. Angewandte Chemie. 2012;124(30):7558-62.

57. Horiuchi Y, Toyao T, Saito M, Mochizuki K, Iwata M, Higashimura H, et al. Visible-light-promoted photocatalytic hydrogen production by using an amino-functionalized Ti (IV) metal–organic framework. The Journal of Physical Chemistry C. 2012;116(39):20848-53.

58. de Miguel M, Ragon F, Devic T, Serre C, Horcajada P, García H. Evidence of Photoinduced Charge Separation in the Metal–Organic Framework MIL-125 (Ti)-NH2. ChemPhysChem. 2012;13(16):3651-4.

59. Toyao T, Saito M, Horiuchi Y, Mochizuki K, Iwata M, Higashimura H, et al. Efficient hydrogen production and photocatalytic reduction of nitrobenzene over a visible-light-responsive metal–organic framework photocatalyst. Catalysis Science & Technology. 2013;3(8):2092-7.

60. Zhang T, Lin W. Metal–organic frameworks for artificial photosynthesis and photocatalysis. Chemical Society Reviews. 2014;43(16):5982-93.

61. Nasalevich M, Van der Veen M, Kapteijn F, Gascon J. Metal–organic frameworks as heterogeneous photocatalysts: advantages and challenges. CrystEngComm. 2014;16(23):4919-26.

62. Lee Y, Kim S, Kang JK, Cohen SM. Photocatalytic CO 2 reduction by a mixed metal (Zr/Ti), mixed ligand metal–organic framework under visible light irradiation. Chemical Communications. 2015;51(26):5735-8.

63. Ivanova S, Senyshyn A, Zhecheva E, Tenchev K, Nikolov V, Stoyanova R, et al. Effect of the synthesis route on the microstructure and the reducibility of LaCoO 3. Journal of Alloys and Compounds. 2009;480(2):279-85.

64. Cava R, Batlogg B, Van Dover R, Murphy D, Sunshine S, Siegrist T, et al. Bulk superconductivity at 91 K in single-phase oxygen-deficient perovskite Ba 2 YCu 3 O 9− δ. Physical Review Letters. 1987;58(16):1676.

65. Popa M, Kakihana M. Synthesis of lanthanum cobaltite (LaCoO 3) by the polymerizable complex route. Solid State Ionics. 2002;151(1):251-7.

66. Suresh D. An Investigation on the Band Gap and Band Edge of Semi-Conducting Lanthanum Transition Metal Perovskites for Photocatalytic Applications. 2015.

67. Daza YA, Maiti D, Kent RA, Bhethanabotla VR, Kuhn JN. Isothermal reverse water gas shift chemical looping on La 0.75 Sr 0.25 Co (1− Y) Fe Y O 3 perovskite-type oxides. Catalysis Today. 2015;258:691-8.

68. Allen T. Particle size measurement: Springer; 2013.

69. Brunauer S, Emmett PH, Teller E. Adsorption of Gases in Multimolecular Layers. Journal of the American Chemical Society. 1938;60(2):309-19.

70. von Laue M. Concerning the detection of X-ray interferences. Nobel lecture. 1915:13.

71. Klug HP, Alexander LE. X-ray diffraction procedures: Wiley New York; 1954.

72. Waseda Y, Matsubara E, Shinoda K. X-ray diffraction crystallography: introduction, examples and solved problems: Springer Science & Business Media; 2011.

73. Goldstein J, Newbury DE, Echlin P, Joy DC, Romig Jr AD, Lyman CE, et al. Scanning electron microscopy and X-ray microanalysis: a text for biologists, materials scientists, and geologists: Springer Science & Business Media; 2012.

74. Hafner B. Energy Dispersive Spectroscopy on the SEM. Characterization Facility, University of Minnesota, USA. 2011.

75. Williams DB, Carter CB. The transmission electron microscope. Transmission electron microscopy: Springer; 1996. p. 3-17.

76. Thomas G, Goringe MJ. Transmission electron microscopy of materials. 1979.

77. Reimer L. Transmission electron microscopy: physics of image formation and microanalysis: Springer; 2013.

78. Rajeshwar K. Fundamentals of semiconductor electrochemistry and photoelectrochemistry. Encyclopedia of electrochemistry. 2007.

79. Gelderman K, Lee L, Donne S. Flat-band potential of a semiconductor: using the Mott–Schottky equation. J Chem Educ. 2007;84(4):685.

80. Yaghoubi H, Li Z, Chen Y, Ngo HT, Bhethanabotla VR, Joseph B, et al. Toward a Visible Light-Driven Photocatalyst: The Effect of Midgap-States-Induced Energy Gap of Undoped TiO2 Nanoparticles. ACS Catalysis. 2014;5(1):327-35.

81. Tu WG, Zhou Y, Zou ZG. Photocatalytic Conversion of CO2 into Renewable Hydrocarbon Fuels: State-of-the-Art Accomplishment, Challenges, and Prospects. Advanced Materials. 2014;26(27):4607-26.

82. Sun D, Fu Y, Liu W, Ye L, Wang D, Yang L, et al. Studies on Photocatalytic CO2 Reduction over NH2-Uio-66 (Zr) and Its Derivatives: Towards a Better Understanding of Photocatalysis on Metal–Organic Frameworks. Chemistry-A European Journal. 2013;19(42):14279-85.

83. Lin S, Diercks CS, Zhang Y-B, Kornienko N, Nichols EM, Zhao Y, et al. Covalent organic frameworks comprising cobalt porphyrins for catalytic CO2 reduction in water. Science. 2015;349(6253):1208-13.

84. Lin H, Huang C, Li W, Ni C, Shah SI, Tseng Y-H. Size dependency of nanocrystalline TiO 2 on its optical property and photocatalytic reactivity exemplified by 2-chlorophenol. Applied Catalysis B: Environmental. 2006;68(1):1-11.

85. Jentoft FC. Electronic Spectroscopy: Ultra Violet-Visible and Near IR Spectroscopies. Characterization of Solid Materials and Heterogeneous Catalysts: From Structure to Surface Reactivity, Volume 1&2. 2012:89-147.

86. Fang J, Wang F, Qian K, Bao H, Jiang Z, Huang W. Bifunctional N-doped mesoporous TiO2 photocatalysts. The Journal of Physical Chemistry C. 2008;112(46):18150-6.

87. Sakthivel S, Janczarek M, Kisch H. Visible light activity and photoelectrochemical properties of nitrogen-doped TiO2. The Journal of Physical Chemistry B. 2004;108(50):19384-7.

88. Gascon J, Hernández-Alonso MD, Almeida AR, Van Klink GP, Kapteijn F, Mul G. Isoreticular MOFs as efficient photocatalysts with tunable band gap: an operando FTIR study of the photoinduced oxidation of propylene. ChemSusChem. 2008;1(12):981-3.

89. Beranek R, Kisch H. Tuning the optical and photoelectrochemical properties of surface-modified TiO 2. Photochemical & Photobiological Sciences. 2008;7(1):40-8.

90. Beranek R, Kisch H. Surface-modified anodic TiO< sub> 2</sub> films for visible light photocurrent response. Electrochemistry communications. 2007;9(4):761-6.

91. Grätzel M. Photoelectrochemical cells. Nature. 2001;414(6861):338-44.

92. Bakhshi S, Collins S, Ferekides C, Takshi A, editors. Department of Electrical Engineering, University of South Florida, Tampa, Florida 33620, USA. Photovoltaic Specialists Conference (PVSC), 2013 IEEE 39th; 2013: IEEE.

93. Beranek R. (Photo) electrochemical Methods for the Determination of the Band Edge Positions of TiO 2-Based Nanomaterials. Advances in Physical Chemistry. 2012;2011.

94. Wang W-N, An W-J, Ramalingam B, Mukherjee S, Niedzwiedzki DM, Gangopadhyay S, et al. Size and structure matter: enhanced CO2 photoreduction efficiency by size-resolved ultrafine Pt nanoparticles on TiO2 single crystals. J Am Chem Soc. 2012;134(27):11276-81.

95. Sales NFd, Mansur HS. Chemsensor of NO2 gas based on porphyrin of 5, 10, 15, 20-tetraphenylporphyrin LB films and LS films. Materials Research. 2008;11(4):477-82.

96. Marsh D, Mink L. Microscale synthesis and electronic absorption spectroscopy of tetraphenylporphyrin H2 (TPP) and metalloporphyrins ZnII (TPP) and NiII (TPP). Journal of chemical education. 1996;73(12):1188.

97. Sakthivel S, Hidalgo M, Bahnemann D, Geissen S-U, Murugesan V, Vogelpohl A. A fine route to tune the photocatalytic activity of TiO< sub> 2</sub>. Applied Catalysis B: Environmental. 2006;63(1):31-40.

98. Chai L, White R, Greiner M, Lu Z. Experimental demonstration of the universal energy level alignment rule at oxide/organic semiconductor interfaces. Physical Review B. 2014;89(3):035202.

99. Yang L-M, Ganz E, Svelle S, Tilset M. Computational exploration of newly synthesized zirconium metal–organic frameworks UiO-66,-67,-68 and analogues. Journal of Materials Chemistry C. 2014;2(34):7111-25.

100. Dimitrijevic NM, Vijayan BK, Poluektov OG, Rajh T, Gray KA, He H, et al. Role of water and carbonates in photocatalytic transformation of CO2 to CH4 on titania. J Am Chem Soc. 2011;133(11):3964-71.

101. Jin S, Son H-J, Farha OK, Wiederrecht GP, Hupp JT. Energy transfer from quantum dots to metal–organic frameworks for enhanced light harvesting. J Am Chem Soc. 2013;135(3):955-8.

102. Shi L, Wang T, Zhang H, Chang K, Meng X, Liu H, et al. An Amine-Functionalized Iron (III) Metal–Organic Framework as Efficient Visible-Light Photocatalyst for Cr (VI) Reduction. Advanced Science. 2015;2(3).

103. Yamamoto M, Wang L, Li F, Fukushima T, Tanaka K, Sun L, et al. Visible light-driven water oxidation using a covalently-linked molecular catalyst–sensitizer dyad assembled on a TiO 2 electrode. Chemical Science. 2016.

104. Lee K, Howe JD, Lin L-C, Smit B, Neaton JB. Small-Molecule Adsorption in Open-Site Metal–Organic Frameworks: A Systematic Density Functional Theory Study for Rational Design. Chemistry of Materials. 2015;27(3):668-78.

105. Nunes GG, Seisenbaeva GA, Kessler VG. Crystal Engineering of Nanomorphology for Complex Oxide Materials via Thermal Decomposition of Metal− Organic Frameworks. Case Study of Sodium Tantalate. Crystal Growth & Design. 2011;11(4):1238-43.

106. Lin Q, Wu T, Zheng S-T, Bu X, Feng P. A chiral tetragonal magnesium-carboxylate framework with nanotubular channels. Chemical Communications. 2011;47(43):11852-4.

107. Tan Y-X, He Y-P, Zhang J. Tuning MOF stability and porosity via adding rigid pillars. Inorganic chemistry. 2012;51(18):9649-54.

108. Arima T-h, Tokura Y. Optical Study of Electronic Structure in Perovskite-Type RM O3 (R= La, Y; M= Sc, Ti, V, Cr, Mn, Fe, Co, Ni, Cu). Journal of the Physical Society of Japan. 1995;64(7):2488-501.

109. Kumar M, Srikanth S, Ravikumar B, Alex T, Das SK. Synthesis of pure and Sr-doped LaGaO 3, LaFeO 3 and LaCoO 3 and Sr, Mg-doped LaGaO 3 for ITSOFC application using different wet chemical routes. Materials Chemistry and Physics. 2009;113(2):803-15.

110. Kato H, Kudo A. Photocatalytic water splitting into H 2 and O 2 over various tantalate photocatalysts. Catalysis Today. 2003;78(1):561-9.

111. Dogra R, Junqueira A, Saxena R, Carbonari A, Mestnik-Filho J, Moralles M. Hyperfine interaction measurements in LaCrO 3 and LaFeO 3 perovskites using perturbed angular correlation spectroscopy. Physical Review B. 2001;63(22):224104.

112. Liqiang J, Honggang F, Baiqi W, Dejun W, Baifu X, Shudan L, et al. Effects of Sn dopant on the photoinduced charge property and photocatalytic activity of TiO 2 nanoparticles. Applied Catalysis B: Environmental. 2006;62(3):282-91.

113. Su H, Jing L, Shi K, Yao C, Fu H. Synthesis of large surface area LaFeO3 nanoparticles by SBA-16 template method as high active visible photocatalysts. Journal of Nanoparticle Research. 2010;12(3):967-74.

114. Wu H, Hu R, Zhou T, Li C, Meng W, Yang J. A novel efficient boron-doped LaFeO 3 photocatalyst with large specific surface area for phenol degradation under simulated sunlight. CrystEngComm. 2015;17(20):3859-65.

115. Wang Y, Zhu J, Zhang L, Yang X, Lu L, Wang X. Preparation and characterization of perovskite LaFeO 3 nanocrystals. Materials Letters. 2006;60(13):1767-70.

116. Li K, Wang D, Wu F, Xie T, Li T. Surface electronic states and photovoltage gas-sensitive characters of nanocrystalline LaFeO 3. Materials chemistry and physics. 2000;64(3):269-72.

117. Shi J, Ye J, Zhou Z, Li M, Guo L. Hydrothermal Synthesis of Na0. 5La0. 5TiO3–LaCrO3 Solid-Solution Single-Crystal Nanocubes for Visible-Light-Driven Photocatalytic H2 Evolution. Chemistry–A European Journal. 2011;17(28):7858-67.

118. de Collongue B, Garbowski E, Primet M. Catalytic combustion of methane over bulk and supported LaCrO 3 perovskites. Journal of the Chemical Society, Faraday Transactions. 1991;87(15):2493-9.

119. Mizokawa T, Fujimori A. Electronic structure and orbital ordering in perovskite-type 3d transition-metal oxides studied by Hartree-Fock band-structure calculations. Physical Review B. 1996;54(8):5368.

120. Umezawa N, Janotti A. Controlling the Electronic Structures of Perovskite Oxynitrides and their Solid Solutions for Photocatalysis. ChemSusChem. 2016;9(9):1027-31.

121. Li P, Ouyang S, Xi G, Kako T, Ye J. The effects of crystal structure and electronic structure on photocatalytic H2 evolution and CO2 reduction over two phases of perovskite-structured NaNbO3. The Journal of Physical Chemistry C. 2012;116(14):7621-8.

122. Oldham K, Myland J, Bond A. Electrochemical science and technology: fundamentals and applications: John Wiley & Sons; 2011.

APPENDIX A: CO_2 PHOTOREDUCTION PRODUCT ANALYSIS

CO_2 photoreduction gaseous products in this study are mainly CO, CH_4 and O_2. No other longer chain hydrocarbons such as C_2H_6 or C_2H_4 were detected. CH_3OH and C_2H_5OH were not detected either. H_2 were not detected. CO and CH_4 amount were calibrated externally for both thermal conductivity detector (TCD) and mass spectrometry (MS). The figures below are the calibration line for CO and CH_4 by TCD and MS. The 80 µl of samples with different concentrations (ppm) were used for each calibration data point, which is consistent with injection volume of samples during the experiment

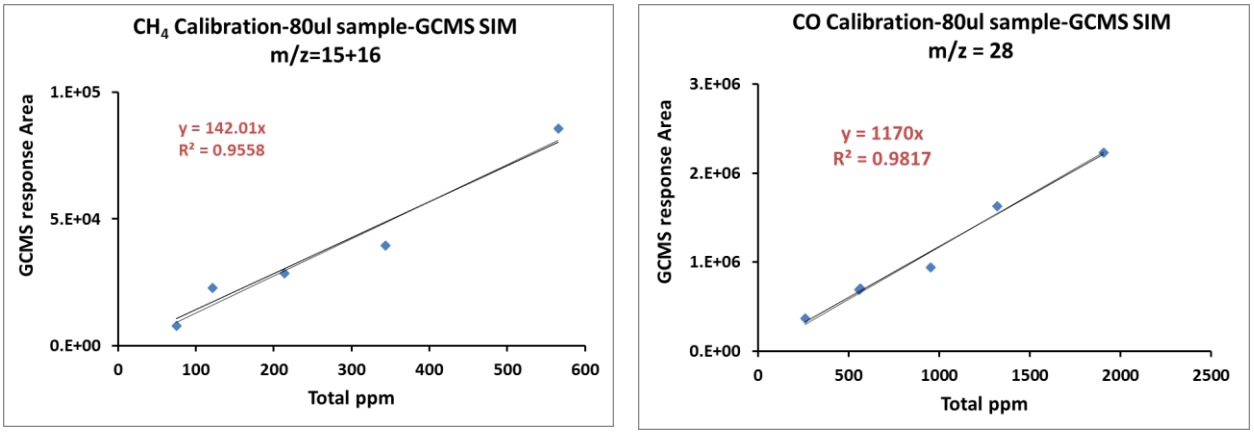

Figure A.1: Calibration line for CH_4 and CO concentration using gas chromatography-mass spectroscopy (selected ion method-SIM)

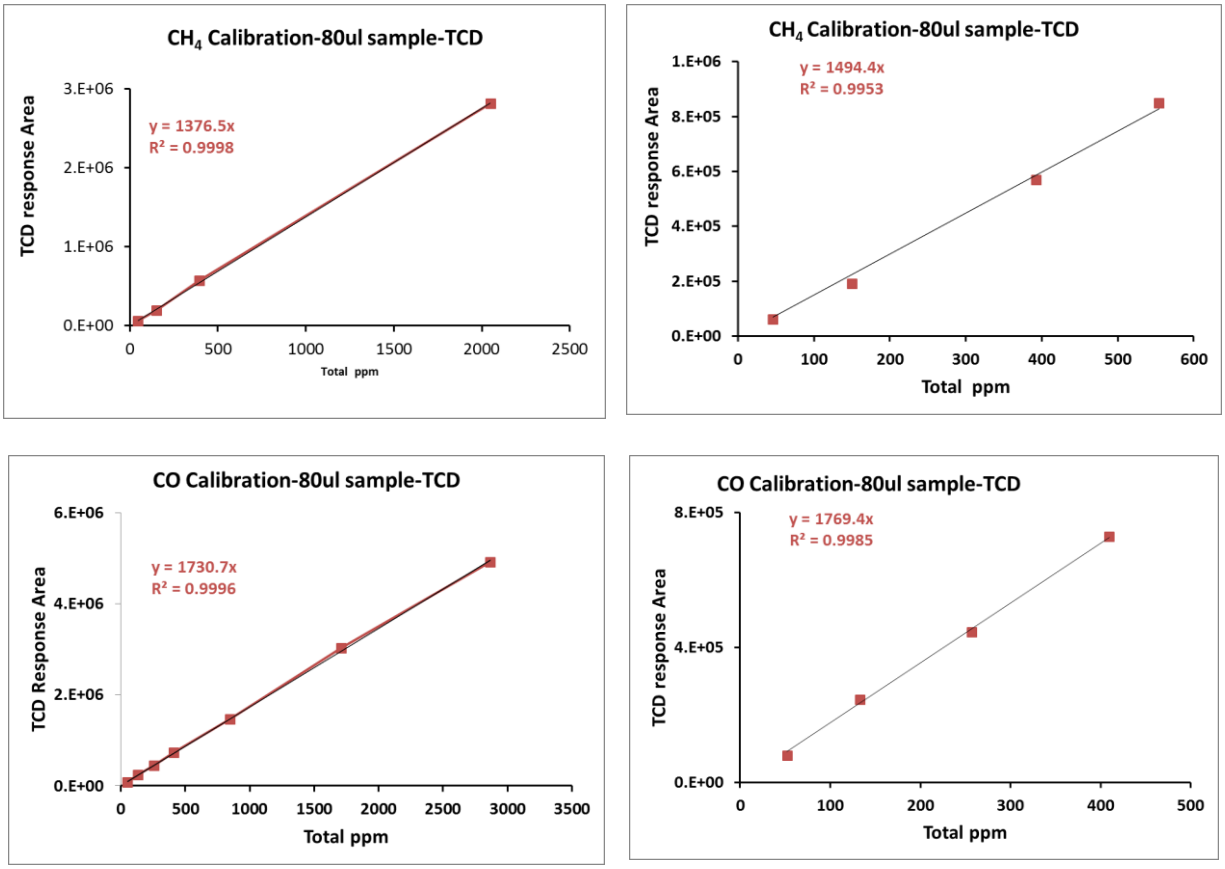

Figure A.2: Calibration line for CH_4 and CO concentration using TCD detector.

APPENDIX B: SUPPORTING CALCULATIONS

A.1 Conversion of ppm to µmol

The CO_2 photoreactor volume was measured by pipetting water into the reactor through the outlet valve until it filled up. The total reactor volume is 9905 µl or 9.9 ml in which 6432 µl is the body of the reactor where the catalyst sits and 3473 µl is the external volume from connection tubes, pressure gauge and valves. The concentration ppm (part per million volume) of products (CH_4 and CO) was converted to number of µmol applying ideal gas law nRT = PV. Under the reaction temperature and pressure (T= 40^{o}C, P = 20psi), CH_4 and CO satisfy the ideal gas behavior. Therefore, the conversion ppm to µmol uses the following equations

$$1\ \text{ppm}\ (\text{V}) = 10^{-6}$$

$$\text{n} = \frac{\text{PV}}{\text{RT}}$$

$$\mu\text{mol}_{\frac{CH_4}{CO}} = \frac{\left(20\text{psi} * \frac{6894.76\text{Pa}}{\text{psi}}\right) * \left(\mathbf{X}\ \text{ppm} * \frac{10^{-6}}{\text{ppm}} * 9905\mu\text{l} * \frac{1\text{m}^3}{10^9\mu\text{l}}\right)}{8.134\text{m}^3\text{PaK}^{-1}\text{mol}^{-1} * (40\text{oC} + 273.15\text{K})} * \frac{10^6\mu\text{mol}}{1\text{mol}}$$

$$= \left(5.3622\text{E} - 4\frac{\mu\text{mol}}{\text{ppm}}\right) * \mathbf{X}\ \text{ppm}$$

ABOUT THE AUTHOR

ThuHuong Ngo was born and raised in Hanoi, Vietnam. She earned her B.S in Chemical Engineering at the University of Tulsa and a M.S at the University of Oklahoma studying novel FTIR catalyst characterization techniques. Thereafter, she joined Dr. Babu Joseph and Dr. Venkat Bhethanabotla's group at USF for a PhD degree. Her work at USF has focused on photoactive materials for CO_2 reduction with H_2O to make CH_4.